McGill University

DEPARTMENT OF MECHANICAL ENGINEERING

Master's Thesis in Mechanical Engineering

Conceptual Design of ISRU Rocket Propulsion Systems for Space Exploration

Sebastian K. Hampl

McGill University

DEPARTMENT OF MECHANICAL ENGINEERING

A thesis submitted to McGill University in partial fulfillment of the requirements of the degree of

Master of Science in Mechanical Engineering

Conceptual Design of ISRU Rocket Propulsion Systems for Space Exploration

Author:	Sebastian K. Hampl
Supervisor:	Prof. Jeffrey Bergthorson
External Research Advisor:	Prof. Evgeny Shafirovich, UTEP
Submission Date:	August 15th, 2024

I confirm that this master's thesis in mechanical engineering is my own work and I have documented all sources and material used.

Montreal, QC, August 15th, 2024 Sebastian K. Hampl

Acknowledgments

I would like to extend my gratitude to all those who have contributed to this thesis, supported me throughout my academic journey in Canada, and who helped me settle in Québec so easily. The research spanning the past two (and a half) years has been akin to an emotional roller coaster, with more twists and turns than I would have hoped.

First and foremost, I express my profound gratitude to my supervisor, Jeff Bergthorson, for his patience and mentorship. His guidance taught me the invaluable skill of critical thinking and self-reliance, which hopefully allowed me to move one step closer to becoming an independent researcher.

Furthermore, I would like to thank Evgeny Shafirovich for supporting my research at the University of Texas at El Paso, where I spent the most fun two months of my whole degree. Enduring countless rounds of paper submission reviews, his support has been crucial in laying the groundwork for this thesis.

I would also like to thank Sam Goroshin and Jan Palečka for providing me with their input and ideas on lunar propulsion technologies. Their continual suggestions have always kept me thinking about some additional challenge that our work had not addressed. Furthermore, I would like to thank Mathieu Francoeur for providing me with the opportunity to teach Thermodynamics and who made my life as his TA very easy.

Additionally, I would like to thank everyone within the AFL lab, who was part of my journey at McGill, and the whole team at UTEP for all the fun taco dinners and late-night trips to Juárez. I would like to especially thank Dominic, who hosted me for the two months in El Paso, took me to explore Texas, and has been of great help with finally getting the publication submitted.

Lastly, I would like to thank all of my friends (be it climbing, running, or skiing buddies) and roommates, Tom, Andrew, Callum, and everyone else who comes over almost daily to hang out at “Le 400": you all have made Montreal feel like home quickly. This also includes all my friends from home, who made the trip over the pond and who are always around when I come back to Munich for the New Year’s party. Be it lobster dinners in Maine with

Fabian or trips from Vermont to Colorado with Max, Maxi, and Quentin, they have always made sure I wouldn't miss home much. This also includes Leendert who was the best lab partner anyone could ask for during his 4 month exchange from TU/e to McGill. I would also like to thank Dylan for always having an open ear and good advice on how to handle roadblocks in the research progress. A special mention goes to Ines for proofreading and rewording my attempt at writing a French abstract for this thesis as well as for all the long runs, hiking trips, and jumping into Corbet's couloir.

Most importantly, I would like to thank my grandmother, father, mother, and Julika for their continuous support, suggestions on all major life decisions, and just being there for me whenever I needed someone to talk to.

My graduate studies would not have been the same without the support of the German Academic Scholarship Foundation, which, aside from financial support, provided me with travel opportunities to their annual conference in Boston and a great network of fellow students around Montréal.

Abstract

Production of rocket propellants from lunar resources has the potential to significantly reduce the cost of space exploration and thus contribute significantly to the development of a space economy. Recent research efforts in this area were focused on the extraction of water from icy regolith for conversion into hydrogen and oxygen, a highly efficient rocket bipropellant. However, water is available only in the polar regions of the Moon, its abundance is to be questioned, and its extraction is a challenging and not a mature technology.

The present thesis aims to assess the feasibility of using propellant components that can be obtained directly from lunar regolith, specifically oxygen, metal alloys, and sulfur through a reduction process based on electrolysis. The concept will also be applicable to other extraterrestrial bodies that contain regolith, such as certain asteroids. Thermodynamic performance characteristics of rocket engines using these components were calculated over a wide range of oxidizer-to-fuel mass ratios. It has been shown that the fuel obtained by extraction of oxygen from regolith, i.e., primarily a mixture of metal alloys, exhibits a relatively high specific impulse of up to 250 s, which is comparable to current solid propulsion systems. The use of fuel-lean propellant mixtures significantly decreases the chamber and nozzle temperatures, which facilitates cooling and potentially reduces the deposition of condensed products in the engine; at the same time, the expected decrease in the specific impulse is less pronounced. The use of sulfur in rocket engines is less promising from a thermodynamic point of view, but it enables engine designs without a need for feeding metal alloy powders.

Multiple different engine designs are proposed and compared and the key engineering design challenges are discussed. Among the different designs the metal-oxygen engine will

have the highest performance but will also be the most complex to design. The sulfur-based engine can be configured as a hybrid rocket (fuel: metal alloys mixed with sulfur, oxidizer: liquid oxygen) and appears to be the most promising in terms of simplicity of the design and predicted performance.

The theoretical work is complemented with preliminary ignition and combustion experiments as well as thermochemical analyses of various metal alloy powders. Particular attention was directed towards silicon and aluminum/silicon alloys, assessed to be the most prevalent compounds in regolith-derived fuel. One notable insight emerged during ignition experiments of the powders in oxygen: the distinct combustion mode of aluminum and silicon, which was also predicted by theoretical computations, was observed. The combustion mode is a key factor to determine product particle size, which directly impacts performance losses in a rocket engine.

Abrégé

La production de carburant pour fusée à partir de ressources lunaires peut réduire considérablement le coût de l'exploration spatiale et contribuer ainsi de manière significative au développement de l'économie spatiale. Les efforts de recherche récents dans ce domaine se sont concentrés sur l'extraction de l'eau contenue dans le régolithe. Le processus d'électrolyse est alors utilisé pour convertir l'eau a ses éléments de base, l'hydrogène et l'oxygène. Ces éléments sont les deux constituants les plus communs du propergol. Cependant puisque l'eau n'est disponible que dans les régions polaires de la Lune, son abondance est remise en question. De plus, la méthode d'extraction de l'eau lunaire est peu avancée et nécessiterait donc être développée plus assidument.

La présente thèse évalue la viabilité de l'utilisation de carburants dérivés de régolithe lunaire. Les dérivés principaux constituent en particulier l'oxygène, les alliages métalliques et le soufre. La performance thermodynamique de ces derniers à été calculée dans le contexte de combustion dans les moteurs de fusée. La variable d'entrée est le rapport de masse entre l'oxydant et le combustible et la variable de sortie est l'impulsion spécifique. Ces calculs démontrent que le combustible obtenu par extraction de l'oxygène du régolithe présente une impulsion spécifique jusqu'à un maximum de 250 s. Cette valeur est comparable à la performance de carburants solides utilisés aujourd'hui. En utilisant un mélange de propergol pauvre en carburant, les températures de la chambre et de la tuyère sont considérablement réduites. Ceci facilite le refroidissement du système de combustion ainsi réduisant le dépôt de produits en phase condensée. Cette diminution de température entraine sans doute une diminution de l'impulsion spécifique. Cependant, cette dernière est beaucoup moins prononcée que prévu. D'un point de vue thermodynamique, l'utilisation du soufre dans les moteurs de fusée est

moins prometteuse. En revanche, elle permet d'éviter injection de poudre d'alliage métallique.

Différents concepts de moteurs sont proposés et comparés. De plus, les défis de conceptions de chacun des moteurs est discuté. Il a été découvert que le moteur le plus performant est celui propulsé à base d'un mélange de métaux et d'oxygène. Cependant, il est le plus complexe à concevoir. Un autre moteur étudié est le moteur propulsé à base de soufre. Ce dernier peut être configuré comme fusée hybride avec un carburant d'alliages métalliques mélangés a du soufre et un oxydant d'oxygène liquide. En termes de simplicité et performance moteur, ce concept semble être le plus prometteur.

La théorie est supportée par des tests préliminaires d'allumage et de combustion ainsi que des analyses thermochimiques de divers alliages métallique. Une attention particulière a été accordée au silicium et aux alliages aluminium/silicium, considérés comme les composés les plus répandus dans les combustibles dérivés du régolithe. Les expériences d'allumage de l'oxygène ont permis de mettre en évidence le mode de combustion distinct de l'aluminium et du silicium. Ceci a également été prédit par les calculs théoriques. Le mode de combustion est un facteur clé pour déterminer la taille des particules de produit ayant un impact direct sur les pertes de performance dans un moteur de fusée.

Contents

Acknowledgments **iii**

Abstract **v**

Abrégé **vii**

List of Figures **xii**

List of Tables **xvii**

1 Introduction **1**

1.1 Preface: Space Exploration and the Space Economy 1

1.2 Space Propulsion 3

1.3 In Situ Resource Utilization (ISRU) 5

1.4 The Case against Water-Based ISRU Propellants 6

1.5 Regolith-Derived ISRU Propellants 7

1.6 Scope of the Presented Work 8

2 Literature Review **10**

2.1 Lunar ISRU Concepts 10

2.2 Regolith Reduction and Space Mining 13

2.3 Non-Regolith-Derived ISRU Concepts 15

2.4 Mission Scenarios 17

2.4.1 Returning to Lunar Orbit 17

2.4.2 Hopper Missions 17

2.5 Metal Flame Combustion 18
2.5.1 Laminar Premixed Metal Flames 19
2.5.2 Laminar Diffusion Metal Flames 22

3 Methodology **26**
3.1 Selection of Regolith Compositions for Analysis 26
3.2 Methodology for the Thermodynamic Calculations 28
3.3 Introduction to the Thermodynamic Codes 28
3.3.1 Comparative Studies and Observations 29
3.3.2 Summary of Findings 35

4 Thermodynamic Calculations **36**
4.1 Rocket Engines Using Oxygen as the Oxidizer 36
4.2 Rocket Engines Using Sulfur as the Oxidizer 44

5 Rocket Engine Configurations **51**
5.1 Metal-Oxygen Rocket Engines 51
5.1.1 “Slurry" 51
5.1.2 Binary Propellant 52
5.2 Sulfur–Based Rocket Engines 53
5.2.1 Sulfur–Oxygen Engine Configurations 53
5.2.2 Metal–Sulfur Engine Configuration 55
5.2.3 Metal–Sulfur–Oxygen Engine Configuration 56
5.3 Engineering Design Challenges 57
5.3.1 Powder Feeding 57
5.3.2 Cooling 58
5.3.3 Erosion 60
5.3.4 Condensed Combustion Products 61
5.3.5 Two-Phase Losses 61
5.4 Comparison 65

6 Experimental Studies **68**

6.1 Thermochemical Analysis of Al/Si Alloys (TGA and DSC) 68

6.1.1 TGA Curves 70

6.1.2 DTG Curves 71

6.1.3 DSC Curves 72

6.2 Ignition Experiments 73

6.2.1 Laser Ignition of Metal Powders in Pure Oxygen 73

6.2.2 Imaging of the Samples 78

6.3 Diffusion Flames 81

7 Conclusions **85**

A Appendix **87**

A.1 Additional Figures for the Thermodynamic Calculations 87

A.2 Supplementary Material for the Aluminum Diffusion Flame Experiments . . . 91

A.2.1 Aluminum powder 91

A.2.2 Coflow 92

A.2.3 First experimental campaign 92

A.2.4 Second experimental campaign 93

Glossary **94**

Bibliography **96**

List of Figures

1.1 Predicted value of the space economy between 2030 and 2050. Adapted from [3]. 2

1.2 Comparison of chemical and electrical propulsion in terms of acceleration and specific impulse [12]. 4

1.3 Applications of lunar ISRU envisioned by NASA. Reprinted from [16]. 6

2.1 Different possible configurations for a metal powder and liquid oxidizer rocket engine. Adapted from [33]. 12

2.2 Measured grain size after the electrolytic reduction process for a lunar regolith simulant. Adapted from [39]. 14

2.3 Difference between a premixed and diffusion flame. 19

2.4 Bunsen flames of various metallic suspensions in air compared to a methane-air flame. Reprinted from [66]. 20

2.5 A stabilized silicon Bunsen flame on a laminar burner. 20

2.6 Dependence of burning velocity in aluminum suspensions on fuel concentration at different concentrations of oxygen diluted with argon. Reprinted from [70]. 22

2.7 Map of the flame propagation regimes within fuel-oxygen concentration coordinates. Adapted from [70]. 23

2.8 Flame temperature along the flame axis height (non-dimensionalized by the maximum measured flame temperature). This highest flame temperature is significantly larger than the theoretical value, which the authors call “superadiabatic" flame temperature[1]. Adapted from [74]. 24

2.9 The closed-tip metal diffusion flame (a) is the equivalent case to the overventilated gas diffusion flame. Analogously, the open-tip metal diffusion flame (b) is the equivalent case to the underventilated gas flame. The exact mechanism and condition when the shift happens were not determined. 25

3.1 Different regolith compositions and their locations on the lunar surface. The majority of the regolith is similar to the highlands type with Al_2O_3 and SiO_2 as the main constituents. Reprinted from [23]. 26
3.2 Composition of ten different regolith-derived fuels assuming all of the oxygen is electrolytically removed. 27
3.3 Thermodynamic calculations for the liquid oxide phases for A-11 RDF and oxygen. In (a) liquid solutions are considered while in (b) only pure liquid oxides are considered and liquid solutions are excluded. 33
3.4 Comparison of calculations for elemental A-11 RDF with and without the introduction of liquid solutions in FactSage. CEA and Thermo results are shown as a reference. 33
3.5 Difference in ISP between vacuum and perfect expansion. All calculations performed with CEA for Al + O_2 at 20 atm chamber temperature and for the I_{sp} case an expansion ratio of 1000. No convergence could be achieved for the frozen I_{sp} calculations at higher O/F mass ratios. 34

4.1 Thermodynamic calculations for the most important metals and metalloids found in regolith, and sulfur. The legend is ordered by peak temperature/peak I_{sp}. A dashed line is used to indicate LOX as the oxidizer, and a dot-dashed line is used for the nonmetallic element sulfur. 37
4.2 Thermodynamic calculations for A-11 RDF and A-12 RDF burning with oxygen performed by Thermo. The calculations for aluminum–oxygen are shown as a reference. The RDF is considered as an elemental mixture and alloy. 38
4.3 Products in the combustion chamber for A-11 RDF predicted by FactSage. . . 41
4.4 Fraction of condensed products inside the combustion chamber, at the throat, and the nozzle exit for A-11 RDF. 42

4.5 Thermodynamic calculations for metal–sulfur reactions. Calculations for the I_{sp} of iron–sulfur do not converge for higher O/F mass ratios. The same applies for other metals at low O/F mass ratios. The legend is ordered with descending peak temperature and peak I_{sp}, respectively. 46
4.6 Thermodynamic calculations for different metal–sulfur–oxygen systems. Calculations for the I_{sp} of iron–sulfur-oxygen do not converge for higher O/F ratios. The calculations of aluminum–oxygen and sulfur–oxygen are also plotted in the graph as a reference. 47
4.7 Influence of the sulfur content on specific impulse for varying volume ratios of the Al–S mixture over different O/F mass ratios. 48
4.8 Thermodynamic calculation for an A-11 regolith-derived mixture, sulfur, and oxygen system. The A-11 calculations with oxygen as well as sulfur–oxygen are shown for reference. 49

5.1 Schematic of the RDF/LOX“slurry" rocket design. 51
5.2 Schematic of the RDF/LOX bipropellant rocket design. 52
5.3 Brimstone rocket in a liquid (spray injection) configuration. 54
5.4 “Brimstone rocket" in a hybrid configuration. 54
5.5 RDF and sulfur in a solid configuration. 56
5.6 RDF and sulfur in a hybrid configuration. 56
5.7 A schematic of the fluidized bed and piston system. Reproduced from [114]. . 58
5.8 Temperatures of the flow at different cross sections for the A-11 RDF$-O_2$ thermodynamic calculations. 59
5.9 Proposed cooling solution for an RDF$-$LOX rocket engine. 60
5.10 Modes of particle combustion in the small Biot number regime. The oxidizer is typically oxygen. Modes A and B produce nanometric solid metal-oxide combustion products in a halo around the droplet, while both variants of Mode C produce micron-sized oxides. Adapted and modified from [66]. 62

5.11 Assessment of the combustion mode at stoichiometry based on the criterion that the metal burns in vapor phase when the flame temperature (T_f) is higher than the boiling temperature of the metal oxide (T_b). The black circles correspond to a pressure of 1 atm, while the red circles correspond to a pressure of 20 atm. The temperatures below the oxidation reactions indicate the flame temperature T_f. 63

6.1 TGA data for the five samples in pure oxygen at a heating rate of 10 K/min. . 70
6.2 DTG curves for all five samples at a heating rate of 10 K/min, which are derived from the previous TGA curves. 71
6.3 DSC curves for the five samples at a heating rate of 10 K/min. 72
6.4 Experimental setup inside the combustion chamber. 75
6.5 Silicon powder ($\approx$ 1 g) burning in a 100% oxygen atmosphere. 75
6.6 Combustion process of different samples captured by the high-speed camera. 77
6.7 SEM images comparing the unburnt materials. 79
6.8 SEM and EDS analysis of a sample of the Al66Si34 alloy. Subfigure (a) shows the unburnt sample of the Al66Si34 alloy powder, while Subfigure (b) shows a SEM image after the combustion process. In Subfigure (c), an EDS analysis is performed, and regions where aluminum is detected are shown in green, regions of silicon in blue, and regions of oxygen in red. In Subfigure(d), the completeness of the combustion process is evaluated, with the dashed lines showing the percentages of the elements when complete combustion occurs. . 80
6.9 A schematic of the old metal dust burner that has been used for premixed aluminum flame experiments. Reprinted from [64]. 81
6.10 Diffusion flames established on the old burner for different oxygen concentrations. 82
6.11 Instabilities observed for the 100% oxygen co-flow diffusion flame over its burn duration. 83
6.12 Mechanical drawing of the new burner assembly. 83
6.13 A stabilized aluminum diffusion flame on the new laminar burner encased in a glass tube. 84

A.1 Thermodynamic calculations for an elemental and an equilibrium composition (A-11 RDF) between FactSage and Thermo. 87
A.2 Detailed gaseous products from Figure 4.3. 88
A.3 Detailed condensed products from Figure 4.3 using the FactSage continuum liquid assumption. 88
A.4 Detailed oxygen products from Figure 4.3. 89
A.5 Influence of the sulfur content on chamber temperature for varying volume ratios of the Al–S mixture over different O/F mass ratios. The parameters for the study are the same as for Figure 4.7. 90
A.6 Temperatures of the flow at different cross sections for the A-11 RDF + S + O_2 thermodynamic calculations 90
A.7 Scanning electron microscope SEM image (left) and the volumetric particle size distribution (right) of "Ampal-637" aluminum powder [133]. 91

List of Tables

3.1 Composition of two exemplary regolith samples before oxygen removal. . . . 27
3.2 Composition of two exemplary regolith-derived fuels (RDFs). 28
3.3 Differences in calculated chamber temperatures between the three solvers for all considered propellant configurations. The deviations are consistent within $\pm 1\%$ for I_{sp} (CEA and Thermo only). 31

4.1 Equilibrium alloy composition calculated in near vacuum ($p = 10^{-6}$ atm) for reduced regolith A-11 (A-12 is very similar and therefore not shown). 39
4.2 Enthalpies of formation of the predicted intermetallic compounds from the Thermo and FactSage databases and partly verified with experimental data from [89, 90]. 40
4.3 Mass fractions in a mixture of 70 vol% metal and 30 vol% sulfur. 48

5.1 Phase of the condensed products at different cross sections for the A-11 RDF + O_2 thermodynamic calculation. 61
5.2 Boiling points (T_b) of the individual metals at 20 atm compared to the adiabatic flame temperatures (T_f) of A-11 RDF burning with O_2 at different O/F mass ratios and the same pressure. The boiling points for the metals at 20 atm were obtained with an iterative procedure in the thermodynamic solver. 64
5.3 Comparison matrix for all proposed rocket engine designs. 67

6.1 Theoretical assessment of the combustion modes of the alloys. (A) indicates vapor phase combustion in Mode A, and (B) indicates heterogeneous combustion in Mode B from Figure 5.10. 78

A.1 Operational variables and their ranges 92
A.2 Experimental parameters for the six distinct runs. As these were preliminary experiments, nitrogen and oxygen were approximated to have the same molar mass for simplicity when setting the mass flow rates. 93

1 Introduction

1.1 Preface: Space Exploration and the Space Economy

"I don't think the human race will survive the next thousand years unless we spread into space. There are too many accidents that can befall life on a single planet. But I'm an optimist. We will reach out to the stars." - Stephen Hawking

Stephen Hawking often spoke about the necessity of space exploration for humankind. Even though his work was mainly focused on underlying astrophysical questions regarding the creation of the universe, he started to engage in aerospace engineering in his later years, and began working on sending a spacecraft to a neighboring solar system.

As a first step, the establishment of a lasting lunar outpost is set to play a pivotal role in advancing space exploration [1, 2]. Such a base will serve as a strategic asset to venture further into space, facilitating improved access to Mars and other celestial bodies. Moreover, the lunar surface holds immense scientific value, providing opportunities for scientific research and the deployment of observatories and communication facilities.

A second, and arguably much more paramount, driver of space exploration will be the commercialization of space and the development of a space economy. The latter is predicted to reach a value of $1 trillion USD by 2030 and grow even more rapidly thereafter [3]. Different estimates for the size of the space economy are presented in Figure 1.1, which clearly shows the size of the yet untouched economic potential.

The number of private startup companies engaged in space mining, particularly on the Moon, has been steadily on the rise. A significant portion of the enthusiasm for lunar mining centers around Helium-3 and its potential use as a future energy source for fusion reactors [4, 5]. Economic assessments related to the material value of asteroids suggest an

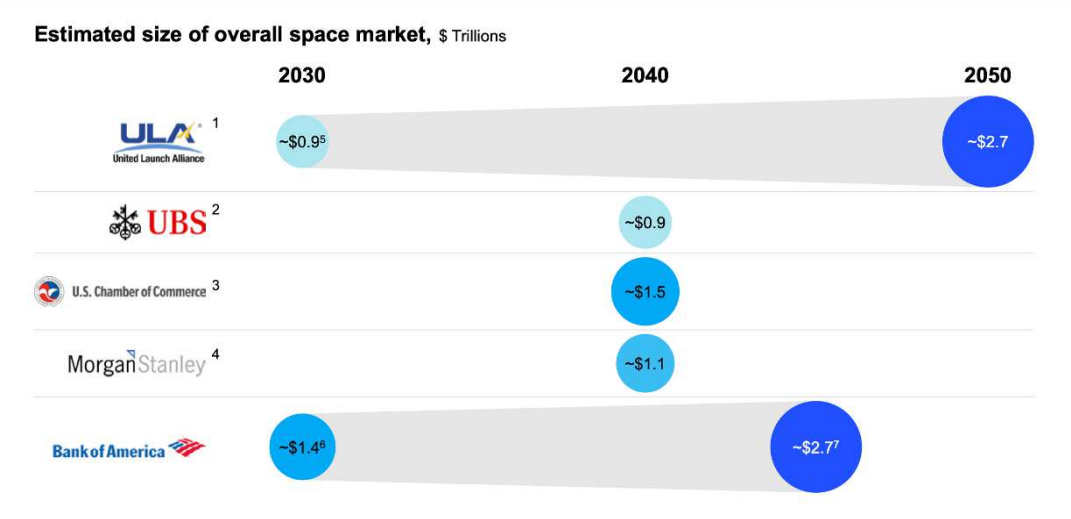

Figure 1.1: Predicted value of the space economy between 2030 and 2050. Adapted from [3].

even greater economic potential for deep-space mining [6]. In a recent study, an asteroid named 33 Polyhymnia was found to exhibit an ultra-high density of $75.3 \pm 9.6\,\mathrm{g/cm^3}$. Such extraordinary densities point to the presence of transuranian elements, with nuclear charges up to $Z = 164$, which do not naturally occur on Earth. These elements could potentially provide almost limitless power through nuclear fission, both in space and on Earth [7]. Based on the value of rare-earth metals commonly present in asteroids, NASA suggests that the target of one of their recent missions, Psyche, is worth \$100,000 quadrillion (10^{15}) dollars. Even though estimates for the value of asteroids differ by multiple orders of magnitude, it is certain that there are trillions of dollars in mining opportunities [8]. Aside from mining, there are multiple applications where the ultra-high vacuum and low-gravity environment of space can be harnessed for in-space manufacturing, which is already being explored in Earth orbit by companies like Airbus [9]. Especially with the recent advances in artificial intelligence and automation, these concepts could be realized as autonomous operations in space with minimal human oversight. To be able to reach the Moon and any objects in deep space, we need advanced space propulsion technologies that rely on the resources available on the bodies that are being explored or mined because bringing material from Earth is very costly and the payload capacity of rockets (for return fuel) is highly limited.

1.2 Space Propulsion

Chemical and electric propulsion are the two main ways of creating momentum in aerospace engineering. The former is used for sending rockets into orbit by generating a high thrust at a low efficiency, while the latter is oftentimes used for in-space satellite propulsion systems where a low thrust is sufficient and efficiency is key[1] [10, 11]. Both propulsion systems are based on Newton's third law and accelerate a spacecraft by ejecting propellant mass, that is carried by the rocket, at a certain exhaust velocity. This principle is described by the rocket equation, which was first derived by Tsiolkovsky in 1903

$$m\frac{dv}{dt} = -c\frac{dm}{dt} \tag{1.1}$$

where v is the velocity of the rocket, c is the exhaust speed of the propellant, t is the time, and m is the time-dependent mass of the rocket. The equation can be integrated into

$$\Delta v = c\ln(\frac{m_0}{m_\mathrm{f}}) \tag{1.2}$$

where m_0 is the initial mass of the rocket with the propellant, m_f the final mass of the rocket (only structural and payload mass), and Δv the total velocity change of the vehicle.

A very important parameter in aerospace engineering is the specific impulse, I_sp, also known as impulse per unit weight of propellant, which describes the efficiency of the propulsion system. It is algebraically defined in integral form as

$$I_\mathrm{sp} = \frac{\int_0^t F dt}{W_\mathrm{p}} = \frac{\int_0^t \dot{m} c dt}{g\int_0^t \dot{m} dt} \tag{1.3}$$

where g is the gravity of Earth, F the thrust, W_p the time-dependent weight of the rocket, and $\dot{m}$ the mass flow of the propellant. If the exhaust velocity c is constant, the equation simplifies to

$$I_\mathrm{sp} = \frac{F}{\dot{m}g} = \frac{c}{g} \tag{1.4}$$

[1] 1 mN thrust on average for electric propulsion systems vs. 34 MN thrust for the first stage of Saturn V (chemical)

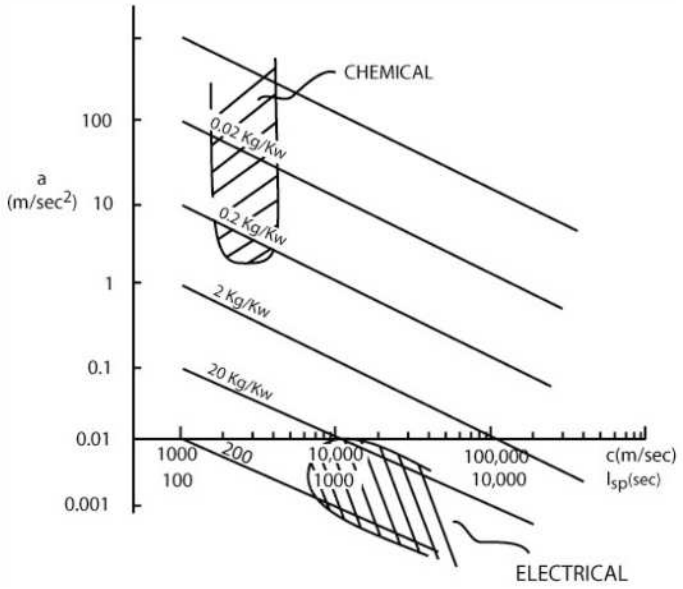

Figure 1.2: Comparison of chemical and electrical propulsion in terms of acceleration and specific impulse [12].

with the unit of the specific impulse typically being in [s] due to the normalization with g. If the concept of specific impulse is incorporated into the rocket equation, the equation can be written as

$$\Delta v = I_{\mathrm{sp}} g \ln\left(\frac{m_0}{m_{\mathrm{f}}}\right) \tag{1.5}$$

As one can see, a high specific impulse is very important to achieve large changes in velocity (Δv). In addition, one also aims to minimize $m_{\mathrm{f}}/m_{_0}$, hence, the majority of the mass will be propellant to achieve high Δv making it the limiting resource. There is a minimum Δv that an object needs to escape the gravitational pull of Earth and reach, e.g., the Moon, but Δv is also used to specify the required performance for orbital maneuvers, such as orbital raising and inclination change.

Despite the numerous advances made in innovative propulsion technologies, particularly in the realm of highly efficient electric propulsion, they cannot replace chemical propellants. Electric propulsion cannot generate the necessary thrust to overcome a gravitational well, as

illustrated in Figure 1.2, which compares the achieved acceleration a [m/s^2] and the specific impulse I_{sp} [s]. There are no current electric propulsion technologies that reach accelerations $> 9.81\ /s^2$ which would be at the minimum required to lift-off from Earth.

The maximum thrust for the highest power electric propulsion system tested, the X3 Hall thruster, is limited to ≈ 5 N [13]. Even if enough thrust could be provided by an electric system to counteract gravity, the maneuvers are not impulsive enough, with thrust-to-weight ratios barely exceeding TWR > 1. These emerging propulsion technologies deliver outstanding performance for orbital maneuvers and deep-space missions, yet they do not serve as a substitute for high-thrust chemical launch systems.

One solution could be a nuclear-thermal propulsion system which is currently being developed by DARPA and NASA and scheduled to be tested at the earliest in 2027 [14].

1.3 In Situ Resource Utilization (ISRU)

When attempting to establish commercial or scientific infrastructure in space, the necessity of directly provisioning these projects with lunar, or other extraterrestrial, resources obtained through ISRU processes becomes apparent. The prohibitively expensive cost of shipping materials from Earth [15], exceeding $35,000 USD per kilogram, underscores the urgency of utilizing local material. A crucial, albeit limited, resource is fuel, particularly rocket fuel (see argument in the previous section about having to minimize m_f/m_0); producing it on the Moon in a cost-effective manner could eliminate a significant bottleneck for return missions, voyages to Mars and beyond, and surface transportation within the lunar environment. Given the Moon's rugged terrain and absence of a substantial atmosphere, the adoption of lunar rocket hoppers is considered an efficient mode of transportation.

NASA has been investigating lunar ISRU for a broad spectrum of applications, which are shown in Figure 1.3. The key applications are using local resources to construct a lunar habitat and extracting oxygen locally to support life on the lunar surface. Propulsion (denoted Lander/Ascent) is not highlighted as a main ISRU application: the graphic suggests using some of the extracted oxygen and methane[2] as the rocket fuels after a lot of processing steps.

[2]Methane is extracted from either the atmosphere on Mars or carbon-bearing ice that is suspected to exist on the lunar surface.

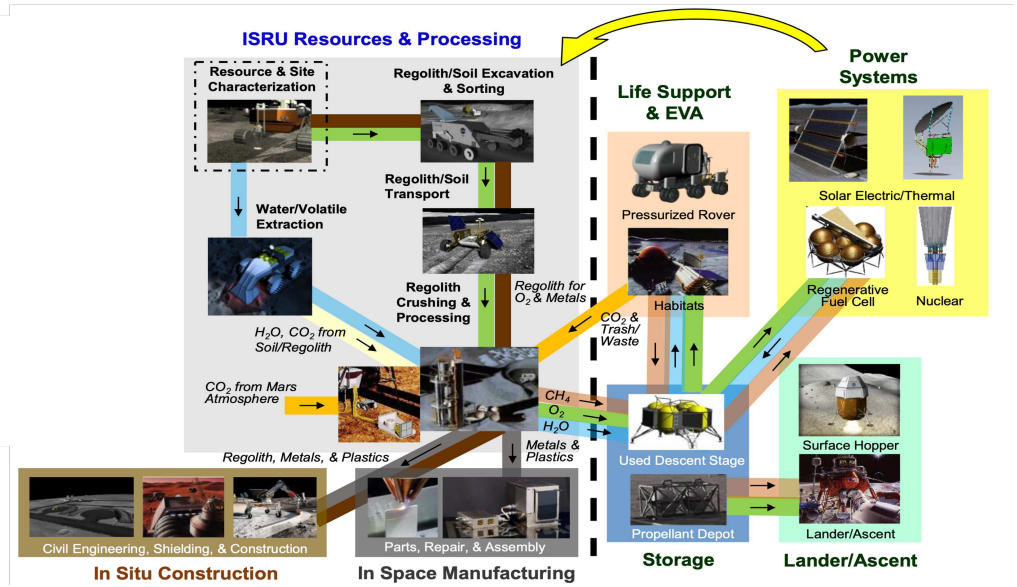

Figure 1.3: Applications of lunar ISRU envisioned by NASA. Reprinted from [16].

Another option that is more commonly proposed for ISRU propellants is the use of water-based propellants. However, there are many unresolved problems associated with them which are discussed in the next section.

1.4 The Case against Water-Based ISRU Propellants

For a long time, the use of hydrogen-oxygen bipropellants, which can be derived from water ice detected on the Moon, was considered the most promising technology. LH_2/LOX engines are a mature technology with high efficiency. However, some factors may limit the feasibility of LH_2/LOX rockets in terms of ISRU technology. The first is the unproven quantity and uneven distribution of water ice concentrated in the polar regions of the lunar surface [17, 18] as well as its total absence on many asteroids depending on their proximity to the sun (where all the ice has evaporated). The recent rover mission "Chandrayaan-3" did not confirm any water deposits on the lunar south pole. Due to the uneven distribution of water, propellant would need to be transported on the Moon from production facilities and bases where water ice is available to bases where hoppers and return rockets might be located. The infrastructure to sustain such an operation is difficult to establish. Alternatively, it has

been suggested that hydrogen could be extracted from metal hydrides on the lunar surface; the process will be very energy intensive, and the quantities of hydrogen are very low, at a maximum of 80 ppm [19]. In addition to that, long-term storage and transport of LH_2 is also challenging because of its much higher volatility in comparison to LOX and extremely low density (0.07 g/cc) as well as its high boil-off rate (up to 11% per hour for the Space Shuttle on Earth and 2% per day on orbit for the PRSD subsystem [20]). Numerical studies for the lunar surface suggest it can be reduced to 0.05% per day but might require large energy inputs (1500 W) for cooling a tank with 9600 kg of LH_2 [21]. Thus, hydrogen storage would require well-insulated, large tanks or, alternatively, high-production-rate facilities at each launch site to supply sufficient amounts of hydrogen just before utilization. When calculating the mass of the tanks (which would also have to be manufactured in-situ), a study suggests that the tank will be more than ten times heavier than the mass of hydrogen it can store [22]. And finally, the sustainability of using valuable water resources, should they finally be confirmed, as a single-use, non-recyclable propellant is contentious.

1.5 Regolith-Derived ISRU Propellants

In the present work, we investigate an alternative solution derived from ISRU methods, which involves the utilization of metal/LOX propellant mixtures. In this concept, both the oxidizer (LOX) and the fuel (powdered metal alloy) are sourced from lunar regolith through a reduction process powered by solar energy. The lunar soil, rich in metal and nonmetal oxides, holds the potential for establishing production facilities on the surface of celestial bodies with solid, rocky compositions. For instance, the Moon's soil primarily consists of oxides, such as silicon, aluminum, titanium, and other trace elements [23]. These metal-based propellants can then be relatively easily stored for extended periods and subsequently employed in rocket engines. Prior investigations, many of which were conducted by NASA, have assessed the performance of such metal/LOX propulsion systems through experimental and theoretical analyses [17, 24, 25].

Another element present on the lunar surface, though not as abundant as silicon and metals, is sulfur, which is also commonly found on many extraterrestrial bodies containing

regolith and can be extracted relatively easily. The potential applications of sulfur in the context of ISRU have been examined [26], primarily with the idea of using it for construction purposes. Studies on metal-sulfur combustion suggest that it can serve as a rocket fuel in various configurations, including solid, hybrid, and potentially bipropellant designs. The configuration of sulfur–oxygen, known as a brimstone rocket, has been well-researched [26]. While its performance may not match that of metal/LOX technology, it remains an attractive alternative and offers a simpler engine configuration from an engineering standpoint.

1.6 Scope of the Presented Work

As outlined in this introduction, the development of propulsion technologies utilizing regolith is essential for the exploration of celestial bodies like the Moon, asteroids, and other bodies within the solar system. Given the breadth of proposed ISRU propulsion technologies, a comprehensive review covering all aspects is unfeasible within the scope of a thesis. Therefore, this study will concentrate on examining chemical propulsion technologies for use on regolith-rich extraterrestrial bodies: metal alloy powder fuel combined with LOX as the oxidizer and sulfur-based propulsion concepts. For the remainder of this thesis, the regolith-derived fuel is referred to as RDF.

A literature review on previously considered ISRU propulsion concepts is presented, as well as a section on lunar regolith reduction, the main technological prerequisite to produce the propellants for the propulsion concepts analyzed in this thesis. Additionally, there will be a brief section discussing ISRU propulsion approaches tailored to specific celestial bodies. Since all proposed propellants contain metals as (part of) the fuel, there will also be a short review of metal combustion research. This is key to understanding the fundamental science behind metal flames, which form the basis for the rocket engine designs.

Subsequently, thermodynamic calculations characterizing the performance of the proposed propellants are presented (Chapter 4). These findings inform the rocket engine designs, which are discussed in the following chapter (Chapter 5). Each of these chapters is separated into two parts for the two different propellant combinations: first, metal alloy and liquid oxygen propulsion systems; and second, propulsion systems using sulfur.

Lastly, preliminary combustion experiments are presented. This work was cut short due to a shutdown of the laboratory at McGill and a malfunction within the thermal analyzers at the collaborating institution in Texas. The results are not fully conclusive, and the experimental campaign could not be completed, but some insights on the combustion mode of aluminum/silicon alloys were gained and a laminar aluminum diffusion flame was successfully stabilized.

2 Literature Review

2.1 Lunar ISRU Concepts

Over the years, there has been sporadic work to harness metal powder as a propellant for lunar propulsion. However, many of these studies have focused on separating the metallic components and only using one of them, oftentimes aluminum, as the propellant. Different engine configurations have been proposed and analyzed on a theoretical level and have been complemented by ground tests evaluating how to feed metallic powder into a rocket engine.

This work has been published in the form of technical reports by NASA investigating the metal/LOX propulsion concepts funded through the RTOP fund. During that time, there were multiple active lunar missions that suggested the existence of surface water and ice [27, 28], and it was concluded to focus on the mining technology to harness these resources for the mature technologies of LH_2/LOX engines. Moreover, erosion of the nozzle and injector by the metalized propellants, as well as the instability of gelled metal propellants, which were the main focus of the research, were identified as additional challenges not present in the liquid bipropellant technology. One last factor was that there was little work on stabilized metal flames, and many people did not consider it a viable technology.

In 1991, Hepp et al. [17] performed thermodynamic calculations and proposed to use metals in combination with oxygen in a rocket engine. They concluded that the propellant combination is very attractive, but substantial gaps exist in how these metals would be extracted from regolith and implemented in an engine design. The following year, Linne and Meyer [29] compared different propulsion technologies and discussed Al/O_2 and Al/H_2O_2 propulsion systems with a similar conclusion. Meyer [24] proposed different engine configurations for Al/O_2 rocket engines, laboratory scale tests of fluidized piston feeding systems, and hot fire

tests of the entire propulsion system. The experiments showed poor performance (around 50% lower than the theoretical value), and multiple problems were identified in the design, such as poor mixing and incomplete combustion. More concepts for metalized propellant with liquid oxidizer engines were proposed in the context of Martian propulsion [30, 31, 32, 33]. The performance figures, especially specific impulse, mainly depend on the propellants, their O/F mass ratio, the chamber pressure, and the expansion ratio for the nozzle. The design of how to supply these propellants, as well as how they are stored, does not influence these theoretical performance figures.

Six different designs for an engine using a powdered metal propellant and liquid oxidizer were proposed and compared in the context of Martian propulsion [33]. These designs are applicable to any such propellant combination and are therefore also relevant for lunar ISRU applications. The six schematic engine designs are shown in Figure 2.1.

Without going into too much detail, the configurations can be described as follows:

(a) A solid fuel grain (using an organic binder that acts as the oxidizer) that burns to produce a fuel-rich exhaust. The exhaust is then burned in a secondary combustion chamber with the liquid CO_2[1] at fuel-lean conditions and expanded through the nozzle.

(b) A hybrid rocket engine concept, which also uses an organic binder (in this case, it is not required to act as an oxidizer) for the fuel grain. Compared to the previous concept, the hybrid can be restarted.

(c),(d) Two variations of a “slurry" design of fuel and oxidizer. Either freezing the CO_2 and metal mixture to create a solid “slurry" or using a liquid CO_2 and metal particle mixture for a liquid “slurry".

(e) A typical liquid bipropellant system where the metal is molten. The energy input required to melt the metal and keep it in a molten state is very high.

(f) A piston feeding system for the powder and direct combustion with the oxidizer. This system mimics the functioning of a bipropellant system, aside from the requirement to inject the metal powder.

[1] Liquid CO_2 as the oxidizer because the concepts were proposed for Martian propulsion.

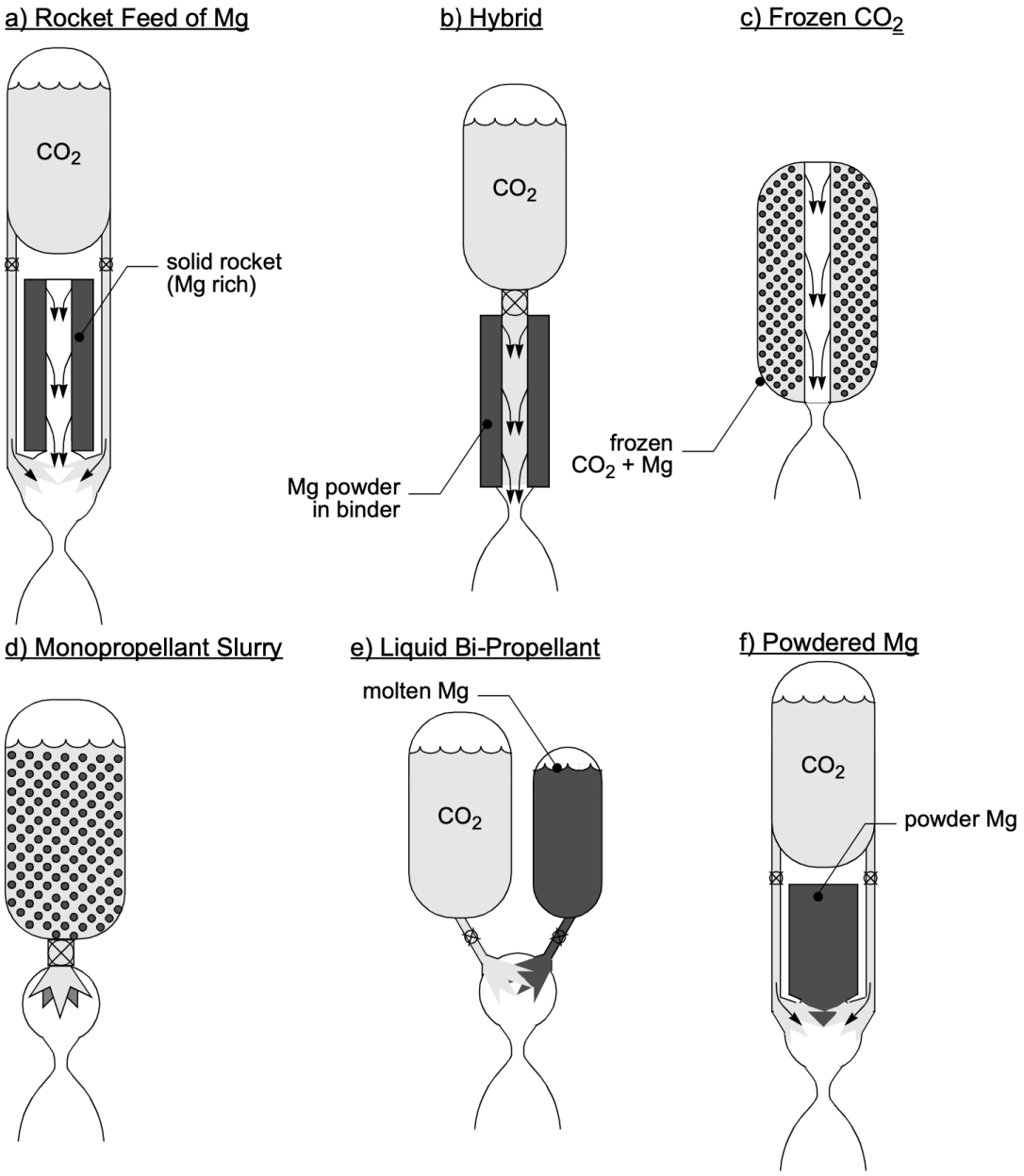

Figure 2.1: Different possible configurations for a metal powder and liquid oxidizer rocket engine. Adapted from [33].

From those options, and based on the results of the study, two options seem the most promising: the monopropellant slurry and the concept using a powder dispersion system and directly combusting the powder with the oxidizer.

In recent years, research has been focused on how to feed powders into a combustion chamber for different applications, mainly ramjet engines. The most studied option in the literature is the positive displacement fluidized bed system, which uses a permeable piston. Methods on how to disperse powders will be discussed in more detail in Section 5.3.2.

2.2 Regolith Reduction and Space Mining

Since the propellants are regolith-derived, the regolith needs to be processed to separate both fuel and oxidizer for the rocket engine. In a recent study, the Technology Readiness Levels (TRLs) were estimated [34]: this nine-level scale goes from 1 (basic principles observed and reported) to 9 (system is flight proven). Water mining and oxygen extraction from regolith are reported at TRL 4/5 (required for a conventional bipropellant system), while the molten electrolysis process to obtain the metal components is estimated at TRL 3/4. Therefore, as of now, there is no significant technological advantage in terms of space mining that would favor focusing on a bipropellant LH_2/LOX system.

The lunar regolith is a blend of minerals that primarily consist of different metal oxides. They all need to be reduced at the same time to obtain metal alloys and oxygen. There have been many studies over the years with the primary goal of obtaining oxygen for a potential lunar habitat. First, they considered reducing the ilmenite ($FeTiO_3$) found within the lunar regolith [35]. Two options were considered for ilmenite reduction: either performing the reduction with hydrogen or alternatively with methane, which requires subsequent methane reforming and then electrolysis to obtain the oxygen. Methane is not available *in situ* and the yield during experimental studies was low at 1 – 3%. Second, a carbothermal reduction of molten regolith was considered [36]. The idea was to use a reduction process with a carbon anode, then, as previously, use methane reforming and then electrolysis. The yield of this process has been shown to be 20 – 30%. Third, molten fluoride electrolysis was considered [37]. The yield of this process was never quantified, and there are problems with the solubility of the oxides in the electrolyte. None of these early studies showed a promising solution for regolith reduction.

In recent years, two processes have been more extensively studied that solve many problems

associated with the previous options: direct molten regolith electrolysis [38, 23] and an FFC-Cambridge process [39] using $CaCl_2$ as the electrolyte. Both seem promising, with the former requiring high temperatures and thus a high energy input while not relying on an electrolyte. The latter seems to work more efficiently as well as being a solid-state process. This means that when feeding powder into the electrolysis reactor, the products will also be a powder, as the regolith does not melt during the process. Both processes have been verified on a laboratory scale and achieved metal-alloy purities of $>95\%$ and a similarly high oxygen extraction rate. The study on the FFC-Cambridge process gives detailed information on the products of the process, specifically the alloy composition, which plays a role when assessing its performance as a rocket fuel (Section 4.1). The main components are:

- An Al/Fe alloy (sometimes with the inclusion of Si)
- A Fe/Si alloy (sometimes with the inclusion of Ti and/or Al)
- A Ca/Si/Al alloy (sometimes with the inclusion of Mg)

Moreover, the particle size was assessed to be the following (Figure 2.2):

Size fraction	Mass (g)	Oxygen (wt.%)
75–150 µm	1.66	5.9
150–300 µm	3.21	3.2
300+ µm	5.94	2.3

Figure 2.2: Measured grain size after the electrolytic reduction process for a lunar regolith simulant. Adapted from [39].

This is relevant since the feeding of metal particles and their combustion properties (Section 2.5) are heavily dependent on the particle size. The purity is lower than the laboratory powders that are typically used in combustion experiments (99.5% pure and higher). However, while this might slightly lower the performance of the system, it is not necessarily a concern for the stability of the combustion process itself and will be sufficient for its use as a propellant in the proposed engine concept.

The only drawback of the FFC-Cambridge process is that the electrolyte is not available *in situ*. The idea is, however, to recycle the electrolyte and thus only have to bring it to the lunar surface once. The process is also viable with different electrolytes other than $CaCl_2$ and there is ongoing research to identify the optimal candidate [40]. Additionally, the influence of low gravity (as is the case on the lunar surface) on the electrolytic process has been investigated, and no major problems have been identified [41].

2.3 Non-Regolith-Derived ISRU Concepts

While a large number of planetary bodies, asteroids, and comets consist of regolith that is similar in composition to the lunar regolith, there are specific planetary bodies of interest where other ISRU propulsion concepts have been discussed. For the sake of completeness, a brief overview of these concepts is provided here.

Mars

Magnesium/CO_2 Propulsion: Mars has a predominantly carbon dioxide atmosphere, which presents an opportunity for utilizing CO_2 as a propellant. One proposed concept involves burning magnesium (which can potentially be extracted from the Martian regolith) with CO_2 in a metal and liquid oxidizer configuration, which is also proposed for lunar ISRU. Experimental studies on single particles have shown that magnesium burns with carbon dioxide [33] and subsequently different rocket engine concepts were proposed [30, 42, 43]. As there is a sufficient atmosphere on Mars, magnesium has also been proposed as a fuel for CO_2-breathing propulsion systems, more specifically ramjet engines [44].

Methane Production: Methane is of interest as it is a commonly used and well tested rocket propellant on Earth. SpaceX almost exclusively relies on CH_4/LOX engines for its Mars mission rockets with the hope of ISRU methane production upon arrival [45]. Methane can be produced through the Sabatier reaction, which utilizes hydrogen (extracted from water ice deposits) and CO_2 (from the Martian atmosphere) to produce methane and water [46]. There are other processes under development using, for instance, zinc as a catalyst to produce methane on Mars [47], and there are small, fluctuating quantities available in the atmosphere

as well, albeit not sufficient for large-scale rocket fuel production [48].

Gas Giants (Jupiter and Saturn)

Hydrogen Extraction: Gas giants like Jupiter and Saturn have atmospheres rich in hydrogen, making them valuable sources of rocket propellant. Extracting hydrogen from these atmospheres could involve various techniques, such as scooping gas directly from the upper atmosphere or utilizing specialized extraction mechanisms [49]. Hydrogen extracted from gas giants could be used as fuel for nuclear thermal rockets or as propellant for other propulsion systems (it is difficult to use this hydrogen in a standard propulsion system due to the absence of an extractable oxidizer).

Titan and Other Moons

Methane Utilization: Moons like Titan, which possess methane lakes and a nitrogen-rich atmosphere, offer opportunities for utilizing methane as a propellant. Methane could be harvested from Titan's surface or synthesized from local resources for use in propulsion systems. Methane-based propulsion systems could enable missions within the Saturnian system and beyond. Propellant options for multiple moons in the Saturnian system are discussed in-depth in [50].

Water Extraction: Europa, one of Jupiter's moons, is believed to have a subsurface ocean beneath its icy crust, containing vast reserves of water. Asteroids and comets also contain water ice among their constituents. Extracting water from these sources could provide a valuable resource for producing propellant through electrolysis, generating hydrogen and oxygen. Water-derived propellants could power spacecraft exploring the Jovian system or be used for deep-space missions [51].

Electric Propulsion

Alternative Propellant Sources: Electric propulsion systems, such as ion thrusters or Hall-effect thrusters, typically use xenon as their propellant due to its high ionization efficiency. However, xenon is relatively rare and expensive. Exploring alternative propellant sources,

such as indium, which may be more abundant on certain celestial bodies, could help mitigate the dependence on xenon [52]. Other plans focus on using helium, hydrogen, and other gases that could be extracted from gas giants, even on the outer bounds of the solar system (Neptune and Uranus), and would enable better access to deep-space [53].

2.4 Mission Scenarios

There are two types of missions on the Moon that typically require rocket engines: return missions back to lunar orbit (LLO), and ultimately to Earth, and ballistic hops to efficiently traverse the lunar surface.

2.4.1 Returning to Lunar Orbit

When returning from the lunar surface to LLO, the Apollo missions used the Ascent Propulsion System (APS) which provided a specific impulse of I_{sp} = 311 s at a chamber pressure of p = 8.3 bar with a payload mass fraction of ζ = 50.31% [54]. The specific impulse of the APS is higher than that of the ISRU options. Assuming that the I_{sp} is 15% higher than the one predicted for a Al/LOX propulsion system, the maximum possible payload fraction of an ascent stage would be ζ = 45.33%, according to the rocket equation, assuming a similar structural mass. As one can see, due to the low gravity on the lunar surface, a lower specific impulse still achieves an acceptable payload fraction.

2.4.2 Hopper Missions

There are problems associated with using rovers on the Moon, such as rugged and unknown terrain as well as low speed when traveling along the surface. These have been the bottlenecks of previous rovers like the Lunar Roving Vehicle, which drove for 30 km on average per mission at a design speed of 13 km/h [55]. NASA successfully tested a ballistic hop of 2.5 m on the Moon using a rocket engine in the Surveyor 6 mission [56].

A study proposed a cold-gas piston system for hoppers on the lunar surface [57]. Others have proposed a system using two to five 66 kN thrust engines for ascent, descent, and hopper missions with an engine burn time of 360 s using a pure Al/LOX system [58, 59]. The

importance of ISRU to hopper missions is discussed in [60], where the authors concluded that, if using propellants transported from Earth, the propellant mass fraction would be prohibitively large after only a few hops for the hopper to be technologically feasible. More recent studies [61] prefer hydrazine monopropellant propulsion systems over the previously proposed options. The main goal for lunar hoppers is to solve the limitations of rovers and their advantages over traditional rover missions are discussed in [61, 62]; an approach that avoids hopping or moving along the surface altogether by close-to-surface levitation systems was proposed in [63].

A study compared the performance of a metal and liquid oxidizer system (magnesium/CO_2 for Mars) with a traditional system [30]. They reached the conclusion that, while the amount of propellant mass transported from Earth increases almost exponentially with the number of hops for a traditional system, the metal/CO_2 system can significantly reduce that propellant mass in the first place, and it only increases linearly with the number of hops. Another study [42] also proposed a multi-sample return mission with hops in between descent and ascent back into orbit for Mars. They proposed a first stage utilizing a metal and liquid oxidizer system and a second traditional bipropellant stage for the return-to-orbit mission.

Therefore, the propulsion system investigated in this thesis can also be an option and be integrated with existing hopper concepts. Its main advantage is, as previously discussed, the ubiquitously available fuel.

2.5 Metal Flame Combustion

While the combustion within a rocket engine is highly turbulent, it is still important to understand the fundamental properties of metal flames. There are two different types of flames: premixed and diffusion flames, which are shown in Figure 2.3.

In a premixed flame, the fuel and the oxidizer are thoroughly mixed when combustion occurs, while in a diffusion flame, the fuel and oxidizer are introduced separately into the combustion zone and mix gradually as they move towards each other. In a rocket engine, we encounter a combination of these types of flames, as the fuel and oxidizer are oftentimes injected separately but can also be injected premixed depending on the specific engine design.

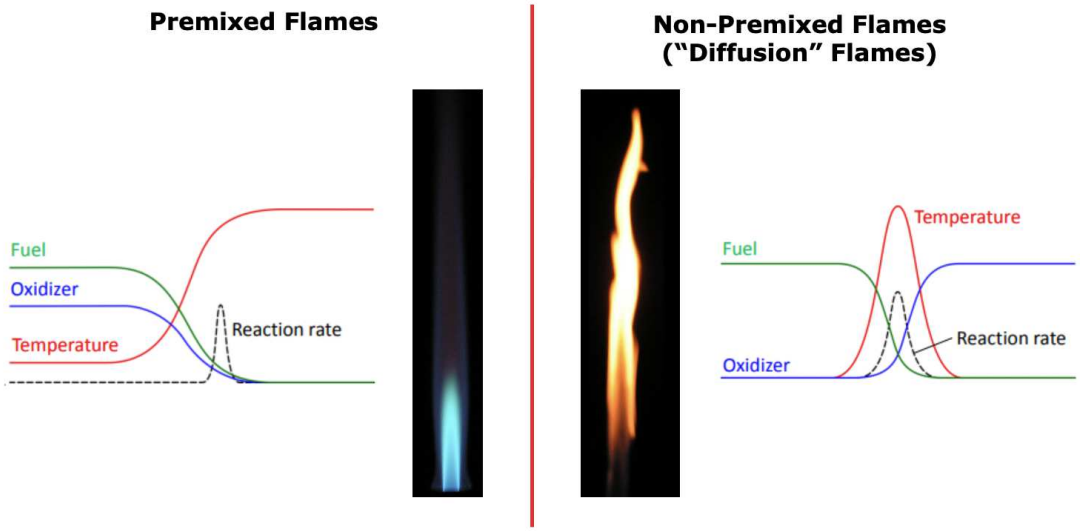

Figure 2.3: Difference between a premixed and diffusion flame.

Research at McGill has focused on laminar premixed flames of mainly aluminum and iron, and the main results are summarized below. As part of this thesis and the broader project, experiments have been planned to investigate diffusion flames. Due to the laboratory closure, these investigations have not been completed, but the preliminary results will be discussed in Section 6.3, and the previous work in the field of metal diffusion flames is also discussed in this section.

2.5.1 Laminar Premixed Metal Flames

Flames of some of the metals found in regolith have been stabilized on Bunsen burners, specifically aluminum, iron, and magnesium. This is possible without any special stabilization device on a custom-built Bunsen burner where the burner lifts particles between 1 and 20 μm in size into a flow of air or other oxidizing gases [64, 65]. An example of such metal flames is shown in Figure 2.4 and compared to a standard methane–air Bunsen flame.

There has also been a recent successful attempt at McGill where a silicon flame was stabilized in the same manner[2] which is shown in Figure 2.5. For the other main metallic

[2]The author would like to thank C. Heng and C. Mani for providing him with the picture of the flame. At the time of writing this thesis, the work has not yet been published.

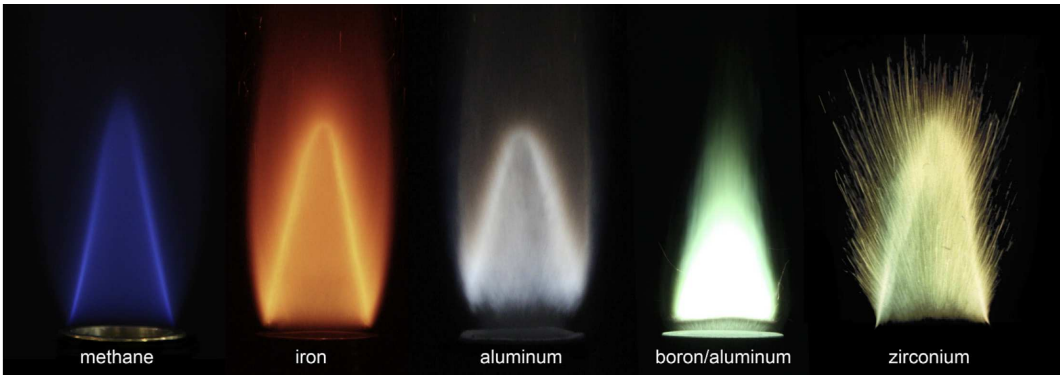

Figure 2.4: Bunsen flames of various metallic suspensions in air compared to a methane-air flame. Reprinted from [66].

components in the regolith, calcium and titanium, studies on stabilized calcium flames and calcium combustion could not be identified. For titanium, studies on single particle combustion have been performed [67].

Figure 2.5: A stabilized silicon Bunsen flame on a laminar burner.

The first laminar metal flames were stabilized by Cassel in the 1960s [68], and they have been investigated at McGill as well as in other laboratories. The breadth of the research and the progress in the field are succinctly summarized in [69]. In general, metal flames show

similar characteristics to flames of gaseous or liquid hydrocarbons.

One of the most relevant flame characteristics for combustion chambers is the laminar burning velocity, as it can inform the maximum mass flow rate (given a fixed combustor size) based on

$$\dot{m} = s_L A \rho \tag{2.1}$$

where s_L is the laminar burning velocity, A the combustor area, and ρ the density of the fuel. From there, the maximum power of the engine can be calculated based on the heat release of the fuel.

The laminar burning velocity is also known simply as flame speed and refers to the rate at which a flame front advances through a combustible mixture during combustion. It represents the speed at which the reaction zone moves relative to the unburnt mixture ahead of it. The laminar burning velocity of a metal flame in air (aluminum in air up to 22 cm/s [70]) is comparable to that of a hydrocarbon (methane in air up to 30 cm/s [71]) albeit lower than that of hydrogen (hydrogen in air up to 250 cm/s [71]). There is one peculiarity, however: the burning velocity plateaus in the fuel-rich regime and is not sensitive to fluctuations. This behavior is shown in Figure 2.6.

This indicates that the flame in the rocket engine will have to be stabilized fuel-rich. Moreover, experimental data for stabilized metal flames is limited to oxygen concentrations of up to 40%. Since the proposed concept operates at 100% oxygen, the flame speed will be higher as it increases with higher oxygen concentrations (also Figure 2.6), and there might be flame instabilities present (Figure 2.7).

All of these experimental studies were performed with a single metal. There has been some work on binary mixtures, which can be found in [72]; however, alloys have not been studied. The work indicates that existing models become less accurate when handling binary mixtures, which makes theoretical estimates of the flame characteristics of complex alloys difficult. Therefore, measurements would have to be conducted to measure properties such as flame speed on the regolith-derived fuel before designing an engine.

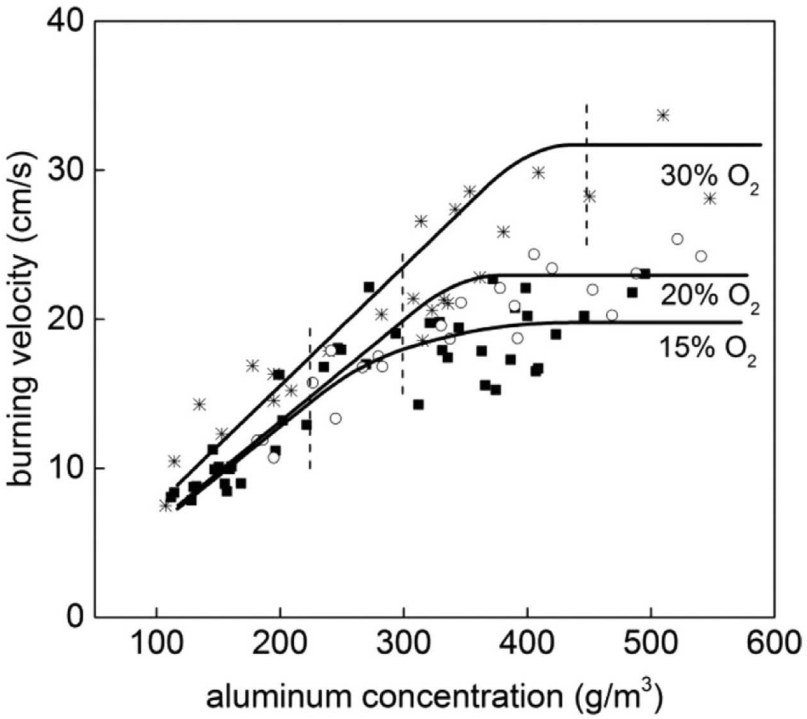

Figure 2.6: Dependence of burning velocity in aluminum suspensions on fuel concentration at different concentrations of oxygen diluted with argon. Reprinted from [70].

2.5.2 Laminar Diffusion Metal Flames

As indicated in Figure 2.3, metal flames can also be stabilized in a diffusion regime. There has been little research in the area, and initially experiments on the behavior of laminar diffusion flames were planned as part of this thesis. These are not directly related to the ISRU concept, but any contribution to the fundamental understanding of metal flames will be useful in further developing metal-based rocket fuels. However, the work could never proceed past the initial stages and obtaining preliminary results (discussed in Section 6.3). The previous work on laminar metal diffusion flames and its shortcomings are described here, which was the motivation for the experimental studies.

A consistent theory for single metal particle combustion has been developed, and combustion modes have been identified [73]. This theory has been applied to premixed metal flames. However, the work on laminar metal diffusion flames attempts to describe them based on

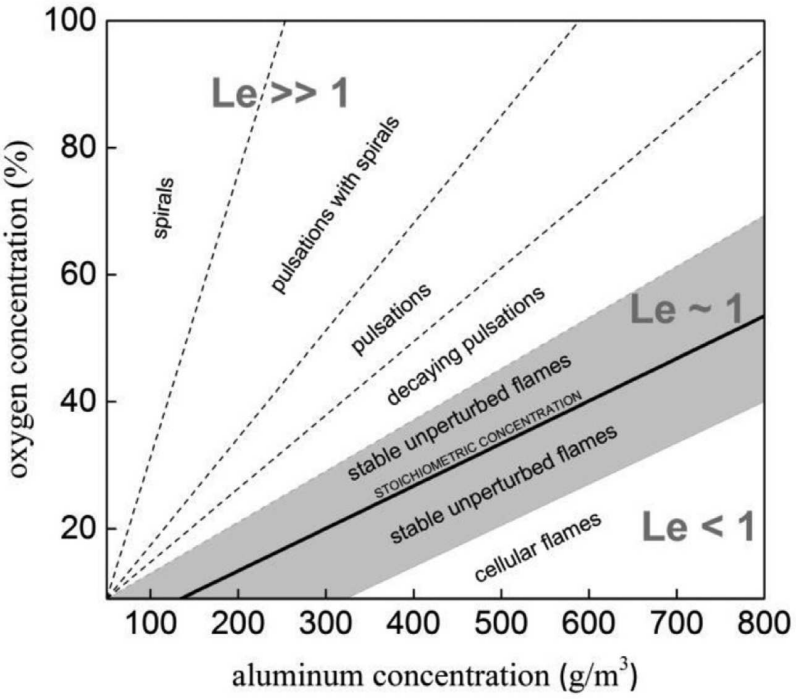

Figure 2.7: Map of the flame propagation regimes within fuel-oxygen concentration coordinates. Adapted from [70].

gas flame Burke-Schumann theory. The problem with that approach is that, in a laminar diffusion dust flame, there is no fuel diffusion since the fuel is not gaseous. Therefore, only the oxidizer diffuses inward into the flame. While in diffusion gas flames the flame boundary can be identified at the point where the oxidizer and fuel concentrations drop to zero due to the combustion reaction, the combustion zone for metal diffusion flames is not as clearly defined. The combustion is expected to happen near the particle surface, and one encounters a microdiffusion flame around the particle located within the broader diffusion flame.

Vovchuk [74] attempted to define a global adiabatic flame temperature for a laminar metal diffusion flame, and came up with the result that this temperature would be increasing along the z-axis, as shown in Figure 2.8.

He inferred this through interferometry and an Abel–transform. While he explained this behavior through heat accumulation along the flame and different radiation and convection heat transfer mechanisms, it is questionable if defining a global adiabatic flame temperature

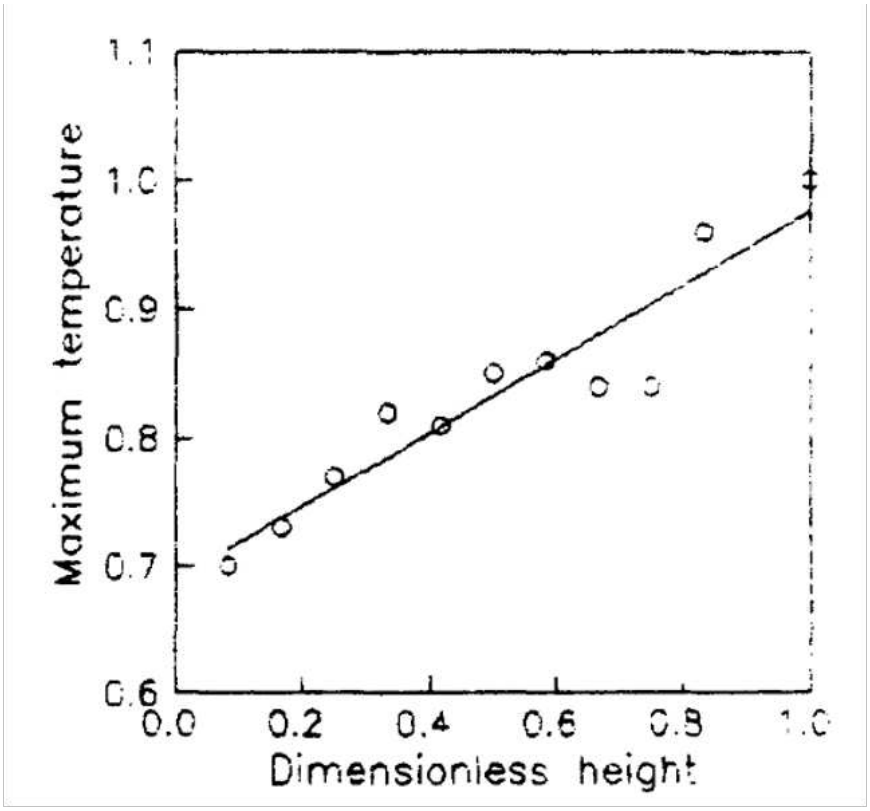

Figure 2.8: Flame temperature along the flame axis height (non-dimensionalized by the maximum measured flame temperature). This highest flame temperature is significantly larger than the theoretical value, which the authors call “superadiabatic" flame temperature[3]. Adapted from [74].

is at all sensible.

The work on laminar diffusion flames also included an attempt to relate flame height and oxygen concentration within the oxidizer flow through an analytical equation [75] as well as stabilizing flames for different metals, which was successfully done for aluminum, iron, and zirconium [76].

Another interesting research subject was understanding how the concept of over- and underventilated diffusion flames transfers to metal diffusion flames. This characteristic

[3]While the concept of “superadiabatic" flames exists for applications such as heat recirculation, its use in the context of a laminar dust diffusion flame might be misplaced. The reasons are provided when examining the shortcomings of their theory on diffusion flames.

of a gas diffusion flame relies on the diffusion of both the oxidizer and the fuel and is thus not observed in the same manner for metal diffusion flames. Instead of an under- or overventilated flame, preliminary experiments suggest that there will be an open and closed tip flame for metals, which is shown in Figure 2.9 [77].

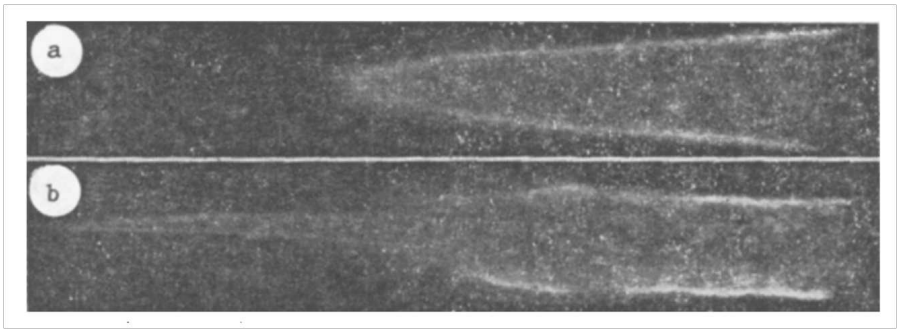

Figure 2.9: The closed-tip metal diffusion flame (a) is the equivalent case to the overventilated gas diffusion flame. Analogously, the open-tip metal diffusion flame (b) is the equivalent case to the underventilated gas flame. The exact mechanism and condition when the shift happens were not determined.

3 Methodology

3.1 Selection of Regolith Compositions for Analysis

Different lunar compositions are considered to assess whether the theoretical performance of RDFs from various types of regolith is sufficient for the concept to be competitive. Figure 3.1 shows a map of regolith resources on the lunar surface and provides three typical regolith compositions [23]. The main elements that will be the constituents of the RDF after reduction (based on ten regolith samples from the Apollo missions [78]) are shown in Figure 3.2.

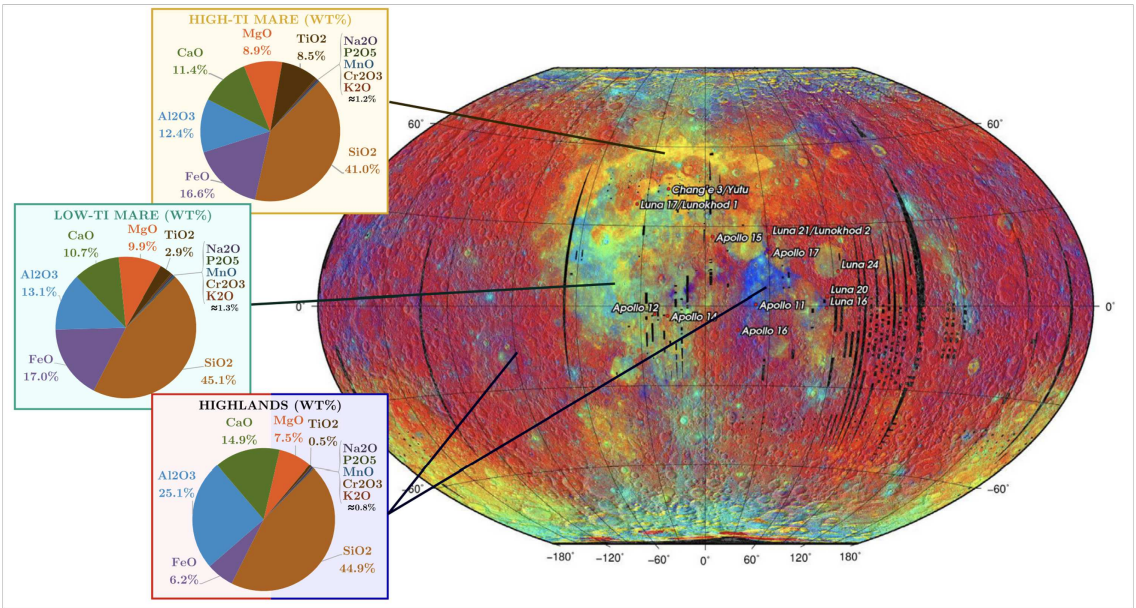

Figure 3.1: Different regolith compositions and their locations on the lunar surface. The majority of the regolith is similar to the highlands type with Al_2O_3 and SiO_2 as the main constituents. Reprinted from [23].

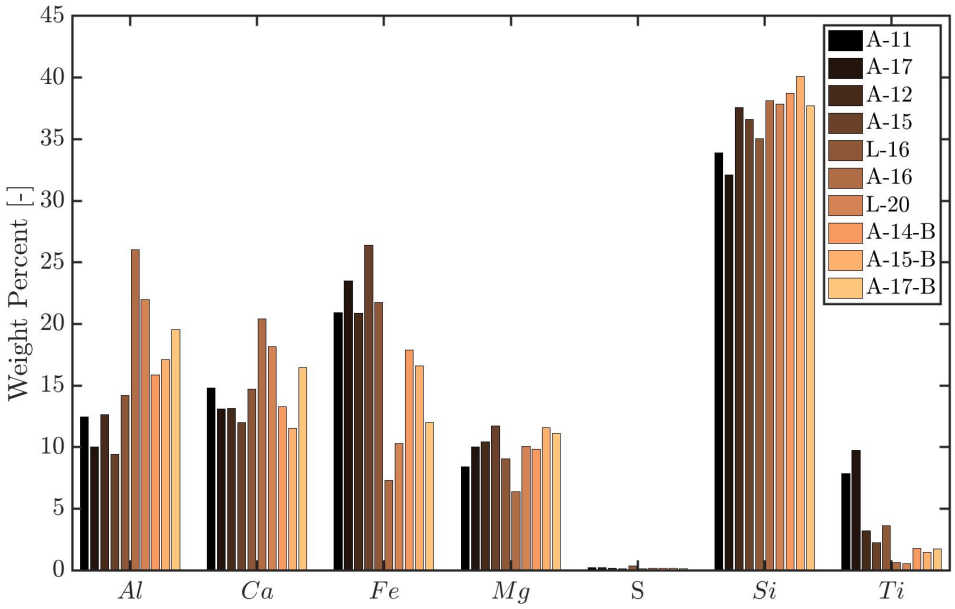

Figure 3.2: Composition of ten different regolith-derived fuels assuming all of the oxygen is electrolytically removed.

Two exemplary compositions (A-11 and A-12, one Low-Ti and one High-Ti regolith) were considered in the thermodynamic calculations. Their compositions before and after reduction are shown in Tables 3.1 and 3.2. While Mare regoliths mainly differ in their titanium content, there is also a Highlands regolith, which contains less iron and more aluminum. There are also differences regarding grain size and thermochemical properties between the different regoliths [79]. For simplicity's sake, we only focus on the two compositions and neglect trace elements (oxide < 5 wt%) with the exception of sulfur.

Table 3.1: Composition of two exemplary regolith samples before oxygen removal.

Region	**Al_2O_3**	**CaO**	**FeO**	**MgO**	**SiO_2**	**TiO**	**Trace**
A-11 (wt%)	13.78	12.12	15.76	8.17	42.17	7.67	0.33
A-12 (wt%)	13.71	10.55	15.41	9.91	46.17	3.07	1.18

Table 3.2: Composition of two exemplary regolith-derived fuels (RDFs).

Region	Al	Ca	Fe	Mg	Si	Ti	S	O_2 ext.
A-11 (wt%)	12.45	14.79	20.92	8.42	33.88	7.86	0.20	41.44
A-12 (wt%)	12.63	13.14	20.87	10.42	37.58	3.21	0.17	42.61

3.2 Methodology for the Thermodynamic Calculations

The thermodynamic calculations determining the theoretical performance of the rocket propellants were performed and verified using three different thermodynamic codes for highest fidelity. The standard approach in previous publications assessing ISRU rocket fuels has been to rely on NASA CEA [17, 80, 81]. However, this code is not optimized for metal fuels or sulfur as an oxidizer. Therefore, Thermo (a Russian thermodynamic code) and FactSage [82] (a commercial thermodynamic software) were also used.

3.3 Introduction to the Thermodynamic Codes

All three thermodynamic codes, namely NASA CEA, Thermo, and FactSage, are based on minimizing Gibbs' free energy. The only difference in results should arise from the databases that include the thermochemical properties of the reactants and products. In our case, a combustion chamber pressure and the reactants, including their initial temperatures and initial state, are specified. In order to infer rocket performance (through the specific impulse), the flow is expanded through a nozzle into a specified pressure environment. This can either be done with continuous adjustment of the equilibrium within the flow or with a "frozen" composition that is found in the combustion chamber.

The NASA CEA code was released in its current form in 1994 [83] and continuously improved since[1]. The thermochemical properties of the substances can be found in the JANAF Thermochemical Tables [84]. This code is well suited for standard liquid and solid rocket fuels, and it includes the capability of calculating rocket performance with continuous equilibrium adjustment. However, the underlying thermodynamic database is insufficient for

[1]The version used for this study is the non-commercial internet version rev4.

metal fuels and sulfur as an oxidizer, which will be shown later.

Thermo code was developed in the former Soviet Union, and the functionality to calculate rocket performance was later added for Mars propulsion applications [30]. The code contains a database of approximately 3,000 compounds [85]. Their thermochemical properties were taken primarily from [86, 87] and partly, similar to CEA, from the JANAF Thermochemical Tables. It also includes complex metallic products in addition to simple oxides, which CEA does not do[2]. One shortfall of Thermo is that it cannot handle reactants with initial temperatures $< 298\,\mathrm{K}$ and therefore LOX.

The third code, FactSage, is mainly used in materials science. Its databases are comprehensive, especially for metals, oxides, and sulfides, and include complex solid and liquid solutions that are not available in the other two codes. Multicomponent phase diagrams for the combustion process can also be easily computed to study phase equilibria at various combustion conditions. It does not include the functionality to calculate rocket performance, though, and one would have to resort to a simple "frozen" equilibrium calculation to infer rocket performance.

In the comparative study, all proposed fuel combinations, including metal–oxygen, metal–sulfur, metal sulfide–oxygen, and metal–sulfur–oxygen, were run on all three codes, and the most important findings are summarized below. To be able to compare the results, the combustion products and flame temperature were considered.

3.3.1 Comparative Studies and Observations

The main goal of the thermodynamic calculations is to assess the viability of the proposed propellants of a rocket engine with the maximum theoretical performance as a proxy. The performance in an actual rocket engine will pose many engineering challenges and will be lower than the theoretical maximum, either due to efficiency losses or as a design choice to lower chamber temperature. For that reason, any discrepancy between the solvers that is $< 15\%$ is disregarded, and only cases where there is a systematic, significant difference in the

[2]Thermo allows for changing the enthalpies manually before the calculation if there are discrepancies with the literature values. Similarly, FactSage allows the user to create their own databases where one can use the preexisting values and make adjustments.

results are investigated. The comparison is also separated into simple systems containing only one metal and complex systems, where a mixture of metals/alloys is considered.

Simple Systems (Single Metals)

The deviations between the three solvers for all propellant combinations that were considered in the thermodynamic calculations are shown below in Table 3.3 (based on the calculated chamber temperature). The difference in percent is calculated by the following equation:

$$\text{Deviation}[\%] = \text{MAX}\left[\frac{T_{c,\text{CEA}} - T_{c,\text{avg}}}{T_{c,\text{avg}}}, \frac{T_{c,\text{Thermo}} - T_{c,\text{avg}}}{T_{c,\text{avg}}}, \frac{T_{c,\text{FactSage}} - T_{c,\text{avg}}}{T_{c,\text{avg}}}\right] \tag{3.1}$$

where

$$T_{c,\text{avg}} = \frac{T_{c,\text{CEA}} + T_{c,\text{Thermo}} + T_{c,\text{FactSage}}}{3} \tag{3.2}$$

The value shown in the table for maximum difference corresponds to the maximum deviation value over all O/F mass ratios. In some cases, a second maximum difference is mentioned in the comments column, showing that two solvers are in good agreement, while the third one shows a large deviation. A color code is employed to highlight the level of deviation, with green indicating a deviation of $< 15\%$, yellow indicating a deviation of 15% - 30%, and red indicating a deviation of $> 30\%$.

The largest deviation is found for iron; however, when excluding CEA, Thermo and FactSage are in good agreement. When looking at the products, CEA predicts $Fe_{0.947}O$ in liquid phase, while the other solvers do not predict it. This is likely the reason for the large deviation.

For metal-sulfur reactions, CEA does not converge in all cases where sulfur is specified as an oxidizer. Thermo and FactSage show deviations of around 20% while predicting similar product compositions. Therefore, the error can only be due to the different thermodynamic properties of the sulfides in their databases.

Table 3.3: Differences in calculated chamber temperatures between the three solvers for all considered propellant configurations. The deviations are consistent within $\pm 1\%$ for I_{sp} (CEA and Thermo only).

Element	Max. Difference	Comments
Metal–Oxygen:		
Al + O_2	1.3%	
Fe + O_2	32.6%	3.8% for Thermo/FactSage
Si + O_2	0.5%	
Mg + O_2	4.6%	CEA/Thermo only
Ca + O_2	7.7%	CEA/Thermo only
Ti + O_2	0.3%	CEA/Thermo only
S + O_2	0.1%	
Metal–Sulfur		
Al + S	20.5%	CEA does not converge
Fe + S	4.6%	CEA does not converge
Si + S	20.8%	CEA does not converge
Mg + S	7.2%	CEA does not converge
Ca + S	3.2%	CEA does not converge
Sulfide–Oxygen		
Al_2S_3 + O_2	13.3%	1.0% for CEA/Thermo
SiS + O_2	7.1%	0.2% for CEA/Thermo
SiS_2 + O_2	18.2%	0.2% for CEA/Thermo
FeS + O_2	5.8%	CEA does not converge
FeS_2 + O_2	9.3%	CEA does not converge
Metal–Sulfur–Oxygen		
Al + S + O_2	1.2%	
Fe + S + O_2	7.8%	2.0% for Thermo/FactSage
Si + S + O_2	1.0%	
Mg + S + O_2	-	Only Thermo; CEA does not converge
Ca + S + O_2	0.5%	
Ti + S + O_2	0.3%	
Complex Systems		
A-11 + O_2	16%	Ranges between 2 - 16%
A-12 + O_2	13.5%	Ranges between 1.5 - 13.5%

When looking at the sulfide-oxygen reaction, the calculations converge again for all three solvers except for iron sulfides. CEA and Thermo are in better agreement than FactSage; this might be due to CEA and Thermo partly using the same sources of thermodynamic data. The metal–sulfur–oxygen systems show good agreement, even for CEA with iron.

When looking at complex systems (in this case, the alloy derived from regolith), there is a large error range depending on the O/F mass ratio. All solvers deviate from each other equally, which is due to the inclusion of different complex products. FactSage predicts the highest temperatures as it includes the heat of mixing, which will be explained in the following subsection.

Complex Systems (Metal Mixtures and Alloys)

When calculating complex systems, there are two major differences between the codes: first, the databases of FactSage and Thermo contain information on ternary systems, while CEA only considers simple oxides. However, when including complex products, we have often observed spikes in temperature and ISP that do not seem to have any scientific background; therefore, it is recommended to exclude these complex oxide products in Thermo calculations. Secondly, FactSage is able to consider liquid metals and oxide solutions (a mixture of several components in a single phase) instead of the combination of several discrete pure liquid oxide and metal phases. The resulting heat of mixing in the liquid phase is not considered in Thermo and CEA. Figure 3.3a shows the evolution of the liquid oxide composition during the combustion of A-11 RDF with oxygen when considering the presence of liquid solutions in FactSage calculations, whereas Figure 3.3b shows the mass fraction of the pure liquid oxide phases when liquid solutions are not included in the thermodynamic calculations. As one can see, pure liquid oxides are predicted to form abruptly at certain O/F mass ratios and the weight percent distribution of the different oxides does not vary continuously, which is unphysical. The actual composition is better approximated when considering liquid solutions.

The combustion temperature is then compared for those two cases and additionally compared with the other two solvers in Figure 3.4. The additional heat of mixing due to the formation of liquid oxide solutions is clearly visible for an O/F ratio of 0.5 to 4 and subsides after.

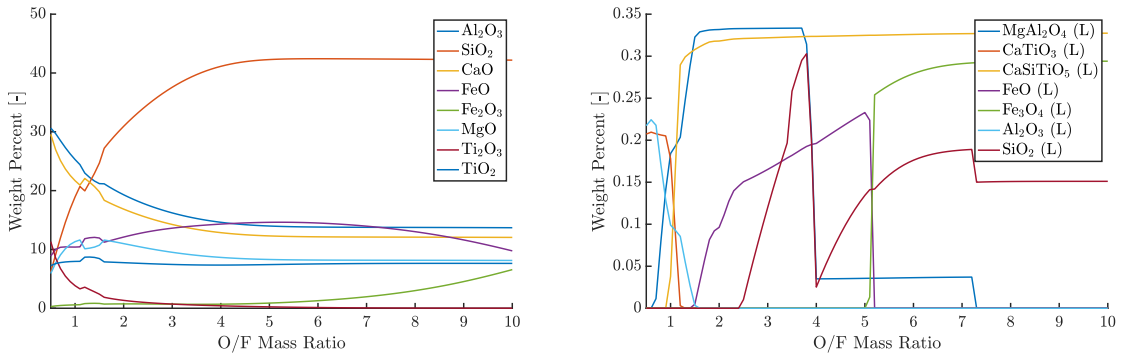

(a) Considering liquid solutions.

(b) Pure liquid oxide composition.

Figure 3.3: Thermodynamic calculations for the liquid oxide phases for A-11 RDF and oxygen. In (a) liquid solutions are considered while in (b) only pure liquid oxides are considered and liquid solutions are excluded.

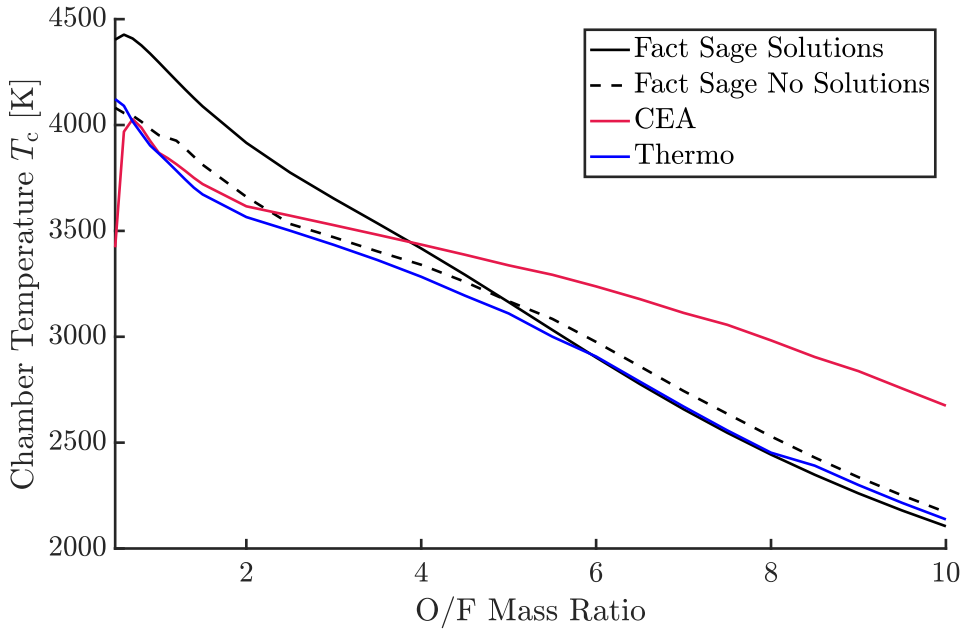

Figure 3.4: Comparison of calculations for elemental A-11 RDF with and without the introduction of liquid solutions in FactSage. CEA and Thermo results are shown as a reference.

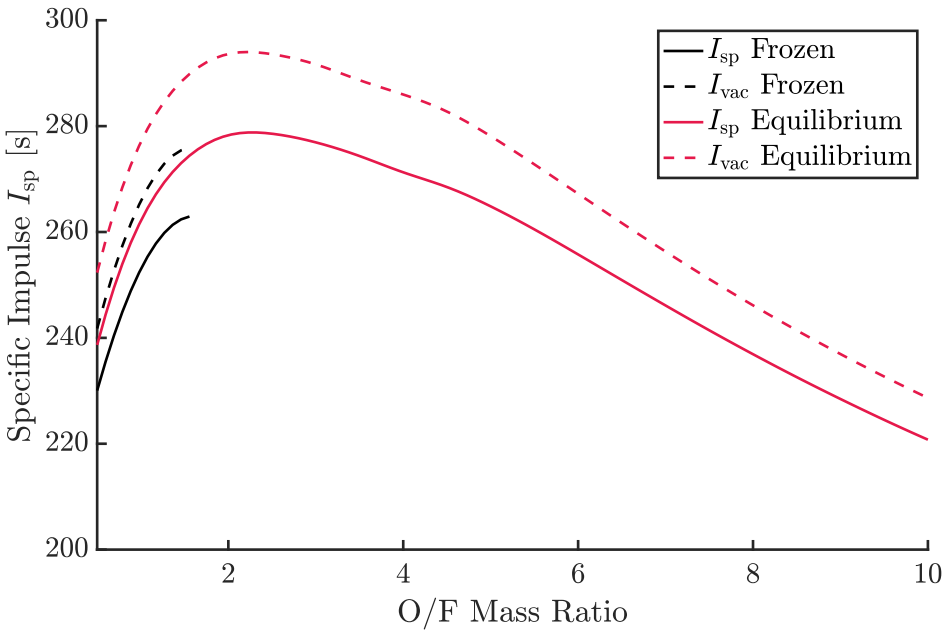

Figure 3.5: Difference in ISP between vacuum and perfect expansion. All calculations performed with CEA for Al + O_2 at 20 atm chamber temperature and for the I_{sp} case an expansion ratio of 1000. No convergence could be achieved for the frozen I_{sp} calculations at higher O/F mass ratios.

There are discrepancies in the predicted metal oxides due to the different databases. It is difficult to pinpoint the exact cause of these errors, however, in complex systems with a plethora of possible combustion products.

Specific Impulse Calculations

Thermo and CEA predicted the same chamber temperature, products, and specific impulse. As mentioned above, FactSage does not include the capability to calculate I_{sp}, therefore, the best possible solution to approximate I_{sp} is a frozen flow calculation, which CEA is also able to perform.

In addition, CEA is the only of the three codes that considers different mechanisms to calculate I_{sp}: frozen and equilibrium. Additionally, both can be calculated for vacuum expansion or for a specified expansion ratio. When calculating frozen I_{sp}, the composition

within the combustion chamber is expanded through the nozzle, while the equilibrium calculation considers shifting chemical equilibrium throughout the nozzle. The frozen calculation, for instance, will not take into account the solidification of some of the liquid oxide phases and other shifting equilibrium effects. For the expansion, one can assume the atmospheric pressure is equal to either the nozzle exit pressure (perfect expansion, I_{sp} in CEA) or zero (I_{vac} in CEA). In Thermo, the expansion into vacuum cannot be calculated. Therefore, calculations were performed for aluminum as a proxy to quantify the difference between the different I_{sp} calculation methods, which are shown in Figure 3.5. As one can see, the equilibrium calculations predict a higher I_{sp} than the frozen calculations, and I_{vac} is higher than the I_{sp} at an expansion ratio of 1000.

3.3.2 Summary of Findings

In conclusion, there is no perfect solver for the given problem. The key limitations and strengths are summarized as follows:

- CEA does not converge for most calculations with Fe-α and when using sulfur as an oxidizer.
- FactSage employs solid and liquid solutions and their associated heat of mixing for complex systems which the other solvers cannot. Moreover, it is able to properly handle ternary and higher order systems. It cannot predict I_{sp}.
- The availability of complex products differs significantly between the databases.
- CEA and Thermo are optimized for rocket applications and estimating performance, while it is only possible to estimate the frozen equilibrium I_{sp} as an approximation with FactSage.

For all thermodynamic calculations that are presented within the paper, the most appropriate solver was chosen based on the comparative study. If the results were within the acceptable error range between the solvers, the lower end of the predicted performance range was chosen.

4 Thermodynamic Calculations

4.1 Rocket Engines Using Oxygen as the Oxidizer

Specific impulse (I_{sp}) at perfect expansion and combustion chamber temperature (T_c) were calculated for oxidizer-to-fuel (O/F) mass ratios ranging from 0.5 to 10 (in steps of 0.1 between 0.5 and 1, and after that in steps of 0.5) for all major metallic regolith components (Al, Si, Fe, Ti, Ca) with oxygen and for sulfur with oxygen. The initial temperature of the reactants was set to 298 K except for the calculation with LOX at 90 K (neither Thermo nor FactSage can run calculations with LOX). The difference between using LOX and gaseous oxygen at 298 K is negligible, as shown for aluminum in Figure 4.1. To smooth the curves, a spline interpolation was utilized. The chamber pressure (P_c) was set to 20 atm, and the ratio of the chamber pressure to the exit pressure (P_e) was set to 1000 (P_c/P_e), which corresponds to $P_e = 0.02$ atm. On the lunar surface, the exhaust expands into a vacuum, and the I_{sp} will be slightly higher due to the pressure term, as can be seen in equation

$$I_{sp} = \frac{v_e + \frac{(P_e - P_a)A_e}{\dot{m}}}{g_0} \tag{4.1}$$

where v_e is the exhaust velocity, P_e the exit pressure, P_a the ambient pressure, A_e the nozzle exhaust area, $\dot{m}$ the propellant mass flow rate, and g_0 the standard acceleration of gravity.

CEA can calculate the specific impulse in vacuum, which is the case for the Moon, however, Thermo does not have that capability. To ensure compatibility, the specific impulse at perfect expansion is calculated and shown in Figure 4.1. The deviation from the specific impulse in vacuum is about 5 – 10 s (see Figure 3.5). The results were computed using different codes, and a rationale regarding the selection of each code for specific calculations was shown in Table 3.3 in Chapter 3.

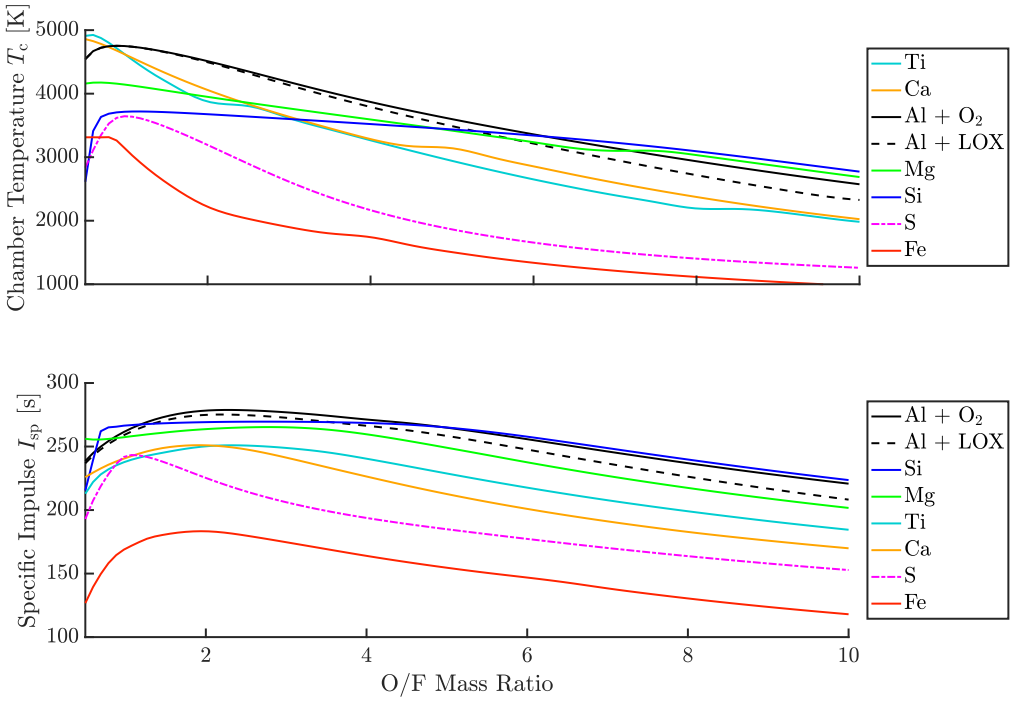

Figure 4.1: Thermodynamic calculations for the most important metals and metalloids found in regolith, and sulfur. The legend is ordered by peak temperature/peak I_{sp}. A dashed line is used to indicate LOX as the oxidizer, and a dot-dashed line is used for the nonmetallic element sulfur.

All propellants but iron have an I_{sp} peak range of 251 s (Ca) to 279 s (Al) over the considered range of O/F mass ratios. Chamber temperatures at peak ISP are predicted to range from 3720 K (Si) to 4900 K (Ti). Iron shows a rather low I_{sp} (max. 183 s) but also a significantly lower chamber temperature with the peak being at slightly over 3300 K. As seen in Figure 4.1, the chamber temperatures decrease significantly for higher O/F ratios, which facilitates cooling. Sulfur burning with oxygen shows both a lower I_{sp} (peak at 243 s) and a lower chamber temperature (peak of approx. 3650 K) than the metals (excluding iron) over the considered O/F mass ratio range.

When a mixture of all these elemental metals and metalloids burns with oxygen, complex products of two or more metals will form, which may change the performance characteristics. We performed the same calculations for two RDFs derived from A-11 and A-12 regolith, as

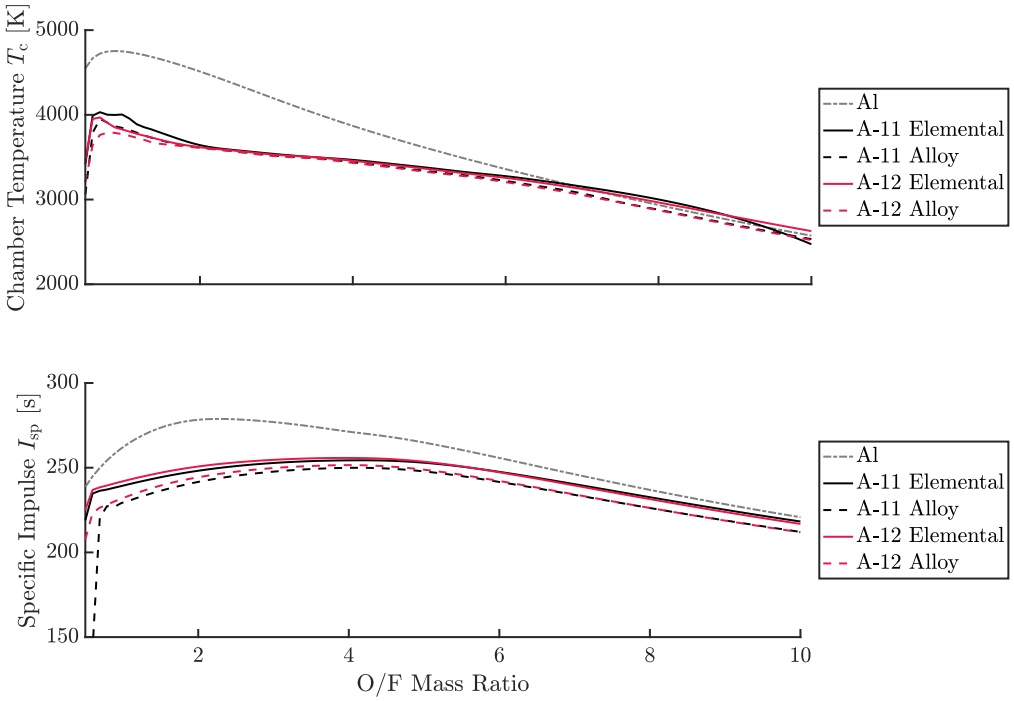

Figure 4.2: Thermodynamic calculations for A-11 RDF and A-12 RDF burning with oxygen performed by Thermo. The calculations for aluminum–oxygen are shown as a reference. The RDF is considered as an elemental mixture and alloy.

shown in Table 3.2. The predicted performance indicates a peak I_{sp} of 256 s with a T_c of approximately 3450 K, and there is only a marginal difference between the two RDFs (see solid lines in the lower graph of Figure 4.2). As expected from the calculations with the single metals, the I_{sp} and chamber temperature for the alloy are lower than those of pure aluminum, the most commonly proposed ISRU fuel.

This calculation is, however, only an approximation of the actual composition of RDF. After the reduction process where the regolith is dissolved in an electrolyte and reduced at 900 °C [39], the product will be an alloy. Separation of its metallic components would require an additional step, which, depending on the process, is either energy intensive or requires chemicals not available *in situ*, or both.

FactSage and Thermo have been used to calculate the equilibrium compositions for the alloys that would be present in the regolith-derived fuel. The results are presented in Table 4.1.

Table 4.1: Equilibrium alloy composition calculated in near vacuum ($p = 10^{-6}$ atm) for reduced regolith A-11 (A-12 is very similar and therefore not shown).

Code	Al_2Ca	CaSi	FeSi	Mg_2Si	Si	Si_2Ti	TiSi	TAU2	FS2L
Thermo (mol%)	18.85	11.30	30.59	14.14	8.37	16.75	-	-	-
FactSage (mol%)	-	37.62	13.38	17.78	-	-	12.20	9.53	9.64

Partly, the same phases are predicted by both codes, while some phases differ; this is mainly due to FactSage predicting ternary solutions (TAU2, FS2L[1]), which Thermo does not do. In general, this calculation is only an approximation of the actual alloy composition after reduction, which will depend on the reduction process, cooling of the liquid phases, and other factors. For the FFC-Cambridge process, the authors noted, for instance, a decrease in silicon concentration after the reduction process due to process related reduction losses for SiO_2 [39]. They found a ternary Ca/Si/Al phase (sometimes also containing magnesium), a binary Al/Fe phase (sometimes with silicon), and a binary Fe/Si phase (sometimes with Ti and/or Al) in the final composition, some of which neither solver predicts (this indicates the relevance of including ternary phases).

To assess if the effect of burning an alloy or an elemental mixture is negligible, one can compare whether the enthalpy of alloying is much smaller than the enthalpy of combustion ($h_{\text{alloying}} << h_{\text{combustion}}$). In a simplified manner, one can compare the standard enthalpies of formation (during the combustion process) for alumina (Al_2O_3), hematite (Fe_2O_3), calcium oxide (CaO), quartz (SiO_2), magnesium oxide (MgO), and rutile (TiO_2), which are -1620.6 kJ/mol, -825.5 kJ/mol, -634.6 kJ/mol, -910.9 kJ/mol, -601.5 kJ/mol, and -938.7 kJ/mol, respectively [84], with the enthalpy of formation for the predicted intermetallic compounds, which are shown in Table 4.2. It is seen that the enthalpies of formation of the intermetallic compounds are approximately 5–10% in magnitude of the enthalpies of formation of the oxides during the combustion process and should not influence the I_{sp} significantly.

[1]TAU2 is a ternary solution $Al_5Fe_2Si_2$-γ ($Al_5Fe_2Si(Al,Si)_2$) (almost identical for both A-11 and A-12 RDF calculations, enthalpies of formation differ by $< 1\%$) from FSstel (solution #168); FS2L is a low-temperature ternary solid solution $(Fe)_1(Si,Al)_2$ from FSstel (solution #79) [88].

Table 4.2: Enthalpies of formation of the predicted intermetallic compounds from the Thermo and FactSage databases and partly verified with experimental data from [89, 90].

Compound	**Al_2Ca**	**CaSi**	**FeSi**	**Mg_2Si**	**Si_2Ti**	**TAU2**	**FS2L**
Enthalpy of Formation Thermo [kJ/mol]	-216.7[2]	−150.9	−80.3	−77.8	−134.3	-	-
Enthalpy of Formation FactSage [kJ/mol]	−90.0	−87.0	−76.4	−65.1	−161.0	−266.1	−96.9

The composition obtained with Thermo is then used as a new composition burning with oxygen, and the results for the chamber temperature showing the difference between alloy and elemental mixture as the initial state of the are presented in the upper graph of Figure 4.2. Slightly lower temperatures are predicted for the alloy than for the elemental mixture. As expected, the slightly lower chamber temperatures also lead to a small decrease in specific impulse, as shown in the lower part of Figure 4.2.

Thermo was used for the calculations since FactSage is unable to calculate the I_{sp}. However, chamber temperatures were verified for the compositions predicted by FactSage, and it predicts a similar decrease in chamber temperature for the alloy compared to Thermo (Figure A.1 in the Appendix).

In conclusion, burning an alloy will lead to an insignificantly lower performance than a mixture or the metallic components. The decrease in performance is not significant enough to warrant the purification or separation of the RDF metal fuels.

One last important aspect is the product composition in the chamber and at the nozzle exit, with a focus on the phases of the products. In general, it is desired to minimize the amount of condensed species as they cause problems with deposition within the engine and lead to two-phase losses of I_{sp}. Detailed calculated products are available in Figures A.2, A.3, and A.4 in the Appendix. For clarity, Figure 4.3 displays only the phase of the products. It is seen that the quantity of condensed species decreases at higher O/F ratios. Gaseous

[2]The FactSage values for the formation enthalpies are in close agreement with the literature. The values in the Thermo database for Al_2Ca and CaSi differ significantly, however, the effect on the combustion temperatures is marginal as seen in Figure A.1 in the Appendix. The Thermo results were further used to calculate I_{sp}.

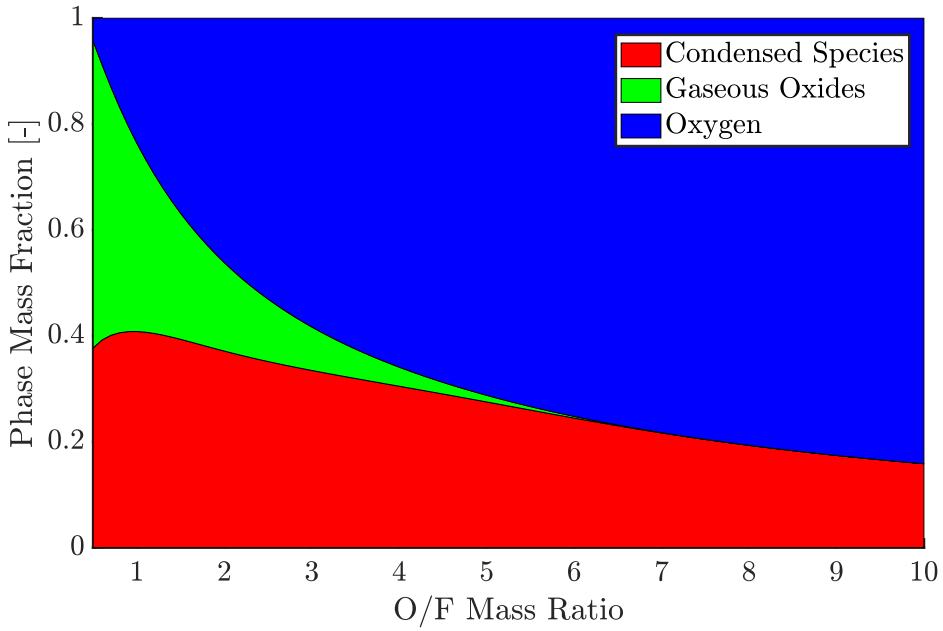

Figure 4.3: Products in the combustion chamber for A-11 RDF predicted by FactSage.

oxides are predominant up to an O/F ratio of 1–2, beyond which oxygen replaces them. Figure 4.4 shows the amount of condensed species at different cross sections of the rocket engine (chamber, throat, nozzle exit). At all locations, the amount of condensed species can be minimized by increasing the O/F ratio.

Thermodynamic calculations offer insight into potential operating conditions for rocket engines and their optimal theoretical performance. These conditions may vary slightly depending on the specific regolith mixtures. The calculations suggest operating at fuel-lean conditions, with an O/F mass ratio typically ranging between 2 and 4, contingent upon the regolith composition. Under these parameters, the specific impulse is projected to fall within the range of 240 s to 250 s with chamber temperatures in the range of 3300 K to 3500 K, which is suitable for regenerative cooling.

This is a first assessment, while in the actual design stage other factors, such as particle size and burning time of these particles, will have to be taken into account. For metal particles and metal dust combustion, these play an important role on the microscopic scale and also influence macroscopic combustion behavior. A critical aspect of this evaluation is determining

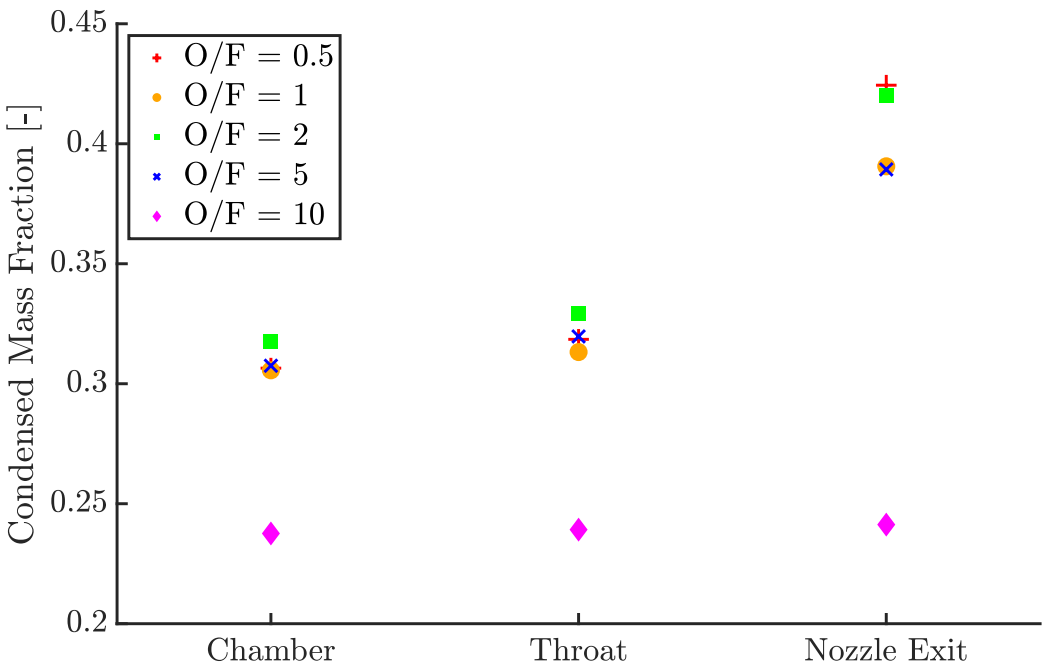

Figure 4.4: Fraction of condensed products inside the combustion chamber, at the throat, and the nozzle exit for A-11 RDF.

the extent to which the chemical energy of burning metal particles is effectively converted into kinetic energy before the particles exit the nozzle. There are two main things that ought to be achieved in the rocket engine design stage: a sufficient burn rate to maximize propulsive power and a sufficient residence time to maximize combustion efficiency. The former is controlled by the diameter of the rocket engine while the latter is controlled by its length.

The duration of particle combustion is significantly influenced by particle size, with larger particles generally taking longer to burn completely than smaller ones. This relationship is a fundamental aspect of combustion science, as the surface area-to-volume ratio of a particle dictates the rate at which reactants can combine with the particle's surface during the combustion process. Smaller particles, with their higher surface area-to-volume ratios, facilitate a more rapid reaction and thus burn more quickly. The concentration of oxygen in the surrounding environment also plays an important role, albeit to a lesser extent. Higher oxygen concentrations can enhance the combustion rate by providing more reactants to

interact with the particle's surface, thereby accelerating the burn time.

This has been experimentally measured for aluminum and iron in [91, 92, 93]. There are multiple ways to define burn time; one is the total time the particle sustains combustion, another one is the 10 – 90% method. This method assesses burn time as 80% of the area under the intensity-time curve. Since the main interest in rocket engines is the heat release, the latter method is more useful for this analysis. Some publications even argue that the heat release is fully completed at the peak of this curve [94] meaning the relevant burn time would be even shorter.

The particle size of RDF that was obtained from the laboratory scale test of the FFC-Cambridge process is $< 75\,\mu$m with more than 50% of the particles being $< 300\,\mu$m. It is very likely that an additional grinding step will be required to reduce the particle size to shorten their burn time.

Burn time measurements are only available for iron and aluminum particles which will be used for the first estimates here. A study measured the burn time to be ≈ 3 ms for 25 μm iron particles in 40% oxygen and 60% xenon [95]. This is a high estimate since RDF burns at a higher temperature than iron and will be burning in 100% oxygen. Moreover, burn rate and burn time are pressure dependent (burn rate: $r = aP^n$, where a is a factor, P the pressure, and n a positive exponent) which will also decrease burn time, since the engine is assumed to operate at 20 atm. For aluminum, the Beckstead correlation is used to estimate burn time (which includes the pressure dependency) [96]:

$$t_\mathrm{b} = \frac{aD^n}{X_\mathrm{eff} p^{0.1} T_0^{0.2}} = 0.13\,\mathrm{ms} \tag{4.2}$$

where a = 0.00735, D = 25 μm, n = 1.5, X_eff = 1 (pure oxygen), p = 20 atm, T_0 = 4767 K (adiabatic flame temperature for aluminum at 20 atm).

Based on these two estimates it is reasonable to assume that the burn time for RDF (after a grinding step) will range between 0.1 - 3 ms.

When designing the engine, one would try to make the length of the combustion chamber equal to:

$$l_c = s_{turbulent} t_b \tag{4.3}$$

where l_c is the combustion chamber length, $s_{turbulent}$ the turbulent flame speed of the RDF fuel, and t_b the previously estimated burn time. It is very difficult to make an educated guess as to what the turbulent flame speed would be, therefore an estimate for the length cannot be provided.

In a second step, one would match the choked mass flow at the throat to the mass flow in the chamber:

$$\dot{m}^* = \dot{m}_c \tag{4.4}$$

$$\rho_c s_{turbulent} A_c = \rho_t u_t A_t \tag{4.5}$$

where ρ_c is the density in the combustion chamber (known from the thermodynamic codes), A_c is the combustion chamber area, ρ_t is the density at the throat (known from thermodynamics), u_t is the velocity at the throat (known), and A_t is the throat area.

Based on this equation, one can design the nozzle as long as A_c/A_t, known as contraction ratio, stays within a feasible range. There is a practical limit for contraction ratios which has to be taken into account. In general it can be expected that the combustion chamber will be much longer than the acceleration/converging nozzle section. The diverging section of the nozzle can then be designed using the method of characteristics.

As previously mentioned, a more concise estimate for RDF is not possible with the limited data. It should be noted, however, that this analysis shows that particle size will play a crucial role when designing the rocket engine as burn times vary drastically and require different combustor lengths for optimal extraction of the particle energy.

4.2 Rocket Engines Using Sulfur as the Oxidizer

Sulfur is not abundant on the lunar surface, but its utilization increases the possible design options for ISRU rocket engines. Early lunar samples indicated the existence of a

low percentage of elemental sulfur in regolith [97] with regional variance in abundance (e.g., high in the Mare soil). The Indian probe Chandrayaan-3 recently confirmed a higher than expected concentration of sulfur in lunar regolith [98]. We also expect sulfur to be present on other celestial bodies composed of regolith, such as asteroids. Hence, the presented ISRU propulsion technology is not confined to the lunar environment. The underlying assumption is that sulfur can be extracted separately from the alloys (using a simple heating process which has been tested on Apollo samples [99]), and it is available in its elemental form to cast/mix rocket propellants.

Just as with the metal-oxygen propellants, we calculated chamber temperature (T_c) and specific impulse (I_{sp}) at perfect expansion for O/F mass ratios ranging from 0.5 to 10 (in steps of 0.1 between 0.5 and 1, and after that in steps of 0.5) for all major metallic regolith components (Al, Si, Fe, Ti, Ca) separately reacting with sulfur (also in a solid state) as an oxidizer. The initial temperature of the reactants was set to 298 K. The chamber pressure (P_c) was set to 20 atm, and the ratio of the chamber pressure to the exit pressure (P_e) was set to 1000 (P_c/P_e), which corresponds to $P_e = 0.02$ atm.

The results, shown in Figure 4.5, predict combustion temperatures ranging from a peak of 4600 K for calcium-sulfur to very moderate temperatures of around 1460 K for iron-sulfur. The predicted peak I_{sp} ranges from 60 to 175 s for the metal-sulfur reaction, much lower than when oxygen is used as the oxidizer.

The utility of metal–sulfur propellant does not lie in its performance, which is significantly lower than that of a metal-oxygen system, but in its simplicity. Metal–sulfur can be cast into a solid propellant grain for a solid rocket motor. Solid rocket motors are simple to design from an engineering perspective as they do not require feeding any propellants.

To maximize performance, while still benefiting from easier propellant handling through casting metal–sulfur, a metal–sulfur–oxygen hybrid system is proposed. This denotes that a solid metal–sulfur propellant reacts with liquid or gaseous oxygen as the oxidizer. This could be in the form of metal sulfide propellant or by using sulfur as "cement" to cast RDF powder into a solid form. There are only minimal quantities of naturally occurring metal sulfides on the lunar surface, and their predicted performance is lower than that of an RDF – S mixture since additional heat is generated through the metal–sulfur reaction before it

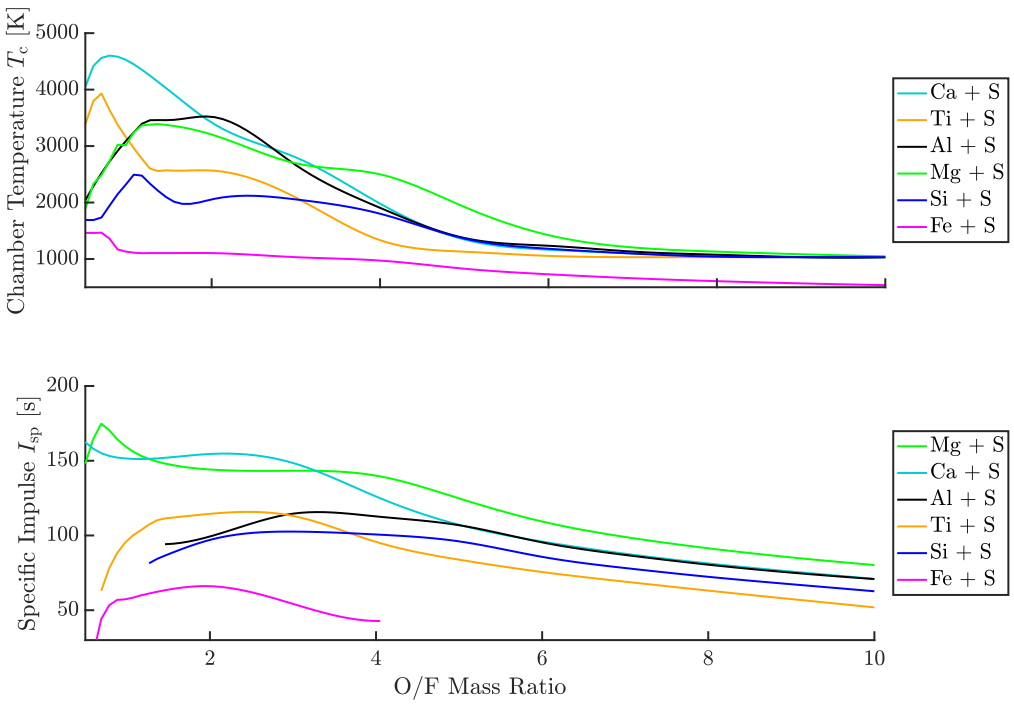

Figure 4.5: Thermodynamic calculations for metal–sulfur reactions. Calculations for the I_{sp} of iron–sulfur do not converge for higher O/F mass ratios. The same applies for other metals at low O/F mass ratios. The legend is ordered with descending peak temperature and peak I_{sp}, respectively.

reacts with the oxygen. Therefore, the thermodynamic calculations were only performed for metal–sulfur–oxygen systems for all metals separately, and the results are shown in Figure 4.6. For completeness, some metal–sulfide mixtures reacting with oxygen were also calculated and showed, as expected, a lower performance than the metal–sulfur–oxygen systems.

The volumetric metal–sulfur mixture ratio corresponds to 70 vol% metal and 30 vol% sulfur, an intermediate value between the maximum (74 vol%) and random (63.5 vol%) packing density of equal spheres (assuming all metal particles are spheres). This assumption has to be modified depending on the particle size of the RDF (for an FFC-Cambridge process mainly $> 300\,\mu$m [39], which would require additional grinding for powder feeding but might be acceptable for casting a solid grain with sulfur) and the sulfur. Moreover, some reduction processes produce porous particles, which would alter the calculations as well.

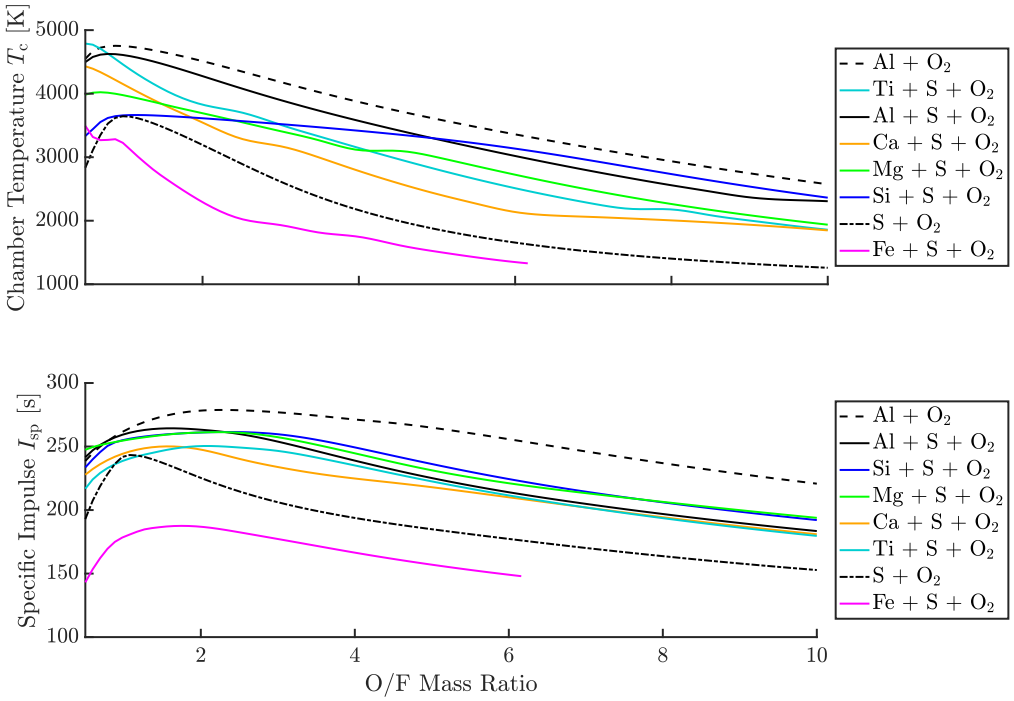

Figure 4.6: Thermodynamic calculations for different metal–sulfur–oxygen systems. Calculations for the I_{sp} of iron–sulfur-oxygen do not converge for higher O/F ratios. The calculations of aluminum–oxygen and sulfur–oxygen are also plotted in the graph as a reference.

The mass fractions based on the volume ratio were calculated by:

$$Y_m = \frac{0.7\rho_m}{0.7\rho_m + 0.3\rho_S} \qquad Y_S = \frac{0.3\rho_S}{0.7\rho_m + 0.3\rho_S} \tag{4.6}$$

where Y_m is the mass fraction of the metal, Y_S is the mass fraction of sulfur, and ρ_m and ρ_S are their respective densities. The mass fractions are shown in Table 4.3. We define the O/F mass ratio for the metal-sulfur-oxygen system as follows; the solid metal and sulfur grain (at the given volume ratio) are considered as the fuel, and we use the molar mass of the grain to calculate the O/F mass ratio with oxygen, the oxidizer.

Figure 4.6 shows that the peak I_{sp} ranges from 180 s to 270 s for the different metals with chamber temperatures up to 4800 K. The performance is about 10% lower for a metal–sulfur–oxygen system compared to a pure metal-oxygen system (aluminum–oxygen is shown as a

Table 4.3: Mass fractions in a mixture of 70 vol% metal and 30 vol% sulfur.

	Al	**Fe**	**Si**	**Mg**	**Ca**	**Ti**
wt% metal	79	84	76	73	59	78
wt% sulfur	21	16	24	27	41	22

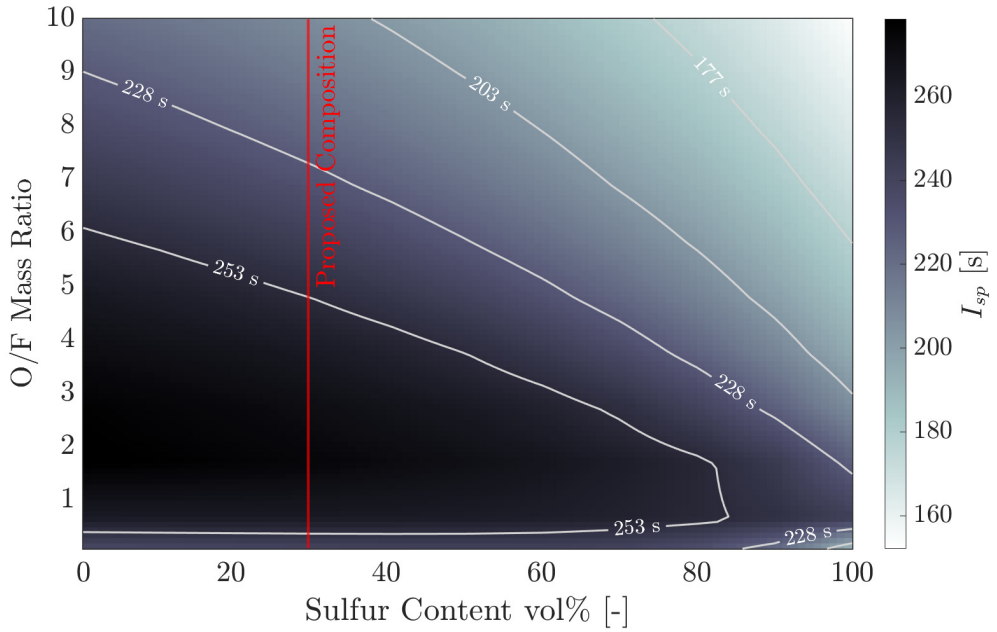

Figure 4.7: Influence of the sulfur content on specific impulse for varying volume ratios of the Al–S mixture over different O/F mass ratios.

reference). However, all of the metal–sulfur–oxygen mixtures except iron show a higher I_{sp} than the brimstone rocket ($S-O_2$).

The influence of the sulfur content in Al – S fuel (oxidizer: oxygen) on I_{sp} was investigated. The results are shown in form of a 2D-map in Figure 4.7 where the sulfur content was varied between 0 vol% (i.e., pure aluminum) to 100 vol% (i.e., pure sulfur) over the O/F mass ratio range of 0.5 – 10. The proposed composition is indicated by the vertical line in the figure, and four iso-I_{sp} lines are shown as contours.

As expected, the addition of sulfur decreases the I_{sp} for any given O/F mass ratio. This

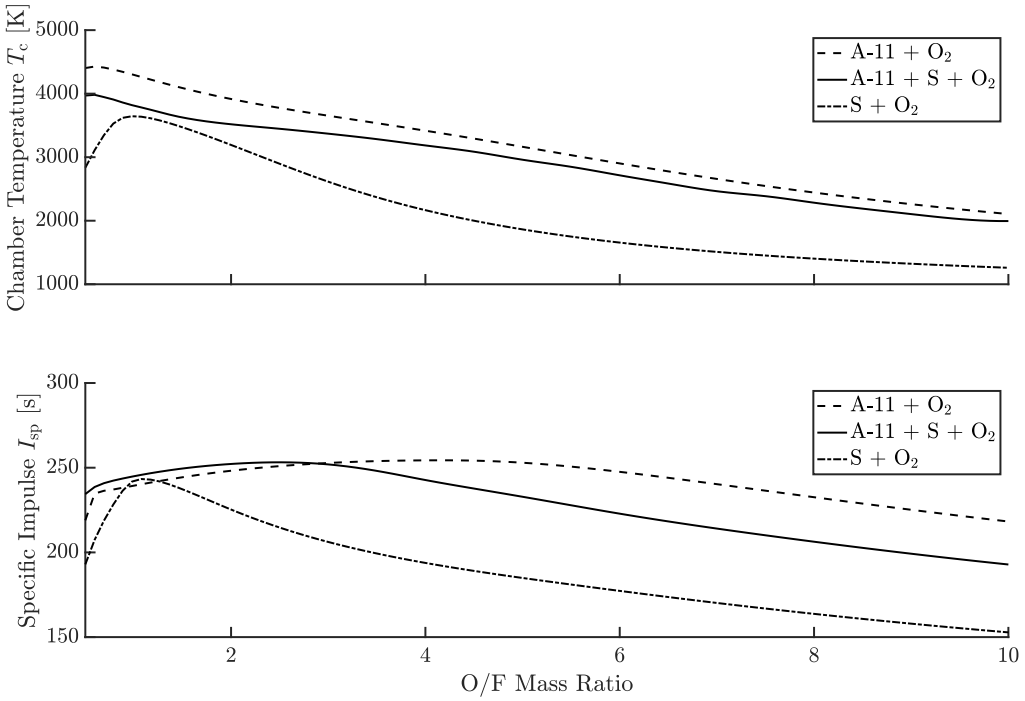

Figure 4.8: Thermodynamic calculation for an A-11 regolith-derived mixture, sulfur, and oxygen system. The A-11 calculations with oxygen as well as sulfur–oxygen are shown for reference.

underscores the idea of using the minimum required amount of sulfur for casting the propellant grain, approximated by the maximum packing density. However, the I_{sp} is relatively constant (> 250 s) for sulfur contents of up to 50 vol% when operating within the proposed O/F mass ratio range of 2 to 4. Similar results can be obtained when doing the same calculations for chamber temperature (the 2D-map is provided in the Appendix in Figure A.5).

Since the products are complex and the convergence of the three solvers is insufficient for some of the metal–sulfur systems, no calculations of an RDF – S system were performed. It is reasonable to expect though that the I_{sp} and chamber temperatures would fall in between the values for the metallic components separately.

For the metal–sulfur–oxygen system, the calculation was performed for both RDFs (A-11 and A-12) as an elemental mixture. Since there is virtually no difference between the results

for A-11 and A-12, only one of them (A-11) is shown in Figure 4.8. It is seen that both I_{sp} and chamber temperature are within the expected range based on the calculations for the pure metals. The temperatures for the propellant mixture with sulfur are lower than when burning with oxygen, while the specific impulse is slightly higher for O/F mass ratios up to 3 and slightly lower for high O/F mass ratios > 3. The RDF–sulfur–oxygen system provides a higher specific impulse than sulfur–oxygen over the whole O/F mass ratio range. It can be expected that an alloy, as previously seen for RDF–oxygen, would also exhibit a slightly lower specific impulse and chamber temperature than the mixture of metals.

5 Rocket Engine Configurations

5.1 Metal-Oxygen Rocket Engines

Based on prior work, which was discussed in Chapter 2, we propose two main configurations for a RDF–LOX rocket engine: a premixed “slurry” design and a binary propellant design using a fluidized piston bed to feed the powder into the combustion chamber.

5.1.1 “Slurry"

A slurry of RDF and LOX, which can be pump-fed and sprayed into the combustion chamber like a monopropellant [64, 80], would be an inherently simple system. A possible configuration for it is presented in Figure 5.1.

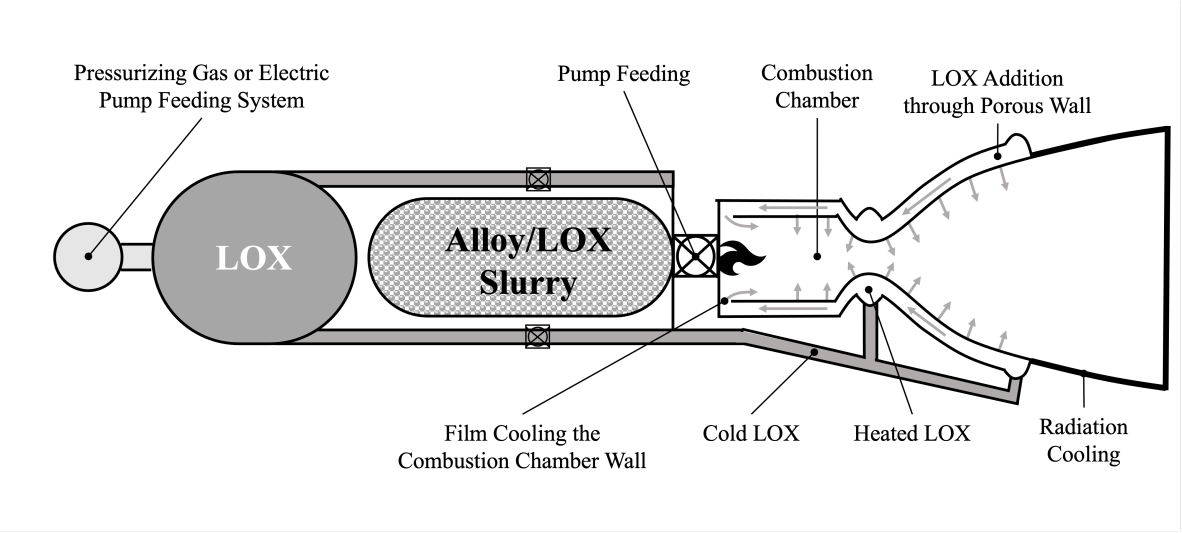

Figure 5.1: Schematic of the RDF/LOX“slurry" rocket design.

Such a system has never been tested and poses challenges for multiple reasons: first,

sedimentation will occur when storing the premixed propellant (especially if it is fuel-lean) because of gravity. One commonly proposed solution is using gelled metalized propellants such as Al/RP-1/O_2 or H_2/Al [50]. However, both rely on either an organic fuel or H_2. Al–LOX mixtures have been used since the 1930s as explosives and are known to be a safety hazard, often resulting in a deflagration-to-detonation (DTD) transition, even with a gelling agent [100, 101]. The proposed gellant was SiO_2, which is available on the lunar surface. Organic polymers are also used as gellants, but they cannot be found *in-situ* [102].

These problems could be mitigated by using a fuel-rich slurry, which minimizes the explosion risk. LOX is added through porous nozzle walls in order to improve combustion performance while avoiding nozzle cooling issues. Even with these improvements, it is questionable whether it can be operated safely. Therefore, we propose an alternate design in the following subsection, which is more promising than the "slurry" design.

5.1.2 Binary Propellant

The RDF – LOX engine can also be configured with a bipropellant design. This system mimics the functioning of a liquid bipropellant engine: the fuel and most of the oxidizer are fed into the combustion chamber separately. A schematic of the concept and its proposed components is shown in Figure 5.2.

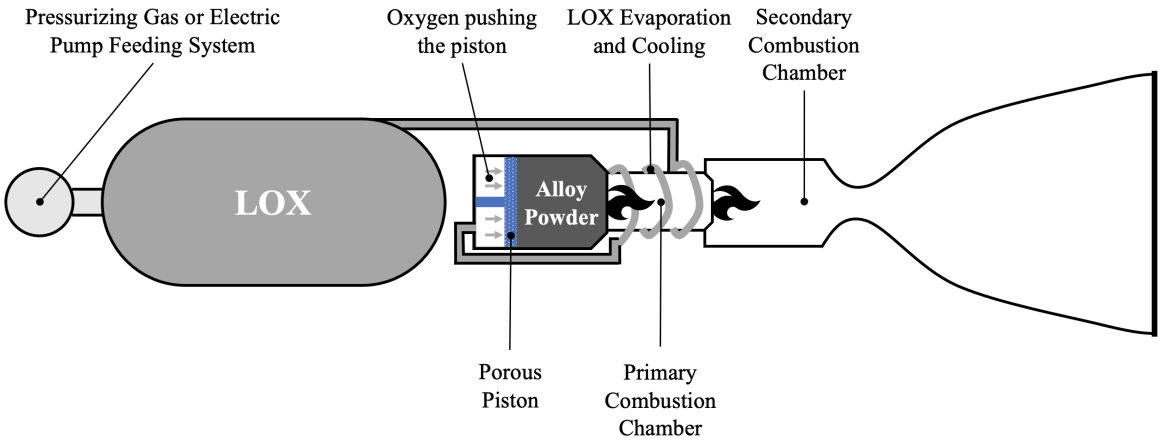

Figure 5.2: Schematic of the RDF/LOX bipropellant rocket design.

On the fuel side, the RDF is stored in loosely packed form inside the fuel tank. The RDF (powder) is then fed into the combustion chamber using a fluidized bed setup. The pressurized gaseous oxygen (after evaporation through cooling of the preburner) is used to push the piston. Since the piston is permeable, part of the oxygen passes through the piston and mixes with the powder; the mixture can then be dispersed, similar to a viscous fluid, and injected into the combustion chamber.

LOX can either be pressure fed or with a turbopump. It might also be possible to drive a turbopump with the oxygen after it has absorbed the heat from the primary combustion chamber, which is commonly done in expander cycles with the fuel. For a low thrust level, a pressure-fed system or an electric pump can be implemented instead of a turbopump; for a high thrust level, a turbopump will be required. To start up the engine and achieve a sufficient temperature for ignition, either a small amount of a hypergolic propellant or a pyrotechnic mixture could be used.

The goal ought to be to operate the engine fuel-lean to lower the combustion temperature. However, to stabilize a flame, a fuel-rich environment is required [70]; therefore, a primary combustion chamber is integrated into the system. This primary chamber is cooled, and the heat from this process is used to evaporate part of the LOX for the dispersion process. The rest of the LOX is injected into the secondary combustion chamber so that the combustion becomes fuel-lean and, additionally, through the porous nozzle for cooling with a boundary layer of oxygen.

5.2 Sulfur–Based Rocket Engines

The inclusion of sulfur as a propellant or additive for RDF enables a broader variety of rocket engine configurations. The different concepts and their specific design challenges will be described in the following subsections.

5.2.1 Sulfur–Oxygen Engine Configurations

The S – LOX (“brimstone") rocket can either be configured as a bipropellant liquid system or as a hybrid. The two designs are shown in Figures 5.3 and 5.4.

The melting point of sulfur is relatively low, 112.8 °C, and the configuration in Figure 5.3 would resemble that of a standard liquid bipropellant engine using spray injection. The sulfur would be preheated to 150 – 160 °C, where its viscosity is lowest, and then introduced as atomized droplets to react with either gaseous or liquid oxygen in the combustion chamber. A more detailed discussion can be found in [26].

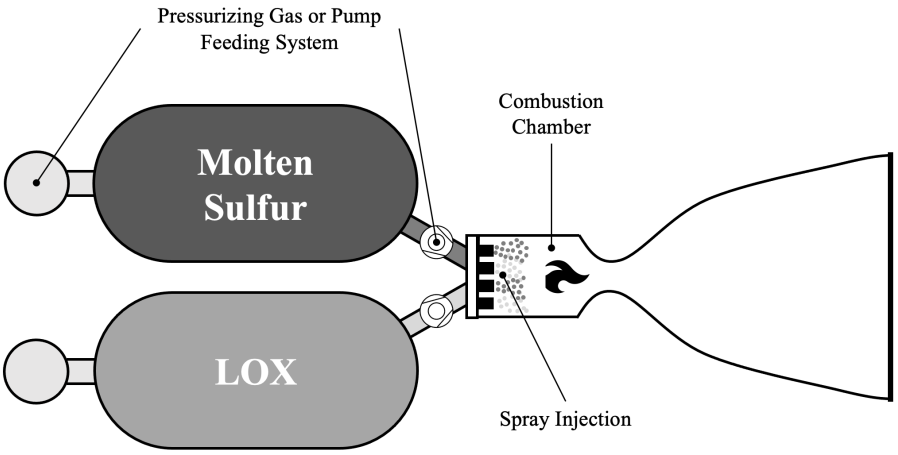

Figure 5.3: Brimstone rocket in a liquid (spray injection) configuration.

Figure 5.4 shows a hybrid engine with a solid sulfur propellant grain and LOX as the oxidizer. Orthorhombic sulfur (its most stable phase) is very brittle and will be difficult to cast into a fuel grain without another component, such as a metal. For a “brimstone" rocket without additives, the bipropellant design is more promising.

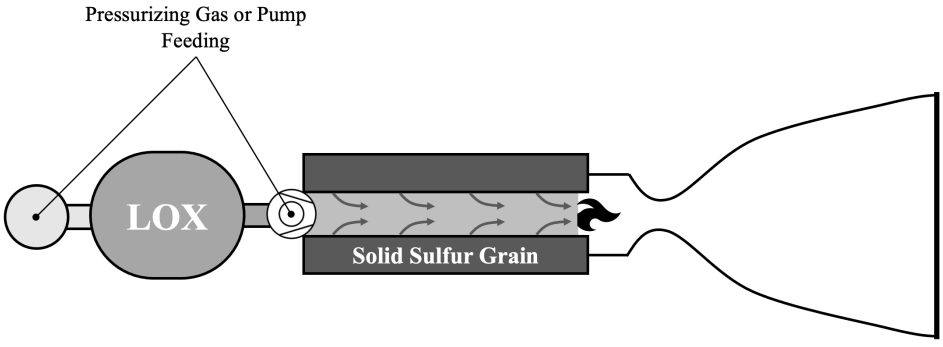

Figure 5.4: “Brimstone rocket" in a hybrid configuration.

5.2.2 Metal–Sulfur Engine Configuration

The enthalpy of formation of metal sulfides is considerably lower than that of corresponding oxides, which results in a relatively low I_{sp} of Me – S propellants as demonstrated by the thermodynamic calculations presented above. However, the non-cryogenic solid metal–sulfur fuels possess one important advantage: they have virtually unlimited storage life. Depots of stored metal-sulfur solid boosters would ensure guaranteed ascend to planetary orbits for mating with nuclear thermal or electric transportation tugs [103] and would permit fast on-planet emergency transportation via suborbital flights. Pressed zinc–sulfur powders have been used as a safe propellant in amateur rocketry since the 1950s. Beside their low I_{sp}, the other undesirable property of Zn – S propellant is its very fast burning rate [104]. The sulfur in the metal–sulfur mixture can be melted by heating the Me – S powder blend above the sulfur melting point (115 °C) [105], which is 200 – 400 °C below the mixture ignition temperature. The resulting slurry can be cast as a propellant grain with a combustion channel of an arbitrary shape. The burning rate of cast metal-sulfur compositions is much lower than that of the pressed metal-sulfur powder grain and is in the 4 – 8 mm/s range [106, 105, 107, 108], approaching the combustion rate of standard composite solid propellant. To increase the combustion rate, the metal-sulfur slurry can also be cast as small droplets in the manner of artillery propellant grains. The calculations indicate that 15 metals are capable of self-sustaining combustion with sulfur. Combustion of the cast Al, Ti, Si, Fe, Mn, – sulfur blends was observed experimentally [106]. The advantage of metal–sulfur boosters, which is schematically shown in Figure 5.5, is their inherent simplicity, allowing practically all-solid booster parts to be manufactured *in-situ*.

For-example, refractory nozzles that require heat resistivity can be net-shape manufactured using Self-Propagating High-Temperature Synthesis (SHS) of Cr – S cermets [108]. To protect the wall of the combustion chamber from deposition of melted sulfide droplets, the propellant grain can be cast with a thin outside layer of pure sulfur, whose gasification (boiling) at about 445 °C will provide outflow, preventing deposition of the sulfide particles.

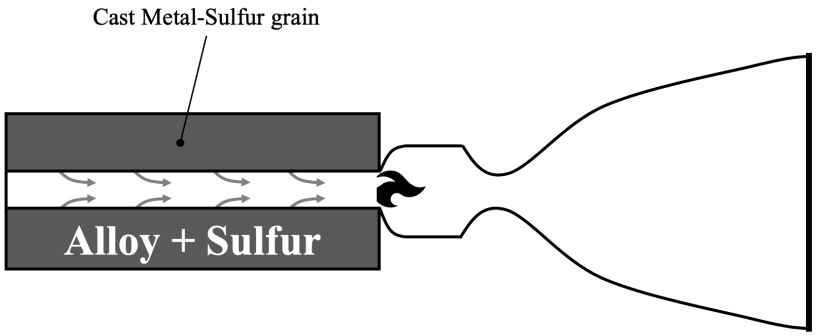

Figure 5.5: RDF and sulfur in a solid configuration.

5.2.3 Metal–Sulfur–Oxygen Engine Configuration

The most promising engine configuration using sulfur is a metal–sulfur–oxygen hybrid rocket engine, whose schematic is shown in Figure 5.6.

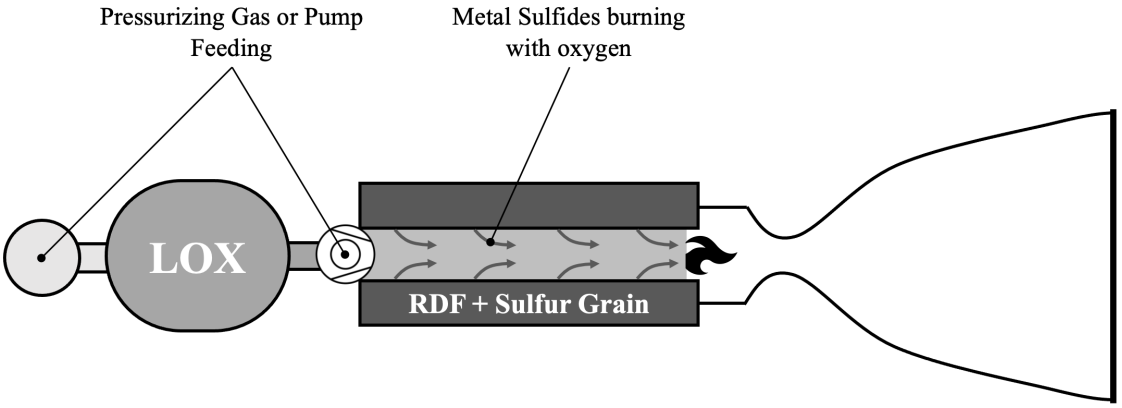

Figure 5.6: RDF and sulfur in a hybrid configuration.

While sulfur decreases the specific impulse of the system compared to pure metals, it enables the much simpler hybrid configuration in contrast to the configuration presented in Section 5.1. Therefore, it is recommended to minimize the sulfur content in the solid fuel grain to achieve maximum specific impulse (as presented in Figure 4.7). The minimum sulfur content is set to fill the gaps between spherical metal particles at maximum packing density, thus allowing for the solidification of the fuel grain.

In practice, hybrid engines have suffered from many problems that prevent them from reaching their predicted performance and stable operation. Two main problems are the formation of a turbulent layer in the combustion zone and an inconsistent regression rate [109]. The proposed propellant will lead to two separate combustion reactions: first, between the alloy and sulfur, which then further reacts with LOX. This could decrease the formation of a turbulent boundary layer and lead to a more consistent propellant burn rate.

5.3 Engineering Design Challenges

5.3.1 Powder Feeding

The most tested option in the literature is the positive displacement fluidized bed system, which uses a permeable piston. In this approach, the fuel is stored in a cylindrical pressure vessel (in powdered form) and backfilled with a carrier gas. When the valve is opened, the carrier gas (an inert or the oxidizer) entrains the fuel as it penetrates through the piston. Then the fuel can flow into the combustion chamber as a dense mixture of carrier gas and metal particles. Such a system has been successfully tested for aluminum and air [25] and for aluminum/magnesium and water [110].This system has also been proposed for magnesium and CO_2 [111] and successfully tested for these reactants [112, 113]. A study was conducted on aluminum-fueled ramjet engines also using a fluidized bed and piston system [114]. Their system does not use an inert dispersion gas but the oxidizer directly. The schematic from their work is shown in Figure 5.7 and has been adapted to fit our proposed binary propellant design (Figure 5.2).

A study [115] also tested both the fluidized piston and a motorized piston, proposed earlier in [116]. The paper concludes that the fluidized system is more suitable than the motorized piston. The dispersion of regolith mixtures has not been studied, and experiments will have to be conducted to identify which modifications to the dispersion system might be required. These will also depend on the particle size (which can be decreased through an additional grinding step) after the reduction process.

Supplying cryogenic LOX is commonly done in rocket engines. However, most of these engines use an engine cycle (such as staged combustion, expander cycle, etc.), and the

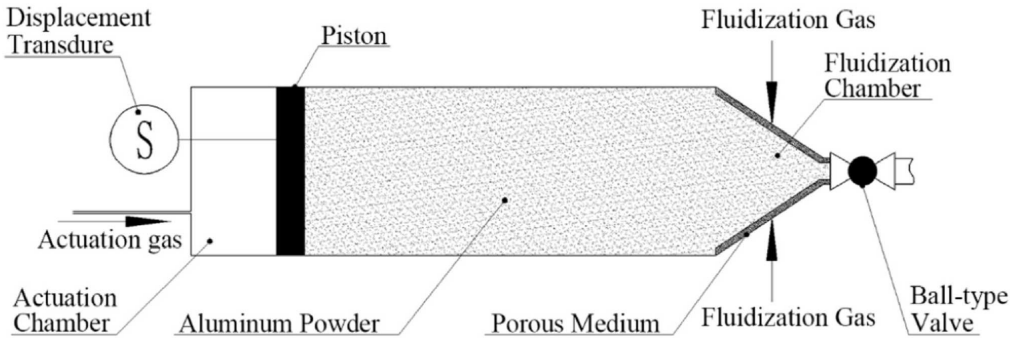

Figure 5.7: A schematic of the fluidized bed and piston system. Reproduced from [114].

pressurization of the oxidizer is turbopump driven. For the RDF – LOX and RDF – S – LOX concepts, a cycle could be used or LOX could be supplied through a pressurized tank. Another option would be an H_2O_2 gas generator to drive the pump or a battery-powered system like in the Electron rockets. A study [117] shows that, especially for lower thrust engines, electric cycles are competitive with gas-generator cycles. The batteries would be transported from Earth with the engine itself but could be charged using solar panels on the lunar surface.

5.3.2 Cooling

Combustion of metals creates very high temperatures in the combustion chamber. Many rocket engines use regenerative cooling by the fuel [118]. Standard regenerative and film cooling strategies are also proposed for engines using LOX as the coolant. Despite the high reactivity of oxygen with any material at high temperatures, it is possible to use specific copper alloys [119] and was demonstrated in successful tests of the engines with LOX cooling [120]. Multiple companies are working on innovative copper alloys that are 3D-printable and function well with LOX at high temperatures, as shown in preliminary tests [121]. Different cooling solutions will be required for the different concepts. In a first step, the temperatures at different cross sections were analyzed over the O/F mass ratio range for the RDF – LOX concept and are presented in Figure 5.8. An increase in the O/F mass ratio decreases temperatures significantly, at the nozzle exit by almost 1000 K when going from a O/F mass ratio of 2 to 5, with an even larger decrease when approaching a ratio of 10. This is

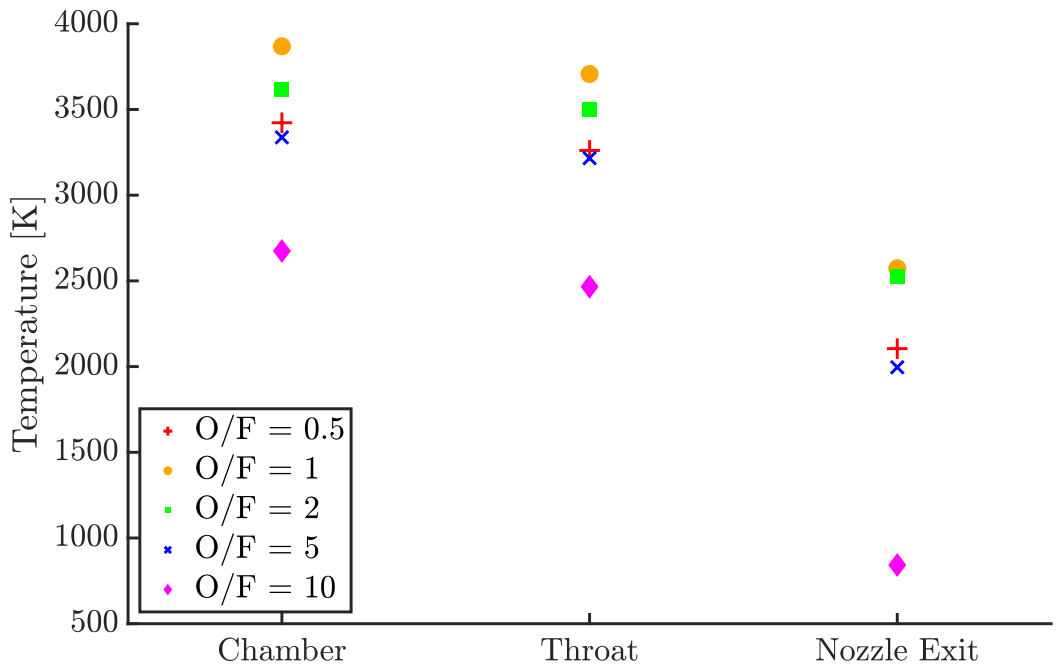

Figure 5.8: Temperatures of the flow at different cross sections for the A-11 RDF$-O_2$ thermodynamic calculations.

another indication that such an engine should be operated fuel-lean, where it is much easier to cool while only a moderate loss in I_{sp} is observed.

In addition to the oxygen flow through a cooling jacket, it is also proposed to inject the oxygen through a porous wall of the nozzle (using ablative materials for the remainder of the nozzle) to achieve the proposed fuel-lean regime and create a film for cooling. A possible implementation is schematically shown in Figure 5.9.

The nozzle materials will have to be chosen depending on the implemented cooling solution. Using oxygen as the coolant will lead to oxidization of the nozzle materials and could only be mitigated by using ceramic liners or, at the minimum, ceramic coatings for a metal liner. A specific analysis of suitable materials is outside the scope of this thesis and is discussed specifically for oxygen cooling in [119, 122]. Using an ablative nozzle or an ablative part at the end of the nozzle is a simpler solution than a sophisticated cooling design. However, some ablative materials that are used in current engine designs might burn vigorously with the

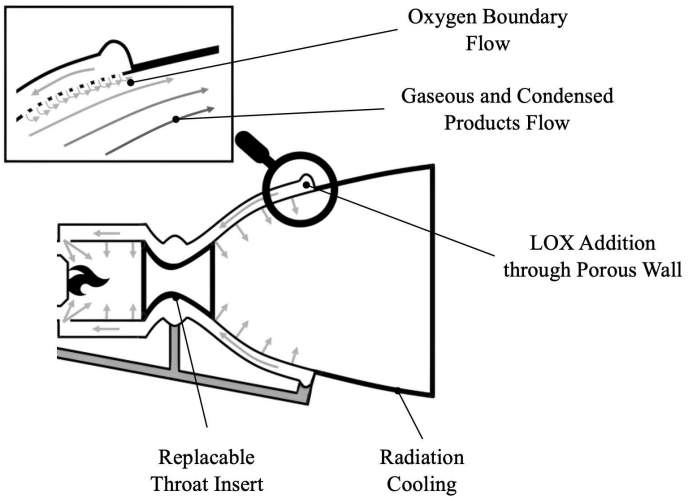

Figure 5.9: Proposed cooling solution for an RDF – LOX rocket engine.

oxygen-rich exhaust flow.

A similar solution can be implemented for a RDF – S – LOX hybrid engine and the brimstone rocket. Chamber temperatures are on the same order of magnitude, and the same trends in temperature at all different cross sections can be observed (temperatures are lower at any point, see Figure A.6 in the Appendix).

The only engine that has to fully rely on ablative cooling is the RDF – S solid rocket engine, as there is no coolant available. This is common practice in any solid engine, and chamber temperatures for RDF – S are not predicted to be particularly high.

5.3.3 Erosion

Any rocket engine where either the oxidizer, or fuel, or both are solid suffers from mechanical and chemical erosion processes. This problem is closely related to the one mentioned in the previous subsections (deposition and cooling). The most commonly proposed solution is to integrate ablative inserts into the design, especially in the throat area, which is shown in Figure 5.9. The problem is discussed extensively in the literature, for instance in [123] and, specifically, for an Al/LOX engine in [80]. When operating at high O/F mass ratios, as proposed, the oxygen will create a jet force and attenuate the erosion problem.

5.3.4 Condensed Combustion Products

Most of the combustion products will be condensed; therefore, deposition on the nozzle walls is a concern. Any deposition would increase the mass of the system, inhibit the flow, and therefore decrease the performance of the system. A study by Miller and Herr investigated deposition in aluminum–steam and magnesium–steam rocket engines, two metals that are also present in RDF [110]. There was much less deposition in the engine using magnesium fuel, as the melting point of magnesia (3125 K) is much higher than that of alumina (2345 K). For RDF, given that adiabatic flame temperatures with oxygen significantly surpass the melting points of alumina and silica, there might be significant deposition. Indeed, the thermodynamic calculations indicate predominantly liquid phases within the combustion chamber. However, at the nozzle exit, where temperatures are much lower, there are much more solid products, which may decrease the deposition. With increasing the O/F mass ratio from 3 to 10, the solid fraction at the nozzle exit increases from 24% to 99% (Table 5.1).

Table 5.1: Phase of the condensed products at different cross sections for the A-11 RDF + O_2 thermodynamic calculation.

Cross Section	**Phase**	**O/F Mass Ratio**					
		0.5	**1**	**2**	**3**	**5**	**10**
Chamber	Liquid	100.0%	100.0%	100.0%	100.0%	100.0%	80.0%
	Solid	0.0%	0.0%	0.0%	0.0%	0.0%	20.0%
Nozzle Exit	Liquid	48.0%	58.5%	70.0%	76.0%	34.0%	1.0%
	Solid	52.0%	41.5%	30.0%	24.0%	66.0%	99.0%

5.3.5 Two-Phase Losses

Should the formed particles reach a sufficient size, they will not maintain the same velocity as the gas, and the thermal equilibrium of the exhaust products is also disturbed. The velocity lag leads to a lower exhaust impulse for these particles and, hence, a lower performance. The velocity lag is typically larger than the thermal lag [124, 125]. The two-phase loss in specific impulse depends on a combination of the two types of lag [126]: for the minimum loss, there

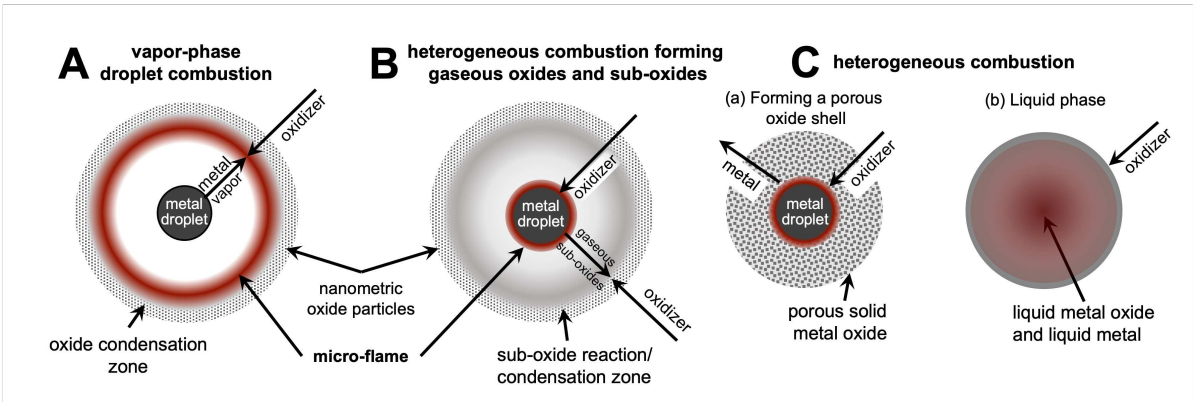

Figure 5.10: Modes of particle combustion in the small Biot number regime. The oxidizer is typically oxygen. Modes A and B produce nanometric solid metal-oxide combustion products in a halo around the droplet, while both variants of Mode C produce micron-sized oxides. Adapted and modified from [66].

is complete heat transfer but still a loss due to the condensed particles not expanding in the nozzle. For maximum loss, the condensed particles are not accelerated, and there is no heat transfer.

Two-phase losses are estimated to influence the performance at maximum by 2% assuming that the product particles are smaller than 1 μm [114]. As previously described, the final particle size after the reduction process will be in the range of 75 – 300 μm [39]. Therefore, to minimize two-phase losses, one should attempt to generate nanoscale combustion products.

Three combustion modes have been identified for metal fuels, which are reproduced in Figure 5.10 and are described in detail in [66]. A second subcategory has been added for Mode C (denoted with (b)), where the metal burns heterogeneously in the liquid phase, forming a liquid metal oxide. Iron is one of the metals that burns in that manner. As the liquid oxide and liquid metal are miscible to a certain extent and there is no unambiguous micro-flame, it is shown as a continuum with a flame throughout. An assessment was performed for the combustion mode of the pure metals with oxygen based on the criterion (T_f / T_b) [73] at both 1 atm and 20 atm, which is shown in Figure 5.11. When burning the pure metals by themselves, we expect all of them but silicon and iron, which burn heterogeneously, to burn in vapor phase.

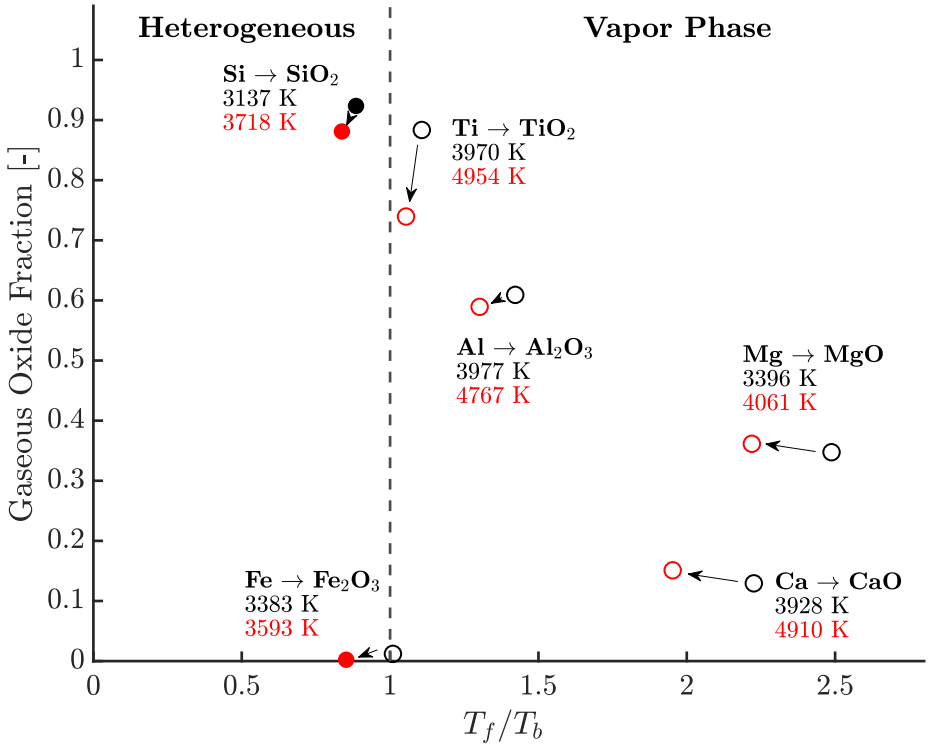

Figure 5.11: Assessment of the combustion mode at stoichiometry based on the criterion that the metal burns in vapor phase when the flame temperature (T_f) is higher than the boiling temperature of the metal oxide (T_b). The black circles correspond to a pressure of 1 atm, while the red circles correspond to a pressure of 20 atm. The temperatures below the oxidation reactions indicate the flame temperature T_f.

However, since we are burning an alloy, we will not achieve the high flame temperatures of the individual metals. The predicted flame temperatures for A-11 RDF at different O/F mass ratios and the chosen chamber temperature of 20 atm were compared with the boiling points of the metals as shown in Table 5.2.

It is seen that, at all O/F ratios, the T_f/T_b ratio is >1 for calcium and magnesium and <1 for titanium, silicon, and iron. Therefore, Ca and Mg would burn in vapor phase and generate nanoscale oxides, while Ti, Si, and Fe would burn heterogeneously.

Table 5.2: Boiling points (T_b) of the individual metals at 20 atm compared to the adiabatic flame temperatures (T_f) of A-11 RDF burning with O_2 at different O/F mass ratios and the same pressure. The boiling points for the metals at 20 atm were obtained with an iterative procedure in the thermodynamic solver.

O/F Mass Ratio	**T_f [K]**	**T_f/T_b**					
		Ti T_b = 4702 K	**Si** T_b = 4439 K	**Fe** T_b = 4066 K	**Al** T_b = 3662 K	**Ca** T_b = 2515 K	**Mg** T_b = 1882 K
0.5	3422	0.73	0.77	0.84	0.93	1.36	1.82
1	3868	0.82	0.87	0.95	1.06	1.54	2.06
2	3616	0.77	0.81	0.89	0.99	1.44	1.92
5	3337	0.71	0.75	0.82	0.91	1.34	1.77
10	2675	0.57	0.60	0.66	0.73	1.06	1.46

Titanium

According to the literature, titanium particles always explode after a certain period of heterogeneous combustion, generating a lot of burning tiny fragments [67]. As a result, combustion of titanium particles produces much smaller oxide particles than other heterogeneous combustion processes.

Silicon

Combustion of silicon is known to involve the formation of the intermediate gaseous product SiO, which leads to the production of nanoscale SiO_2 particles [127]. Therefore, combustion of Si, though occurring heterogeneously, also generates nanoscale products, as represented by Mode B from Figure 5.10.

Aluminum

For aluminum, the T_f/T_b ratio is close to 1, which makes the assessment difficult. However, combustion of aluminum is known to include the formation of intermediate gaseous suboxides [128], so it is also promising from this point of view.

Calcium and Magnesium

These two metals are predicted to burn in vapor phase (Mode A) even at higher O/F mass ratios and consequently lower chamber temperatures. Combustion studies on the burning mode or combustion behavior of calcium could not be identified that support this assumption. Calcium in powdered form is pyrophoric and thus very difficult to store safely. For the same reason, an experimental investigation of its combustion with air or oxygen is challenging.

Iron

The low gaseous mass fraction of the oxides of iron and calcium indicates the presence of more solid particles. At higher pressures, iron is predicted to burn heterogeneously, and based on the low gaseous mass fraction in Mode C. Single particle combustion experiments of iron in up to 100% oxygen have shown that the bulk of product particles is still micron sized and only $< 10\%$ are nanoparticles [95]. They have also shown that the combustion mode is not well described by Mode C (a), therefore, Mode C (b) has been added to Figure 5.10. Thermodynamic calculations for combustion of A-11 RDF at 20 atm have shown that the gaseous fraction of iron oxides is equal to 0.90, 0.23, 0.16, and 0 at the O/F mass ratios of 1, 2, 5, and 10, respectively. Small values indicate that most iron oxide particles will be of the same scale as the initial fuel particles.

In conclusion, while the assessment of the exact magnitude of the two-phase losses is not possible, this analysis serves as a first assessment of the expected combustion behavior of RDF. It is recommended to verify the combustion mode with experimental studies. However, based on our preliminary assessment, it becomes clear that two-phase losses will be a minor issue for the rocket engine design.

5.4 Comparison

The RDF – LOX bipropellant rocket engine is predicted to have the highest performance with a peak I_{sp} of 256 s at an O/F mass ratio of 4. Additionally, it offers restarting capabilities,

but the design is complex from an engineering perspective with the need to develop a reliable powder feeding system.

The RDF – S – LOX hybrid rocket engine has a simple design compared to the RDF – LOX concept, with a slightly reduced peak I_{sp} of 252 s at an O/F mass ratio of 4 and a marginally lower chamber temperature of 3447 K. Throttling and restarting are not inherently possible with the hybrid system, as metal and sulfur can self-sustain combustion. However, one can deliberately choose a Me – S mixture ratio that will not support self-sustained flame propagation and will not achieve peak performance either. Then, the system can be quenched by cutting the oxygen flow and restarted.

S – LOX is a suitable rocket engine design when access to sulfur is abundant. The performance, with a I_{sp} of 243 s at an O/F ratio of 1.1, is sufficient for missions to LLO or hopper missions. The combustion temperature reaches a peak of 3633 K at the optimal O/F fuel mass ratio. As with all bipropellant concepts, it is more complex than a hybrid or solid engine but offers restarting capabilities.

RDF – S as a solid rocket engine is predicted to have the lowest performance with an I_{sp} of 100 – 120 s at a combustion temperature of 2000 – 3000 K. Solid rocket motors are simple to design but can usually neither be throttled nor restarted. The primary drawback of any system using sulfur is that its extraction necessitates a separate process from the rest of the RDF. The reduction process for RDF is required for oxygen generation on the lunar surface, with RDF serving as a convenient byproduct. However, this convenience does not extend to sulfur extraction. While exhibiting a much lower performance, the solid system excels in one aspect: propellant storability. The cast RDF – S propellant grain could be stored for nearly indefinite periods and would be well-suited as an emergency system, eliminating the need for propellant production close to the mission launch date.

The different concepts, their possible applications, as well as their benefits and drawbacks, are concisely summarized and compared in Table 5.3 below.

[1]The exact calculations for RDF-sulfur could not be run, therefore a range is provided.

Table 5.3: Comparison matrix for all proposed rocket engine designs.

Concept	Performance (ISP)	Complexity	Throttling/ Restart
RDF + LOX (bipropellant)	Highest Peak I_{sp} = 256 s at O/F = 4 and T_c = 3416 K	Complex	Both possible
RDF + S + LOX (hybrid)	High Peak I_{sp} = 252 s at O/F = 2.5 and T_c = 3447 K	Medium complexity	Throttling possible, restart only possible at specific conditions
S + LOX (bipropellant)	Medium to High Peak I_{sp} = 243 s at O/F = 1.1 and T_c = 3633 K	Complex	Both possible
RDF + S (solid)	Low Peak $I_{sp} \approx$ 100-120 s at T_c = 2000 - 3000 K[1]	Simple	Not possible

Concept	Maintenance/ Reusability	Safety	Application
RDF + LOX (bipropellant)	+	Higher failure risk	Return to LLO and hopper
RDF + S + LOX (hybrid)	o	Reliable	Return to LLO and hopper
S + LOX (bipropellant)	o	Higher failure risk	Return to LLO and hopper
RDF + S (solid)	-	Most Reliable	Hopper and emergency system

6 Experimental Studies

The main focus of this thesis has been on the theoretical study, and an experimental study meeting the standards for journal publication could not be completed. However, some progress has been made, and for completeness, the preliminary results of three different experimental campaigns are documented in this section and related to the conceptual work on the rocket engines.

6.1 Thermochemical Analysis of Al/Si Alloys (TGA and DSC)

Thermogravimetric Analysis (TGA) and Differential Scanning Calorimetry (DSC) are two commonly used techniques in materials science and chemistry. TGA involves heating a sample under controlled temperature conditions while measuring its weight change as a function of temperature or time. This technique is used to determine various properties, such as decomposition temperature, thermal stability, and moisture content, of a material. DSC, on the other hand, measures the difference in heat flow between a sample and a reference material as a function of temperature. It is used to study phase transitions, melting points, glass transitions, reaction kinetics, and purity of materials. Both techniques provide valuable insights into the thermal behavior and properties of materials, aiding in their characterization and understanding of their reactivity.

In the context of the ISRU project, it was of interest to understand the reactivity and oxidation processes of the RDF. As a starting point, we used aluminum/silicon alloys for the experimental campaign. The work aimed to build on a previous publication [129] where the Al88Si12 alloy was analyzed to assess how an aluminum/silicon alloy compares to pure aluminum from a thermochemical perspective and how that might influence its suitability

as a rocket fuel. Our work included Al75Si25, Al66Si34, and pure silicon in addition to the powders analyzed in the previous paper. If possible, it would be of scientific value to obtain a reduced regolith sample from NASA to conduct a thermal characterization of an RDF in the future.

The following five powder samples were obtained from different suppliers for the experiments (unfortunately, no uniform particle size could be obtained for the different compositions, and the number of suppliers selling such powders is very limited):

- Aluminum powder, $3-4.5\,\mu$m, 97.5% purity (Alfa Aesar)
- Silicon powder, <325 mesh, 99.5% purity (Alfa Aesar)
- Al88Si12 alloy powder, eutectic composition, $5\,\mu$m, spherical, (SkySpring Nano Materials)
- Al75Si25 alloy powder, $<150\,\mu$m (Goodfellow AL15-PD-000110)
- Al64Si36 alloy powder, $<150\,\mu$m (Goodfellow AL14-PD-000110)

Two runs were conducted in pure oxygen for each of the different samples. An STA (Simultaneous Thermal Analyzer, Netzsch STA 449 Jupiter) was used for the measurements, and both TGA and DSC curves were documented. The resulting curves and conditions were the following:

- TGA in the temperature range 25°C to 1500°C with a heating rate of 10 K/min
- DSC in the temperature range 25°C to 1500°C with a heating rate of 10 K/min
- DTG in the temperature range 25°C to 1500°C with a heating rate of 10 K/min

For all the following results, the two runs have been averaged. It is common practice to average five runs for such measurements, therefore, these preliminary results might not be fully statistically representative.

6.1.1 TGA Curves

The TGA curves for all five samples at the heating rate of 10 K/min are plotted in Figure 6.1.

The dashed line shows the theoretical calculated mass gain that is expected after oxidation. Based on the slow oxidation of silicon (since the STA does not reach temperatures higher than 1500°C), the assumption can be made that mainly aluminum will oxidize within the alloys. In that case, the theoretical mass gain is shown by the dotted lines. The colors of the lines match with the corresponding TGA curves.

The curves for Al100 and Al88Si12 were compared with the previous measurements performed in the previous study [129]. We encountered some peculiarities in the measurements: the first one is the additional mass gain after the primary oxidation process (indicated by a plateau in the mass gain). Theory does not predict any further oxidation that could lead to a mass gain approaching 200% at higher temperatures. This is consistently visible for all samples (besides silicon which does not reach a plateau below 1500°C). Aluminum, within some tolerance, seems to fully oxidize, while the curve for Al88Si12 indicates that only aluminum oxidizes up to the first plateau. Al75Si25 shows even less reactivity and oxidizes less, while

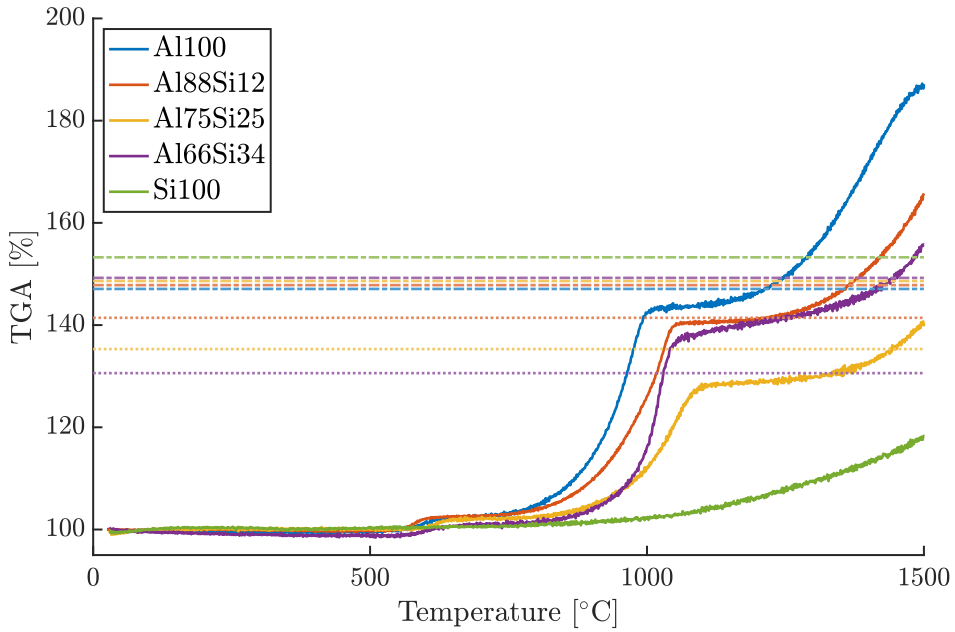

Figure 6.1: TGA data for the five samples in pure oxygen at a heating rate of 10 K/min.

Al66Si34 shows significantly higher reactivity, which is almost on par with Al88Si12. Silicon starts oxidizing very late (at $> 1000°C$) and it appears that higher temperatures are required to achieve full oxidation. These observations are consistent between the two experimental runs.

Based on the limited data, it is difficult to pinpoint why a higher reactivity was observed for Al66Si34. Intuitively, based on the difference between Al100 and Al88Si12, one would expect the reactivity to decrease with a higher silicon content in the alloy. Further measurements are required to verify the higher reactivity of Al66Si34 and find a coherent explanation for its oxidation behavior.

6.1.2 DTG Curves

In order to analyze the reaction rate during the oxidation process, the DTG curves were plotted, which is shown in Figure 6.2. DTG curves are the derivative of the TGA curves.

As previously discussed, it remains unclear why there are further reactions (and for

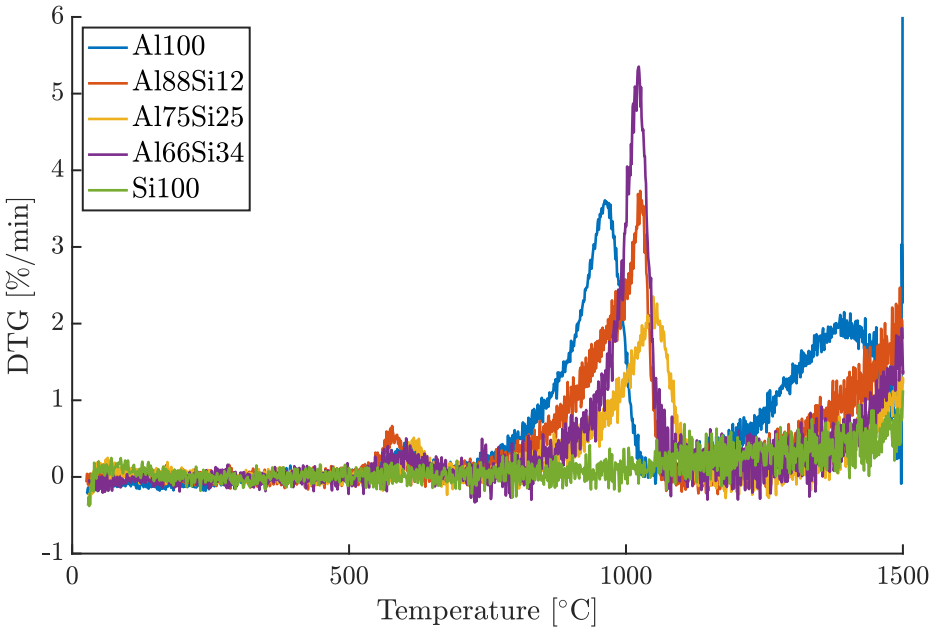

Figure 6.2: DTG curves for all five samples at a heating rate of 10 K/min, which are derived from the previous TGA curves.

aluminum even a second plateau) after the primary oxidation process. Since the DTG curves are a proxy for reactivity, it is once again visible that Al66Si34 seems to react more strongly than the other samples, even more than Al100.

6.1.3 DSC Curves

As a final step, the DSC curves were evaluated. Due to a falling baseline trend in the measurements, which was also observed during calibration runs, the data was smoothed using MATLAB. This allows for a better visualization of the relevant features of the DSC curve: the endothermic and exothermic reactions. The result is shown in Figure 6.3.

We can clearly observe the melting points (small endothermic, i.e., negative peaks) of the aluminum sample as well as the alloys at around between 600 – 700°C, which is consistent with the literature values. Silicon melts at 1414°C just before its oxidation starts, so the endothermic peak due to melting appears just before the exothermic peak of the oxidation. The alloys seem to oxidize at a slightly higher temperature than aluminum, and we can again observe the high reactivity of the Al66Si34 sample, as indicated by the area under the exothermic reaction peak. The higher energy release when approaching 1500°C is due to the

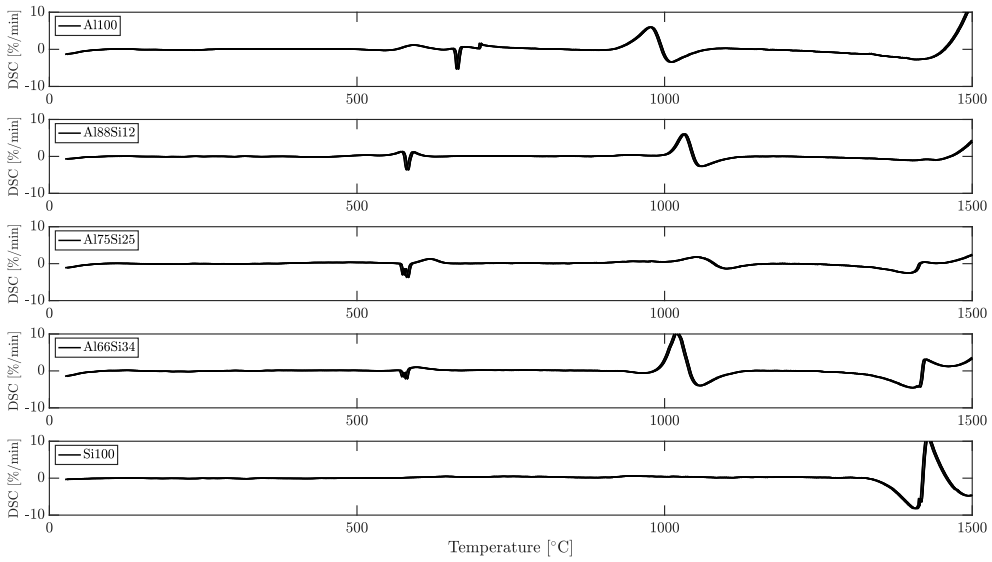

Figure 6.3: DSC curves for the five samples at a heating rate of 10 K/min.

smoothing algorithm, which does not fully subtract the falling baseline from the measurement. An interesting observation is the high reactivity of silicon when it starts to oxidize, which is not as visible in the TGA curves. This peak might also be enlarged due to the smoothing algorithm and thus erroneously indicate a high energy release.

6.2 Ignition Experiments

The second experimental campaign focused on validating the combustion characteristics (and combustion mode) of aluminum, silicon, and alloys. As previously discussed, laminar aluminum (premixed) flames are well understood, but there is no published research on laminar silicon flames, even though one has been stabilized recently at the AFL (Figure 2.5). Additionally, a study was published on silicon being burned in a turbulent manner [127]. A mixture of the two metals has not been investigated, neither in the form of an alloy nor a binary mixture.

The experimental setup in the combustion chamber resembles the environment at the exit of the fluidized piston injection system, where powder is entrained with oxygen right before injection into the combustion chamber. Therefore, this is a first experimental campaign to understand the ignition and combustion behavior of such a configuration.

6.2.1 Laser Ignition of Metal Powders in Pure Oxygen

The ignitability of silicon and aluminum/silicon alloys in oxygen was investigated in a windowed chamber equipped with a 60 W CO_2 laser (Synrad Firestar Ti-60), which was used recently to study the combustion of magnesium and lithium powders [130, 131]. As a reference, aluminum was also ignited in the same environment. The combustion was qualitatively documented using a high-speed camera (Phantom v1210), and the burnt samples were analyzed with scanning electron microscopy (SEM) and energy dispersive X-ray spectroscopy (EDS). The same powders that were used for the TGA and DSC measurements (details in Section 6.1) were also used for the ignition experiments

Combustion experiments were conducted with the following steps:

1. The sample is placed in the chamber on a high-temperature resistant ceramic plate and aligned so that the center of the sample is directly under the laser beam. The powder is placed in loosely packed form and at variable thicknesses.

2. The chamber is evacuated with a vacuum pump to a pressure of approximately 1 – 2 Torr (133 – 267 Pa).

3. The chamber is flushed with ultra-high purity oxygen (99.99% purity) until it equilibrates at a pressure of 675 Torr (90 kPa, which is the standard atmospheric pressure in El Paso, TX).

4. The laser is activated and fired for 2 s, thus applying 64 J of energy to the sample. After that the laser is turned off.

5. The ignition and combustion processes are recorded with the high-speed camera at 1736 fps.

6. The chamber is purged with nitrogen for 1 min, and then the sample is removed from the combustion chamber.

All of the samples ignited and combusted from the center of the powder sample toward the outside. Two types of experiments were conducted: one with a loosely packed scoop of hemisphirically shaped powder, and one with a flat powder sample, as shown in Figures 6.4a and 6.4b.

The hemisphirical shaped samples were approximately 1 g in mass, while the flat powder samples were 0.25 g in mass. Aluminum could not be burned in a controlled manner as a 1 g hemisphirical sample, while silicon burned in a more controlled manner and showed more steady flame propagation in the larger mass sample. The burning process timelapse of the hemisphirical sample is shown in Figure 6.5.

The combustion process over a time frame of three seconds is shown in Figures 6.6a, 6.6b, 6.6a, 6.6d, and 6.6e for all the powder samples. Due to the violent combustion behavior of aluminum, the sample mass for the alloys was reduced (from 1 g to 250 mg), and the shape shown

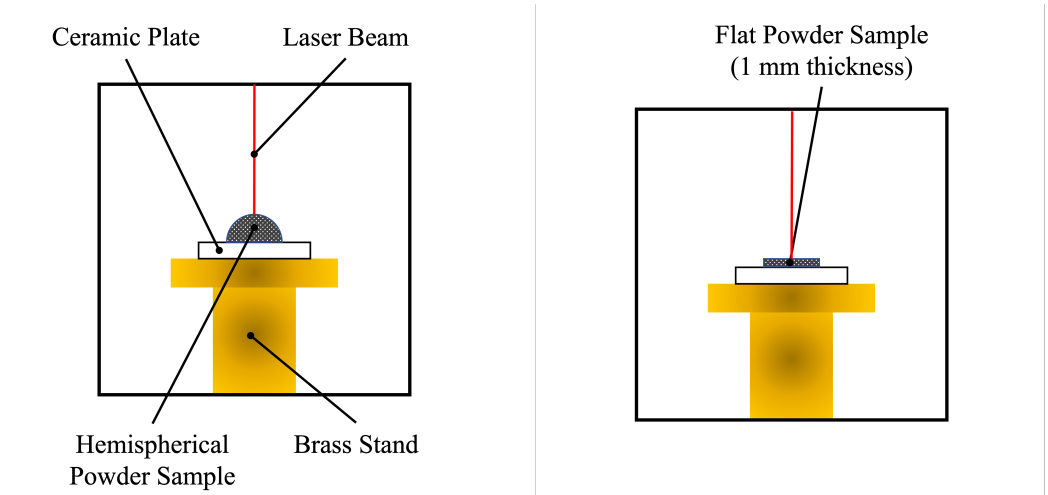

(a) Hemisphirical powder shape

(b) Flat powder shape

Figure 6.4: Experimental setup inside the combustion chamber.

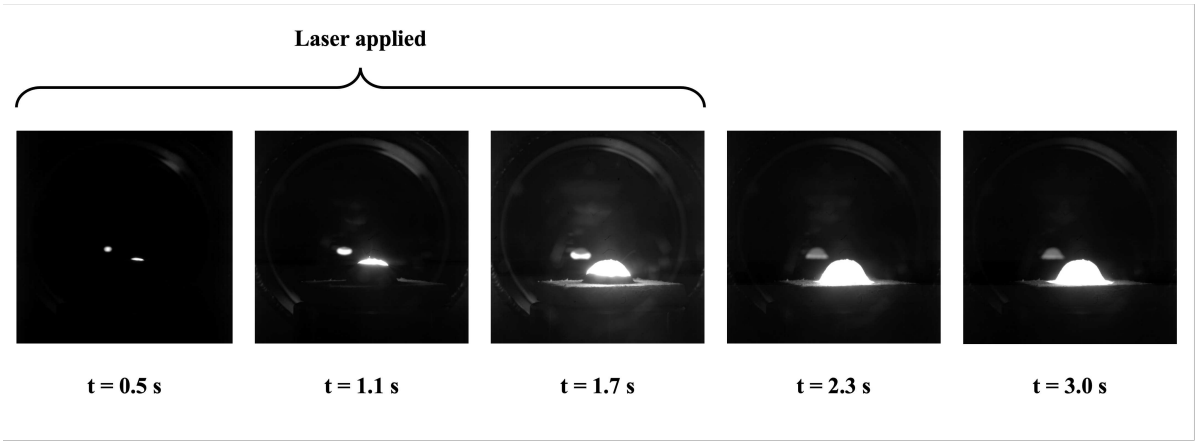

Figure 6.5: Silicon powder (≈ 1 g) burning in a 100% oxygen atmosphere.

in Figure 6.4b utilized. As one can see, silicon burns consistently (best visible in Figure 6.5) and the flame propagates slowly through the material; for aluminum, the combustion process is violent.

The observations are in line with the combustion modes for aluminum and silicon, which were discussed in Section 5.3.5. The violent combustion process is a sign of vapor phase combustion for aluminum, while silicon burns more consistently and heterogeneously in Mode B with a multi-phase surface reaction. These macroscopic observations of the combustion

behaviors in the ignition experiment are shown in Figures 6.6e and 6.6a.

All the alloys ignited with the same experimental procedure, and their combustion behavior resembled that of pure silicon; the flame propagated rather consistently through the powder sample, and no sparks or explosion-like behavior could be detected, as shown in Figures 6.6b, 6.6a, and 6.6d.

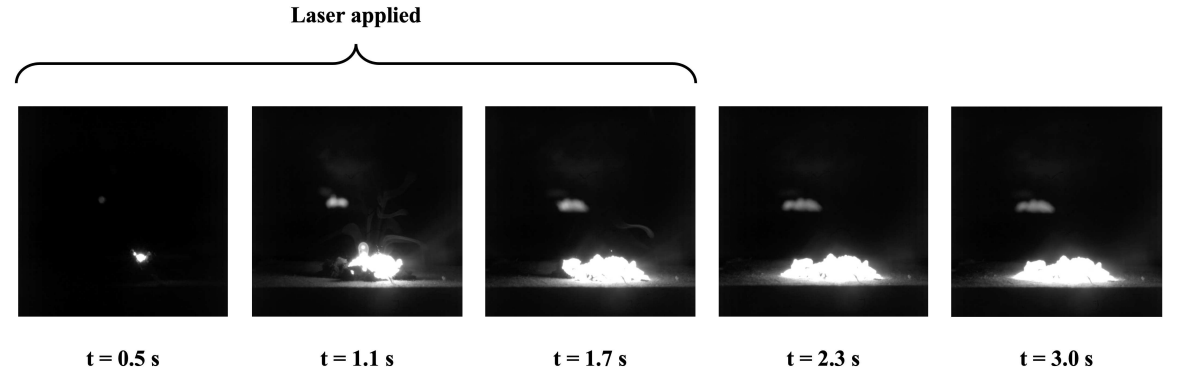

(a) Silicon powder ($\approx$ 250 mg) burning in a 100% oxygen atmosphere.

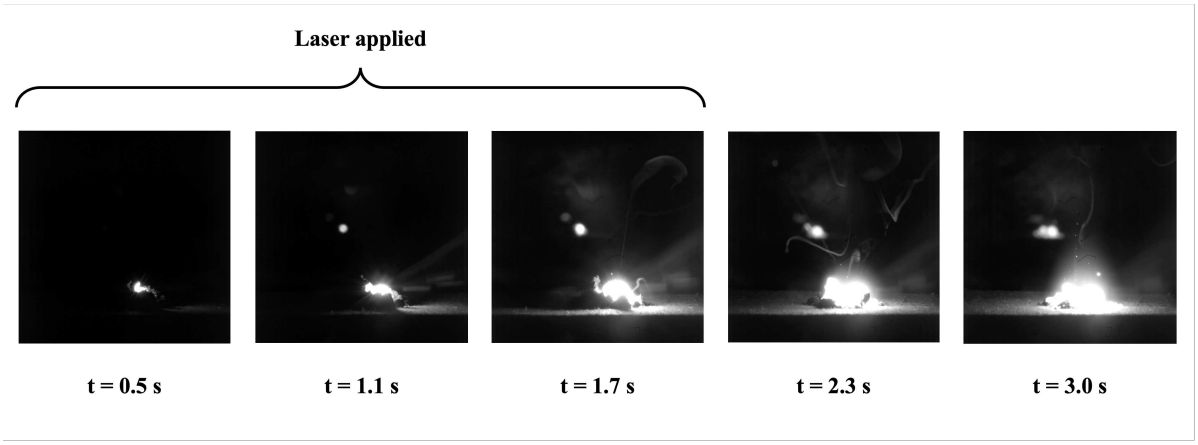

(b) Al66Si34 alloy powder ($\approx$ 250 mg) burning in a 100% oxygen atmosphere.

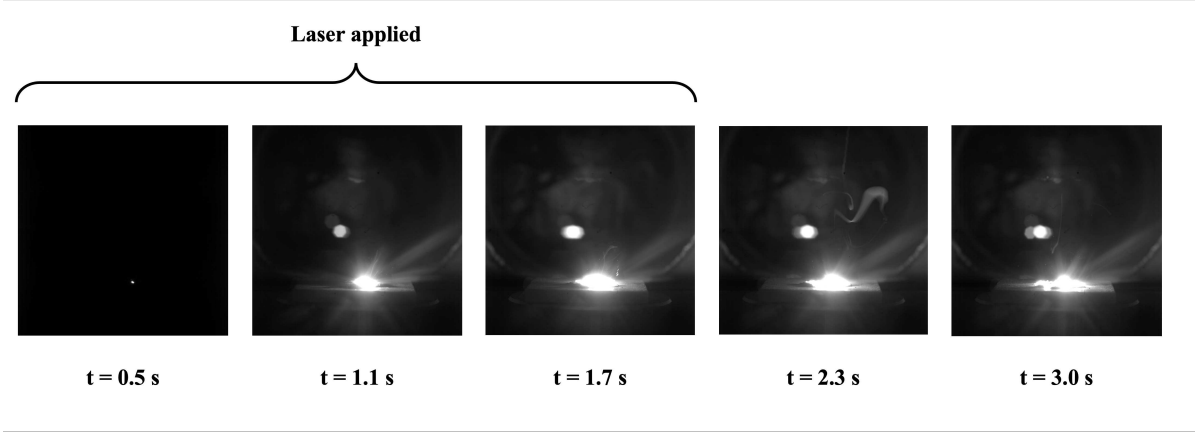

(a) Al75Si25 alloy powder (≈ 250 mg) burning in a 100% oxygen atmosphere.

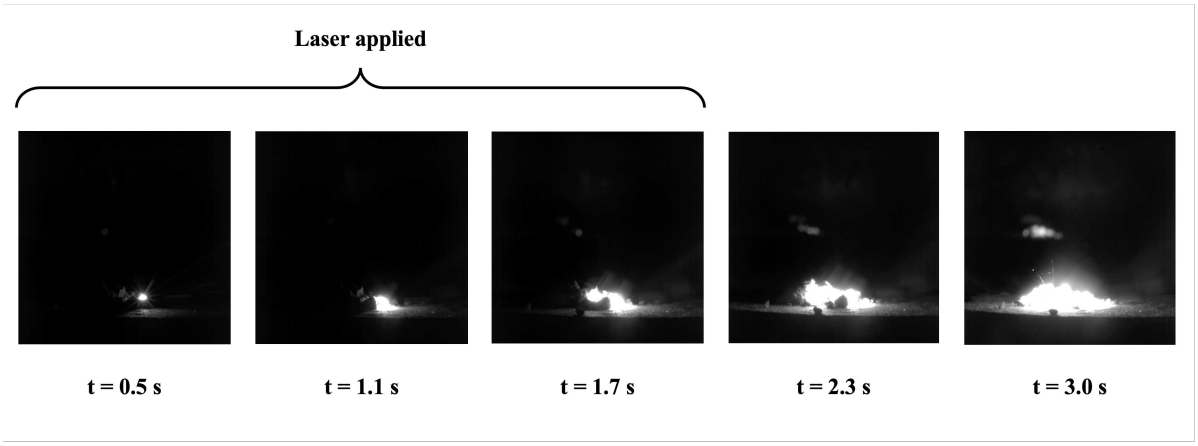

(d) Al88Si12 alloy powder (≈ 250 mg) burning in a 100% oxygen atmosphere.

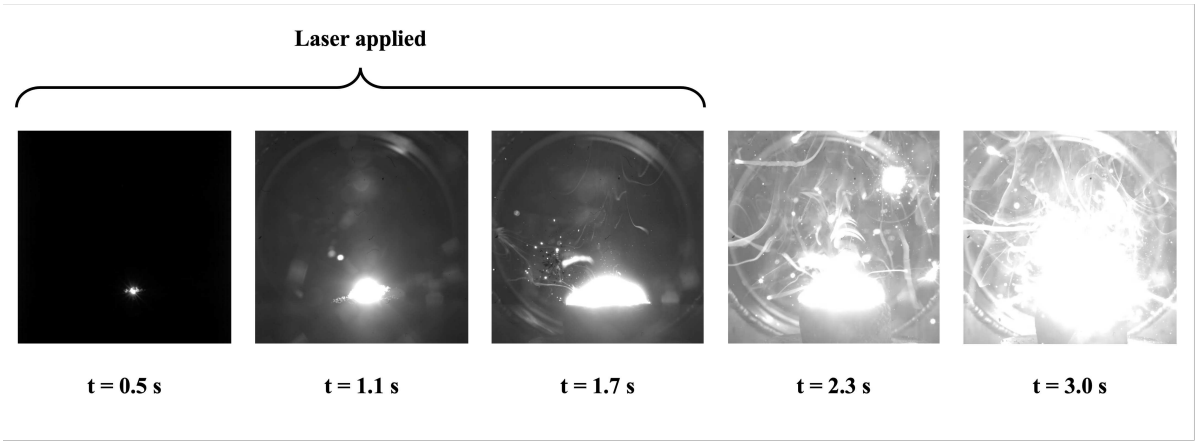

(e) Aluminum powder (≈ 250 mg) burning in a 100% oxygen atmosphere.

Figure 6.6: Combustion process of different samples captured by the high-speed camera.

Table 6.1: Theoretical assessment of the combustion modes of the alloys. (A) indicates vapor phase combustion in Mode A, and (B) indicates heterogeneous combustion in Mode B from Figure 5.10.

Oxide	$\mathbf{T_b}$	$\mathbf{T_f/T_b}$				
	[K]	**Al100**	**Al88Si12**	**Al75Si25**	**Al66Si34**	**Si100**
$\mathbf{Al_2O_3}$	2792	1.42 (A)	1.40 (A)	1.39 (A)	1.38 (A)	-
$\mathbf{SiO_2}$	3538	-	1.11 (A)	1.10 (A)	1.09 (A)	0.89 (B)

This is peculiar because, even though the alloy is burning at a lower temperature, the flame temperature is still significantly higher than the boiling point of aluminum. Therefore, aluminum should still burn in vapor phase, but this is not the case based on the macroscopic observations. Based on the calculations, even silicon should burn in vapor phase because the alloy burns hotter than pure silicon. Contrary to the expectations from the theoretical calculations, on a qualitative level that can be captured with the high-speed camera, no difference could be detected between the different compositions. The ratios and the associated combustion mode for aluminum and silicon at the different alloy conditions are shown in Table 6.1.

The most noteworthy aspect of the experimental studies is that even a small percentage of silicon in an alloy changes the combustion behavior compared to pure aluminum, but in a manner that is not predicted by theory. Even the combustion of the Al88Si12 alloy resembles the combustion behavior of silicon more than that of aluminum. More studies are required to gain a deeper understanding of these preliminary observations and if the combustion is actually heterogeneous on a microscopic level.

6.2.2 Imaging of the Samples

The samples were imaged using SEM and EDS. When looking at the raw materials, one could see that the structures of the aluminum/silicon alloys differ significantly from those of pure silicon. The alloy particles are spherical, while the silicon particles are not, as shown in Figures 6.7a and 6.7b. The Al88Si12 alloy is used as a comparison to the silicon particles as

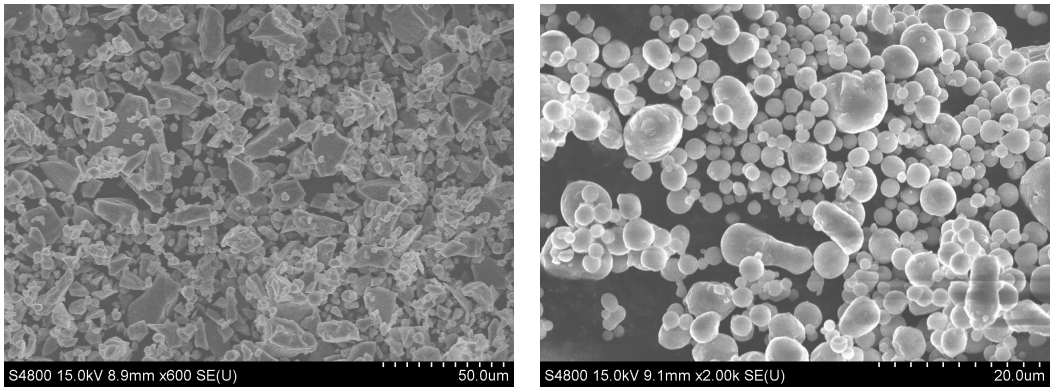

(a) Silicon powder unburnt.

(b) Al88Si12 powder unburnt.

Figure 6.7: SEM images comparing the unburnt materials.

they are similar in particle size, while the other two alloy samples are not.

The oxide samples for the Al66Si34 alloy (chosen since its composition is closest to RDF) show areas where combustion has taken place and areas where almost no combustion is visible; this is probably due to only the surface layer burning, while most of the material underneath did not. As a reference, the unburnt Al66Si34 material is shown in Figure 6.8a. The burnt sample is shown in Figure 6.8b and a color map for the different elements was created by the EDS and demonstrated in Figure 6.8c.

When looking at the percentage of oxides that the EDS detects, it becomes clear that some part of the sample did not burn, as 37% (error 6.5%) aluminum, 27% (error 5.3%) silicon, and 34% (error 2.3%) oxygen are detected (all values by mass). For full combustion at stochiometry (using a thermodynamic software) and the given composition of the material (66% aluminum and 34% silicon), these values should be by mass percentage approximately 32% aluminum, 19% silicon, and 47% oxygen. The oxygen figure in the measurement is lower than the predicted one for full combustion (70 – 74% combustion efficiency within error bounds), which matches the observed areas where the material did not combust. The results are shown in a graphic in Figure 6.8d.

The most important observation is that both silicon and all types of alloys burn and oxidize to some degree. This is consistent with the research studies on aluminum burning in multiple configurations (laminar [64] and turbulent [132], respectively) as well as a recent study on

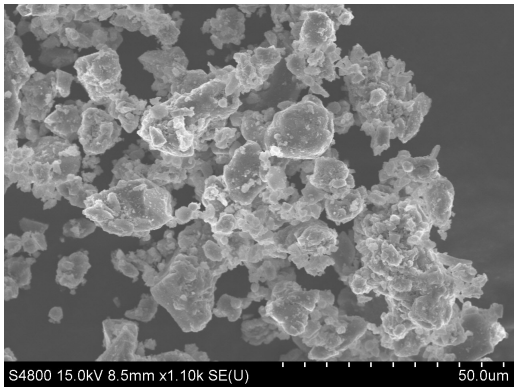

(a) Unburnt Al66Si34 sample

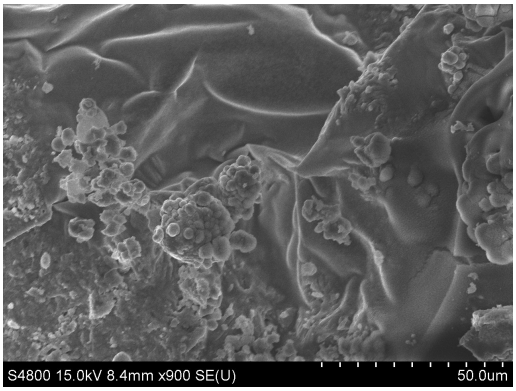

(b) Burnt Al66Si34 particles

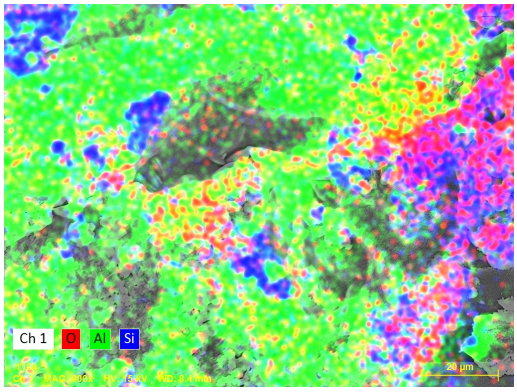

(c) Detected elements with the EDS

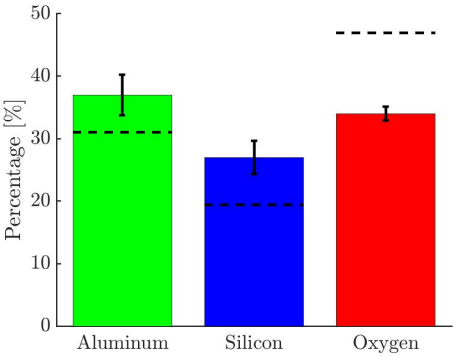

(d) Completeness of combustion

Figure 6.8: SEM and EDS analysis of a sample of the Al66Si34 alloy. Subfigure (a) shows the unburnt sample of the Al66Si34 alloy powder, while Subfigure (b) shows a SEM image after the combustion process. In Subfigure (c), an EDS analysis is performed, and regions where aluminum is detected are shown in green, regions of silicon in blue, and regions of oxygen in red. In Subfigure(d), the completeness of the combustion process is evaluated, with the dashed lines showing the percentages of the elements when complete combustion occurs.

silicon igniting in a dust cloud [127].

6.3 Diffusion Flames

The third experimental campaign was centered on the stabilization of a metal diffusion flame, with the intention of furthering the development of a theory that aligns more closely with our current comprehension of metal combustion. The gaps in the previous theory were described in Section 2.5.2.

The first round of experiments was performed on the AFL laminar metal dust burner that has been used for premixed flame experiments for the last 20 years. A schematic of the burner is shown in Figure 6.9 and a detailed description of its functioning can be found in [64].

In a first attempt to stabilize a diffusion flame, the modifications to the system were kept

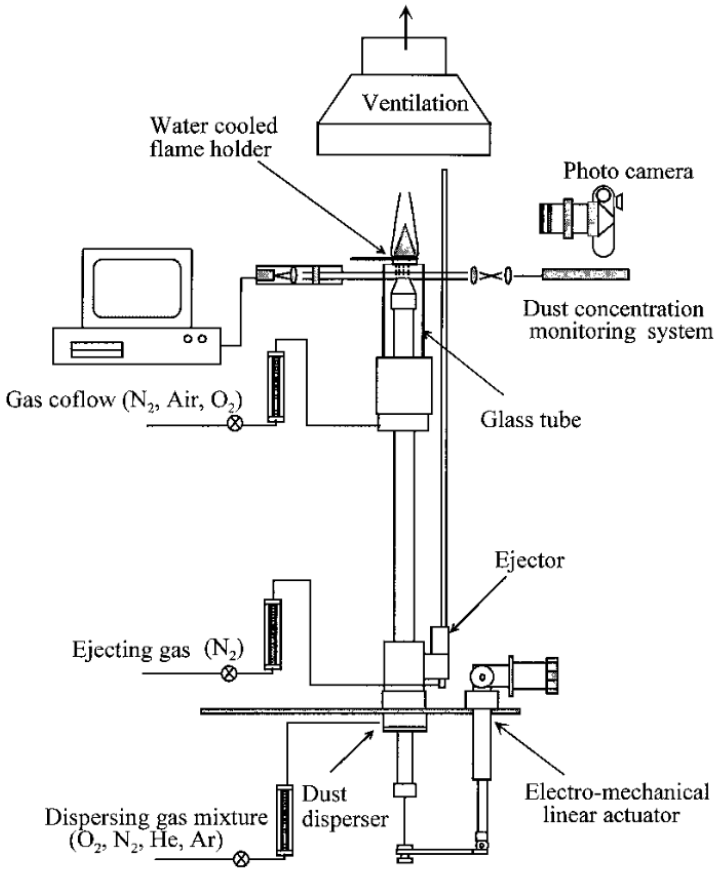

Figure 6.9: A schematic of the old metal dust burner that has been used for premixed aluminum flame experiments. Reprinted from [64].

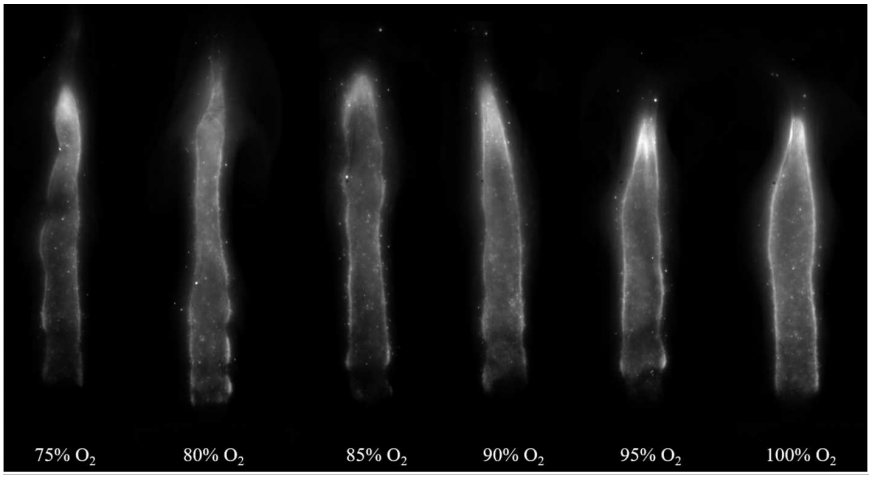

Figure 6.10: Diffusion flames established on the old burner for different oxygen concentrations.

minimal: the co-flow was switched from protective nitrogen to oxygen (the oxidizer that will diffuse into the flame), and the dispersion gas was switched from air (in premixed mode) to nitrogen. A mixing tank was implemented on the oxidizer line to be able to vary the oxygen concentration in the co-flow. We achieved combustion of aluminum for a co-flow of 75 – 100% oxygen for around 30 s. The pictures of the flame, which were recorded with a high-speed camera, are shown in Figure 6.10. A summary of the experimental parameters and different tests that were conducted can be found in Appendix A.2.

However, the flames suffered from a lot of flame instabilities and vortex formation and only kept a stable shape for less than a second. A time lapse for the observed instabilities is shown for the 100% oxygen co-flow diffusion flame in Figure 6.11.

While the investigation of these instabilities is an interesting topic for future research, the unstable flames are not suitable for the investigation we wanted to conduct.

Therefore, the burner was modified, and a new design was used for the second experimental campaign. The main issue that was identified is that the diffusion flame needs to be encased to prevent diffusion of the oxidizer into the room and away from the flame. A glass tube was implemented into the setup, which is moved downwards to be able to ignite the mixture and upwards once ignition has been achieved, encasing the flame. This also allows for varying the ratio of diameters between the dispersion flow tube and the co-flow, which is an important

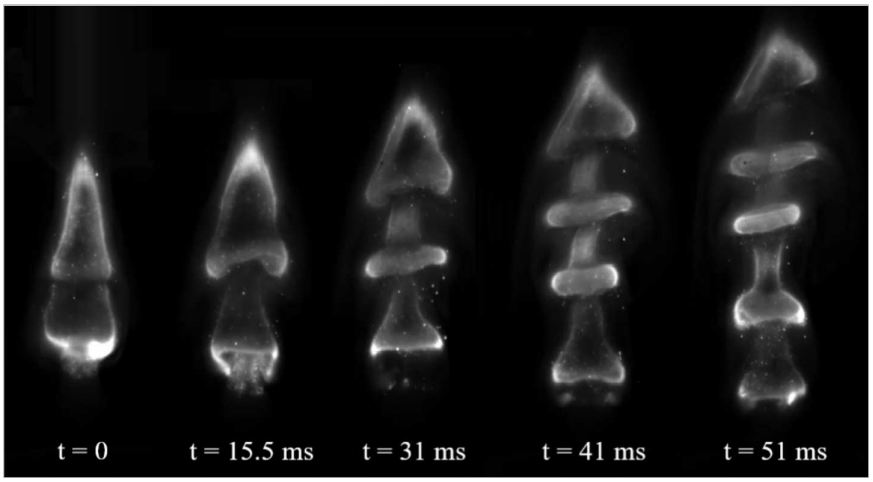

Figure 6.11: Instabilities observed for the 100% oxygen co-flow diffusion flame over its burn duration.

parameter in Burke-Schumann flame theory and a crucial factor for an underventilated or overventilated flame (in gas flame theory). In addition to that, the burner design was modified in other areas. One major upgrade was the inclusion of an ejector, which allows for a direct flow rate variation of the dispersion flow.

The schematic for the new burner design is shown in Figure 6.12[1]. The drawing does not include the glass tube, which is inserted into the assembly, labeled as 4, and can be moved along the dispersion tube and held in place with a set screw.

With this new design, a diffusion flame could be stabilized for one minute in a first set of tests, and a picture of the flame is shown in Figure 6.13.

[1]The author would like to thank C. Mani for providing him with the drawings. He was responsible for redesigning the burner as part of his honors thesis.

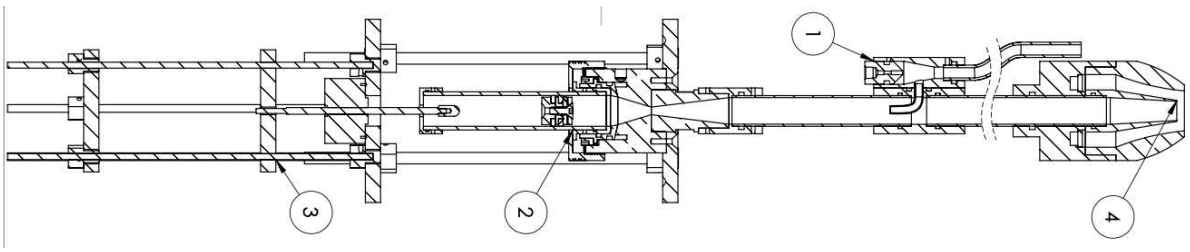

Figure 6.12: Mechanical drawing of the new burner assembly.

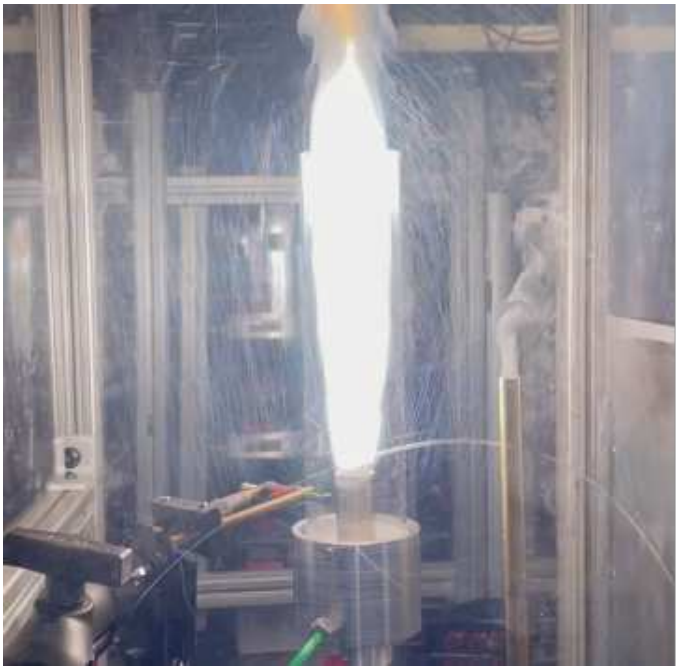

Figure 6.13: A stabilized aluminum diffusion flame on the new laminar burner encased in a glass tube.

However, due to the shutdown of the laboratory, the experimental campaign could never move past those preliminary experiments within the time frame of this thesis. Once the laboratory and experimental setup are operational again, we now have the capabilities to investigate the initial key research question: What governs the stabilization (and possibly the shape/height) of a metal diffusion flame? One key indicator to answer this question could be the minimum oxygen concentration (given by how much oxygen has diffused from the co-flow into the flame) at which the individual particles ignite. This will form the basis for a possible future campaign for laminar dust diffusion flames.

7 Conclusions

Thermodynamic calculations have been conducted for regolith-derived fuels with oxygen. These calculations predict that RDF A-11 (a mixture of metal alloys) achieves a maximum specific impulse of 256 s at an O/F mass ratio of approximately 4. It has been shown that an alloy composition, which will be the fuel after the reduction process, exhibits a slightly lower ISP than an elemental mixture and aluminum, which was previously proposed as an ISRU fuel.

The high combustion chamber temperatures predicted by the thermodynamic calculations also indicate that such an engine would have to be operated fuel-lean to decrease deposition and allow for a simpler cooling system. With increasing O/F mass ratio, the I_{sp} decreases significantly less than chamber temperature. For O/F mass ratios between 4 – 8, chamber temperatures drop by 975 K while the I_{sp} decreases from its peak of 255 s to 230 s.

As the design of an RDF – LOX engine requires a powder feeding system, sulfur was considered as another ISRU fuel. It can act as a binder, an oxidizer for metals, or even as a fuel itself, enabling a wider range of propulsion options. Thermodynamic calculations were performed for different configurations. A key result is that the sulfur content in the fuel should be minimized while still allowing for the RDF to be cast into a solid fuel grain. This can be achieved at approximately 70 vol% RDF and 30 vol% sulfur. The decrease in peak I_{sp} through the inclusion of sulfur is predicted to be approximately 2%, while chamber temperatures are similar. At higher O/F mass ratios, the decrease in I_{sp} reaches up to 10%.

The brimstone rocket is calculated to have a lower performance than the systems including RDF and does not offer any other advantages over these systems. The last proposed design of a RDF – S solid rocket engine design is attractive because of its simplicity but exhibits low performance.

The RDF–S–LOX hybrid rocket engine is a promising design that has not been previously proposed. Advancing the development of this concept, as well as the RDF–LOX concept, to the next stage necessitates addressing several open research questions and conducting experimental studies. In particular, the combustion mechanism of a Me–S grain in an oxygen environment will be investigated on a small rocket test stand in the months after the writing of this thesis.

A Appendix

A.1 Additional Figures for the Thermodynamic Calculations

Thermo and FactSage predict different equilibrium compositions for the alloy A-11 RDF. Therefore, the difference in combustion temperature for the alloy vs. the elemental mixture was verified in both codes, and the results are shown in Figure A.1. The initial conditions are the same that were used for all thermodynamic calculations in the paper. Both codes predict a slight decrease in combustion temperature when burning the alloy compared to the elemental mixture. The higher predicted temperature in FactSage for low O/F mass ratios is aligned with the inclusion of the heat of mixing, which was previously shown in Figure 3.4.

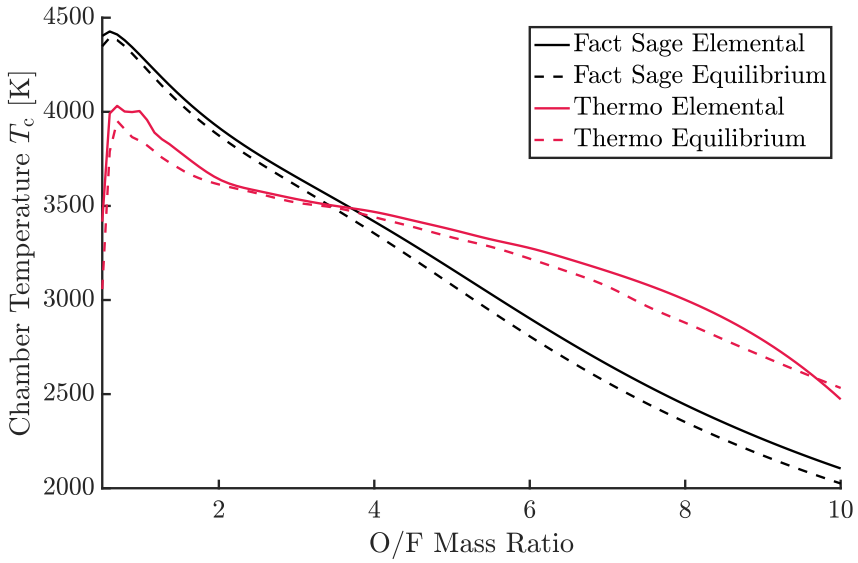

Figure A.1: Thermodynamic calculations for an elemental and an equilibrium composition (A-11 RDF) between FactSage and Thermo.

Figures A.2, A.3, and A.4 show the detailed composition for the three different categories in Figure 4.3. They are based on calculations for A-11 RDF and will differ for other regolith compositions.

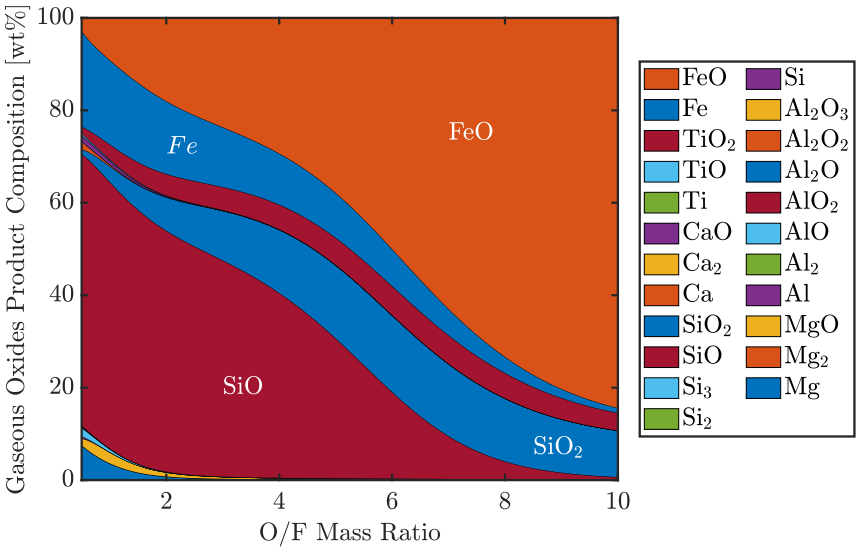

Figure A.2: Detailed gaseous products from Figure 4.3.

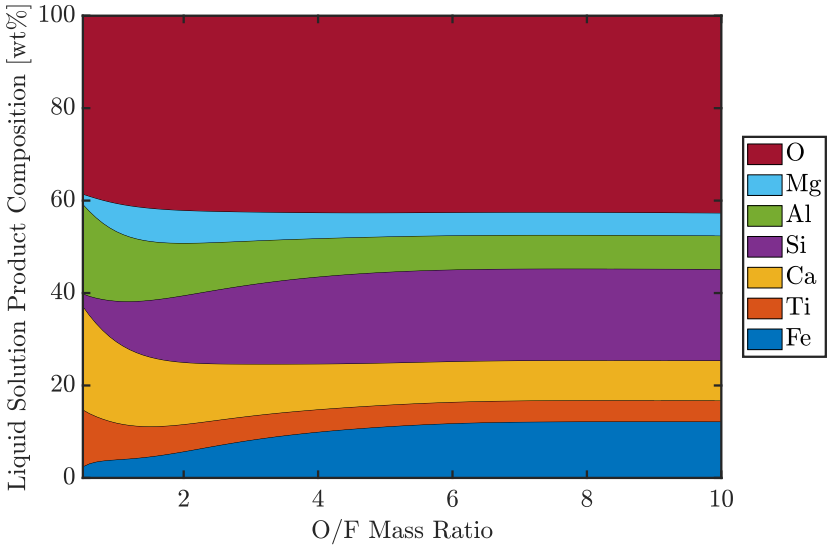

Figure A.3: Detailed condensed products from Figure 4.3 using the FactSage continuum liquid assumption.

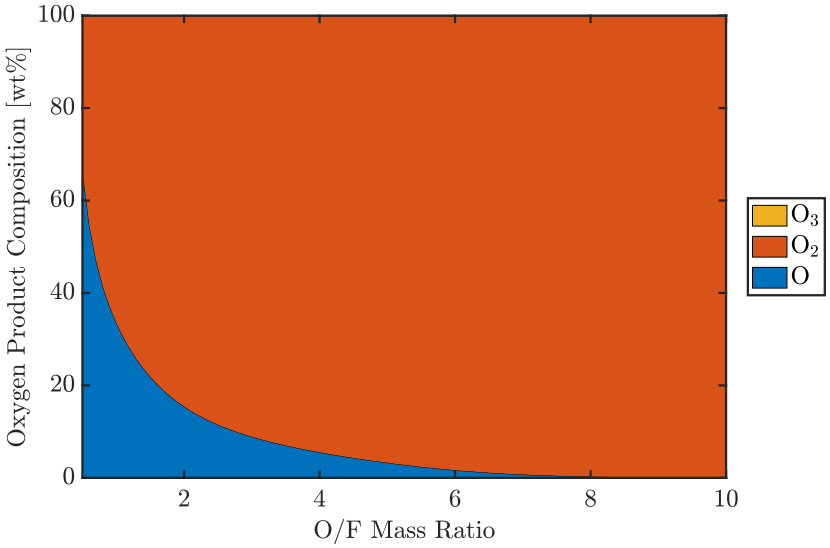

Figure A.4: Detailed oxygen products from Figure 4.3.

Figure A.5 presents the results for the adiabatic flame temperature for varying metal-sulfur mixture ratios in the same way I_{sp} was presented in Figure 4.7. The temperature aligns with the performance calculations, with a higher chamber temperature at higher I_{sp} values, and shows similar iso-temperature lines than iso-I_{sp} lines.

In the same manner as the temperatures throughout the nozzle are shown for A-11 RDF + O_2 in Figure 5.8, the calculations were performed for the hybrid including 30% sulfur and are shown in Figure A.6. As observed for all propellant combinations including sulfur, the temperatures are slightly lower at all cross sections throughout the rocket engine. This indicates that we will have a similar amount of condensed species (Figure 4.4 for A-11 RDF + O_2) for the propellant including sulfur, and the previously presented design considerations are equally valid.

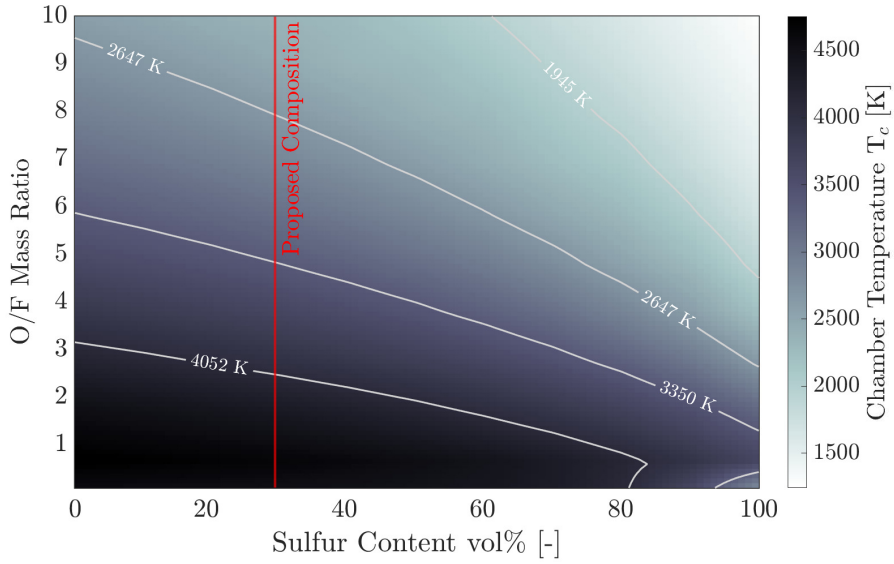

Figure A.5: Influence of the sulfur content on chamber temperature for varying volume ratios of the Al–S mixture over different O/F mass ratios. The parameters for the study are the same as for Figure 4.7.

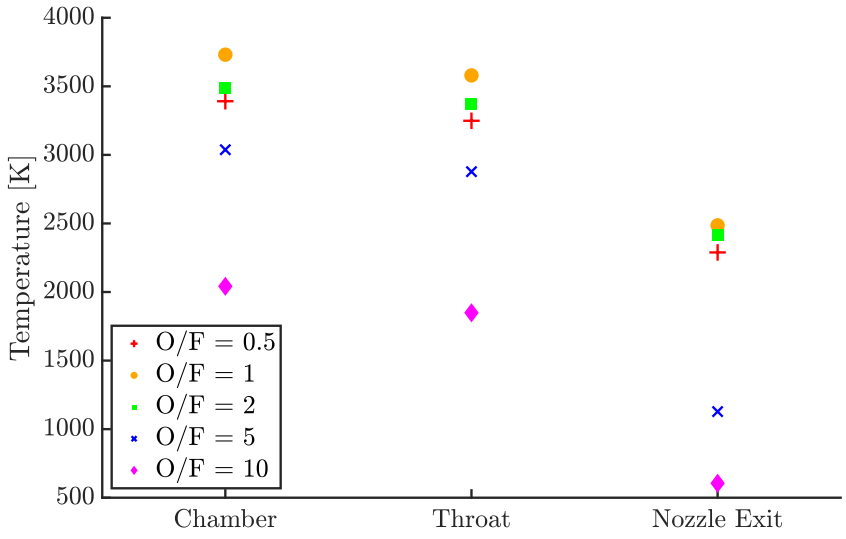

Figure A.6: Temperatures of the flow at different cross sections for the A-11 RDF + S + O_2 thermodynamic calculations

A.2 Supplementary Material for the Aluminum Diffusion Flame Experiments

The main parameters for the diffusion flame experiments are: the dust concentration of the aluminum powder (dependent on the mass flow of the carrier gas), the particle size, the mass flow of the coflow, and the composition of the coflow.

A.2.1 Aluminum powder

The experiments were conducted using micron-sized aluminum powder "Ampal 637" with a Sauter mean diameter (d_{32}) of approximately 6.5 μm. The powder is dried in a vacuum oven to minimize the effects of moisture. A SEM image of the powder is shown in Figure A.7 to illustrate the morphology and size of the particles and the particle size distribution of "Ampal 637" is also plotted.

The total dust concentration of the aluminum powder is dependent on the mass flow rate of the carrier gas (here N_2) and the piston speed. Using calibration experiments, the total mass flow of aluminum dust is determined. In this calibration experiment, the concentration of the particles is monitored by a laser light attenuation probe while a vacuum collects the dust for a fixed period of time. The laser detects and shows a change in voltage when particles are

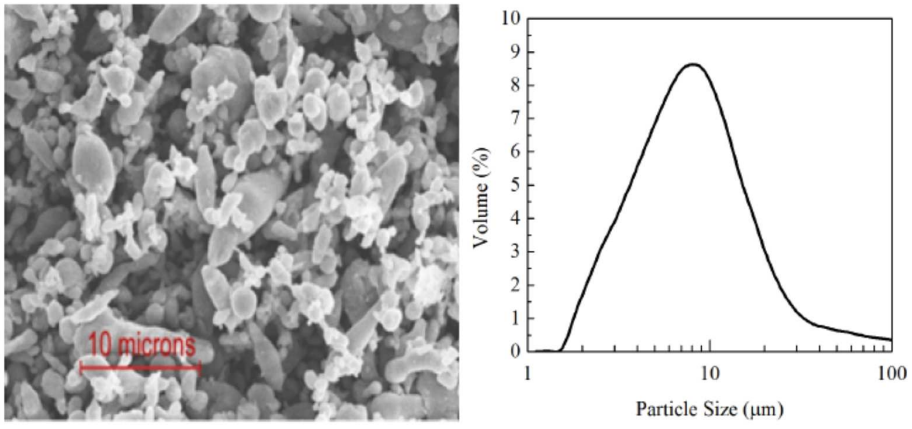

Figure A.7: Scanning electron microscope SEM image (left) and the volumetric particle size distribution (right) of "Ampal-637" aluminum powder [133].

Operational variable	Description	Min. value	Max. value	Unit
$Q_{N_2,carrier}$	Volumetric flow rate of inert carrier gas for dispersion	100	250	cc/s
$Q_{N_2,dilution}$	Volumetric flow rate of inert gas to dilute the pure oxygen	0	80	cc/s
Q_{coflow}	Volumetric flow rate of pure oxygen	200	500	cc/s
v_{piston}	Piston speed for dispersion	0.02	0.1	cm/s

Table A.1: Operational variables and their ranges

passing. The dust concentration in the flow is calculated by dividing the mass of the particles by the total volume of gas. The result of the calibration experiment is a linear relationship between voltage and dust concentration. Using this relationship, the dust concentration of the aluminum particles can be accurately measured during experiments.

A.2.2 Coflow

The coflow can be varied in terms of mass flow rate and composition. Both are controlled using mass flow controllers (MFC). The composition of the coflow consists of a mixture of oxygen and nitrogen allowing for the dilution of pure oxygen.

A.2.3 First experimental campaign

The operational variables with their minimum and maximum values are shown in Table A.1. These were varied in an attempt to achieve a stable Aluminum diffusion flame.

The bounds of the variables in Table A.1 are set by minimal flow rates for aluminum dispersion and operational limits of the MFCs. As previously mentioned, the concentration of aluminum particles depends on a combination of piston speed and the volumetric flow rate of N_2 carrier gas.

Six experimental runs were conducted in this campaign; the parameters v_{piston} and $Q_{N_2,carrier}$

Run No.	Coflow [cc/s]	Dilution [cc/s]	O_2 Percentage	Stability [ms]
1	300	0	100%	20 – 30
2	285	15	95%	20 – 30
3	270	30	90%	15 – 20
4	255	45	85%	15 – 20
5	240	60	80%	10 – 15
6	225	75	75%	< 10

Table A.2: Experimental parameters for the six distinct runs. As these were preliminary experiments, nitrogen and oxygen were approximated to have the same molar mass for simplicity when setting the mass flow rates.

for the aluminum particle dispersion were kept constant throughout, and are 0.076 cm/s and 150 cc/s, respectively. Both flow rates ($Q_{N_2,\text{dilution}}$ and Q_{coflow}) for the coflow were varied to achieve oxygen levels of 75% to 100%. The parameters are summarized below in Table A.2.

As noted in the main body of the thesis, the flames were highly unstable which can be seen in the table and therefore, no further parameters such as flame height were evaluated.

A.2.4 Second experimental campaign

While the design of the improved laminar dust burner is very similar to the previous one, some components have changed such as the stepper motor. Moreover, through the integration of an ejector, the mass flow rate through the dispersion can be varied more precisely and also while operating the experiment.

The experiment that successfully stabilized the diffusion flame was a single run with minimal modifications from previous tests with premixed flames. Consequently, the parameters were not optimized for diffusion flames, and the flow parameters were not recorded, as the primary goal was to demonstrate the feasibility of stabilization. Therefore, the exact parameters for the successful experimental run cannot be provided.

Glossary

AFL Alternative Fuels Laboratory. 73, 81

APS Ascent Propulsion System. 17

CEA Chemical Equilibirum with Applications. xiii, 28–30, 32, 34, 35

DARPA Defense Advanced Research Projects Agency. 5

DSC Differential scanning calorimetry. 68, 69, 72, 73

DTD Deflagration-to-Detonation. 52

DTG Difference thermogravimetry. 69, 71, 72

EDS Energy dispersive X-ray spectroscopy. 73, 78

ISRU In-situ resource utilization. xii, 5–8, 22, 28, 38, 44, 68

JANAF Joint Army-Navy-NASA-Air Force. 28, 29

LH_2 Liquid hydrogen. 6, 7, 10, 13

LLO Low-Lunar Orbit. 17, 66

LOX Liquid oxygen. xiv, 6–8, 10, 13, 29, 36, 51, 52, 54, 57, 58, 60, 65, 66

MFC Mass flow controller. 92

NASA National Aeronautics and Space Administration. xii, 2, 5, 6, 10, 17, 28, 69

O/F Oxidizer-to-fuel. xiv, xvi, xvii, 36, 37, 40, 41, 45–50, 58, 60, 61, 63–66, 87, 90

PRSD Power Reactant Supply and Distribution. 7

RDF Regolith-derived fuel. xiii, xiv, xvi, xvii, 8, 32, 33, 37–45, 49–53, 56, 58–61, 63–66, 68, 69, 79, 87–90

RP-1 Rocket Propellant-1 or Refined Petroleum-1. 52

RTOP Research, Technology, Objectives and Plans. 10

SEM Scanning Electron Microscope. xvi, 73, 78, 91

SHS Self-Propagating High-Temperature Synthesis. 55

STA Simultaneous thermal analyzer. 69, 70

TGA Thermogravimetric analysis. 68–71, 73

TRL Technology Readiness Levels. 13

TWR Thrust-to-weight ratio. 5

Bibliography

[1] NASA. "NASA's plan for sustained lunar exploration and development". https://www.nasa.gov/sites/default/files/atoms/files/a_sustained_lunar_presence_nspc_report4220final.pdf. (2020), accessed 03/20/2024.

[2] NASA. "NASA's lunar exploration program overview". https://www.nasa.gov/sites/default/files/atoms/files/artemis_plan-20200921.pdf. (2020), accessed 03/20/2024.

[3] R. Brukardt, J. Klempner, D. Pacthod, and B. Stokes. "The role of space in driving sustainability, security, and development on Earth". In: *McKinsey & Company Aerospace and Defence* (2022). URL: https://www.mckinsey.com/industries/aerospace-and-defense/our-insights/the-role-of-space-in-driving-sustainability-security-and-development-on-earth.

[4] M. W. Pontin. "Mining the Moon". In: *MIT Technology Review* (2007). URL: https://www.technologyreview.com/2007/08/23/223985/mining-the-moon/.

[5] E. Slyuta, A. Abdrakhimov, and E. Galimov. "The estimation of Helium-3 probable reserves in lunar regolith". In: *Lunar and Planetary Science* 38 (2007), p. 2175.

[6] S. Yarlagadda. "Economics of the stars: the future of asteroid mining and the global economy". In: *Harvard International Review* (2022). URL: https://hir.harvard.edu/economics-of-the-stars/.

[7] E. LaForge, W. Price, and J. Rafelski. "Superheavy elements and ultradense matter". In: *The European Physical Journal Plus* 138 (2023), p. 812. DOI: 10.1140/epjp/s13360-023-04454-8.

[8] R. Sohn. "Metal asteroid Psyche has a ridiculously high 'value.' But what does that even mean?" In: *Space.com* (2023). URL: https://www.space.com/psyche-metal-asteroid-composition#:~:text=Scientists%20think%20the%20asteroid%20could,scientist%2C%20Lindy%20Elkins%2DTanton..

[9] Airbus Space and Defence. *In space manufacturing and assembly*. https://www.airbus.com/en/newsroom/news/2022-05-in-space-manufacturing-and-assembly. (2022), accessed 11/01/2023.

[10] D. M. Goebel, I. Katz, and I. G. Mikellides. *Fundamentals of Electric Propulsion*. 2nd ed. Hoboken, NJ: Wiley, 2024. ISBN: 9780470436448. DOI: https://doi.org/10.1002/9780470436448.ch1.

[11] NASA. *Saturn V News Reference: F-1 Engine Fact Sheet*. https://web.archive.org/web/20051221114403/http://history.msfc.nasa.gov/saturn_apollo/documents/F-1_Engine.pdf. (1968), accessed 03/20/2024.

[12] M. Martinez-Sanchez and P. C. Lozano. *16.522 Space Propulsion. Massachusetts Institute of Technology Open Courseware*. Online course materials provided by MIT. Spring 2015. URL: https://ocw.mit.edu/courses/aeronautics-and-astronautics/16-522-space-propulsion-spring-2015/.

[13] S. Hall, B. Jorns, S. Cusson, A. Gallimore, H. Kamhawi, P. Peterson, T. Haag, J. Mackey, M. Baird, and J. Gilland. "Performance and High-Speed Characterization of a 100-kW Nested Hall Thruster". In: *Journal of Propulsion and Power* 38 (2021), pp. 1–11. DOI: 10.2514/1.B38080.

[14] DARPA. *DARPA, NASA Collaborate on Nuclear Thermal Rocket Engine*. https://www.darpa.mil/news-events/2023-01-24. (2023), accessed on 03/20/2024.

[15] G. F. Sowers. "A cislunar transportation system fuelled by lunar resources". In: *Space Policy* 37 (2016), pp. 103–109. DOI: 10.1016/j.spacepol.2016.07.004.

[16] K. R. Araghi. *NASA Lunar In-Situ Resource Utilization Technology Overview*. Presentation to Korean Institute of Geoscience and Mineral Resources (KIGAM) ISRU Workshop.

2022. URL: https://ntrs.nasa.gov/api/citations/20220006072/downloads/LIVE-ISRU%20-Overview-RevB.pdf.

[17] A. Hepp, D. Linne, G. Landis, M. Groth, and J. Colvin. "Production and Use of Metals and Oxygen for Lunar Propulsion". In: *Journal of Propulsion and Power* 10.6 (1991), pp. 834–840. DOI: 10.2514/3.51397.

[18] P. O. Hayne, A. Hendrix, E. Sefton-Nash, M. A. Siegler, P. G. Lucey, K. D. Retherford, J.-P. Williams, B. T. Greenhagen, and D. A. Paige. "Evidence for exposed water ice in the Moon's south polar regions from Lunar Reconnaissance Orbiter ultraviolet albedo and temperature measurements". In: *Icarus* 255 (2015), pp. 58–69. ISSN: 0019-1035. DOI: https://doi.org/10.1016/j.icarus.2015.03.032.

[19] D. J. Lawrence, P. N. Peplowski, J. T. Wilson, and R. C. Elphic. "Global Hydrogen Abundances on the Lunar Surface". In: *Journal of Geophysical Research: Planets* 127.7 (2022), e2022JE007197. DOI: https://doi.org/10.1029/2022JE007197.

[20] E. D. Mendez-Ramos. "Enabling Conceptual Design and Analysis of Cryogenic In-Space Vehicles through the Development of an Extensible Boil-Off Model". PhD thesis. Atlanta, GA: Georgia Institute of Technology, 2021.

[21] K. Kinefuchi, T. Miyakita, Y. Umemura, J. Nakajima, and M. Koga. "Cooling system optimization of cryogenic propellant storage on lunar surface". In: *Cryogenics* 124 (2022), p. 103494. DOI: https://doi.org/10.1016/j.cryogenics.2022.103494.

[22] Q. Cheng, R. Zhang, Z. Shi, and J. Lin. "Review of common hydrogen storage tanks and current manufacturing methods for aluminium alloy tank liners". In: *International Journal of Lightweight Materials and Manufacture* 7.2 (2024), pp. 269–284. DOI: https://doi.org/10.1016/j.ijlmm.2023.08.002.

[23] S. S. Schreiner, J. A. Dominguez, L. Sibille, and J. A. Hoffman. "Thermophysical property models for lunar regolith". In: *Advances in Space Research* 57.5 (2016), pp. 1209–1222. DOI: 10.1016/j.asr.2015.12.035.

[24] M. L. Meyer. "Powdered aluminum and oxygen rocket propellants: Subscale combustion experiments". In: *Proc. of the 30th JANNAF Combustion Subcommittee Meeting, Monterey, CA* (1993). NASA Technical Memorandum 106439.

[25] V. Malinin, E. Kolomin, and I. Antipin. "Ignition and Combustion of Aluminum–Air Suspensions in a Reactor for High-Temperature Synthesis of Alumina Powder". In: *Combustion Explosion and Shock Waves* 38 (2002), pp. 525–534. DOI: 10.1023/A:1020330316134.

[26] D. Vaniman, D. Pettit, and G. Heiken. "Uses of lunar sulfur". In: *Proc. of the Second Conference on Lunar Bases and Space Activities of the 21st Century* (1992). , NASA Report N93-13981.

[27] A. Mardon. "Lunar Prospector: A Preliminary Surface Remote Sensing Resource Assessment for the Moon". In: *New Technologies for Lunar Resource Assessment*. Ed. by R. C. Elphic and D. S. McKay. 1992, p. 35.

[28] S. Nozette, C. L. Lichtenberg, P. Spudis, R. Bonner, W. Ort, E. Malaret, M. Robinson, and E. M. Shoemaker. "The Clementine Bistatic Radar Experiment". In: *Science* 274.5292 (1996), pp. 1495–1498. DOI: 10.1126/science.274.5292.1495.

[29] D. L. Linne and M. L. Meyer. "A compilation of lunar and Mars exploration strategies utilizing indigenous propellants". In: *NTRS* (1992). NASA Technical Memorandum 105262.

[30] E. Y. Shafirovich, A. A. Shiryaev, and U. I. Goldshleger. "Magnesium and carbon dioxide: A rocket propellant for Mars missions". In: *Journal of Propulsion and Power* 9.2 (1993), pp. 197–203. DOI: 10.2514/3.23609.

[31] E. Shafirovich and A. Varma. "Metal-CO_2 Propulsion for Mars Missions: Current Status and Opportunities". In: *Journal of Propulsion and Power* 24.3 (2008), pp. 385–394. DOI: 10.2514/1.32635.

[32] E. Shafirovich. "Lithium and Magnesium Fuels for Space Propulsion and Power". In: *Nano and Micro-Scale Energetic Materials*. Ed. by W. Pang and L. T. DeLuca. Weinheim,

Germany: Wiley, 2023. Chap. 14, pp. 397–416. ISBN: 9783527835348. DOI: 10.1002/9783527835348.ch14.

[33] S. Goroshin, A. Higgins, and J. Lee. "Powdered magnesium-carbon dioxide propulsion concepts for Mars missions". In: *Proc. of the 35th Joint Propulsion Conference and Exhibit, Los Angeles, CA* (1999). AIAA-1999-2408. DOI: 10.2514/6.1999-2408.

[34] G. Sanders and J. Kleinherz. *In situ resource utilization (ISRU) envisioned future priorities*. https://ntrs.nasa.gov/citations/20220004617. (2020), accessed 04/01/2023.

[35] M. A. Gibson, C. W. Knudsen, D. J. Brueneman, C. C. Allen, H. Kanamori, and D. S. McKay. "Reduction of lunar basalt 70035: Oxygen yield and reaction product analysis". In: *Journal of Geophysical Research: Planets* 99.E5 (1994), pp. 10887–10897. DOI: https://doi.org/10.1029/94JE00787.

[36] S. D. Rosenberg, R. L. Beegle, G. A. Guter, F. E. Miller, and M. Rothenberg. "The onsite manufacture of propellant oxygen from lunar resources". In: *Space Resources. Volume 3: Materials*. Houston, TX: NASA Johnson Space Center, 1992, pp. 162–184.

[37] D. Kesterke. *Electrowinning of Oxygen from Silicate Rocks*. Vol. 7587. U.S. Department of Interior, Bureau of Mines, 1971.

[38] L. Sibille, D. Sadoway, A. Sirk, P. Tripathy, O. Melendez, E. Standish, J. Dominguez, D. Stefanescu, P. Curreri, and S. Poizeau. "Recent Advances in Scale-Up Development of Molten Regolith Electrolysis for Oxygen Production in Support of a Lunar Base". In: *Proc. of the 47th AIAA Aerospace Sciences Meeting including The New Horizons Forum and Aerospace Exposition* (2009). AIAA-2009-659. DOI: 10.2514/6.2009-659.

[39] B. A. Lomax, M. Conti, N. Khan, N. S. Bennett, A. Y. Ganin, and M. D. Symes. "Proving the viability of an electrochemical process for the simultaneous extraction of oxygen and production of metal alloys from lunar regolith". In: *Planetary and Space Science* 180 (2020), p. 104748. ISSN: 0032-0633. DOI: https://doi.org/10.1016/j.pss.2019.104748.

[40] A. Meurisse, B. Lomax, Á. Selmeci, M. Conti, R. Lindner, A. Makaya, M. D. Symes, and J. Carpenter. "Lower temperature electrochemical reduction of lunar regolith

simulants in molten salts". In: *Planetary and Space Science* 211 (2022), p. 105408. DOI: https://doi.org/10.1016/j.pss.2021.105408.

[41] B. A. Lomax, G. H. Just, P. J. McHugh, P. K. Broadley, G. C. Hutchings, P. A. Burke, M. J. Roy, K. L. Smith, and M. D. Symes. "Predicting the efficiency of oxygen-evolving electrolysis on the Moon and Mars". In: *Nature Communications* 13.583 (2022). DOI: https://doi.org/10.1038/s41467-022-28147-5.

[42] E. Y. Shafirovich and U. Goldshleger. "Mars Multi-Sample Return Mission". In: *Journal of the British Interplanetary Society* 48 (1995), pp. 315–319.

[43] E. Shafirovich and U. Goldshleger. "Comparison of Potential Fuels for Martian Rockets Using CO2". In: *Journal of Propulsion and Power* 13.3 (1997), pp. 395–397.

[44] S. Yuasa and H. Isoda. "Carbon Dioxide Breathing Propulsion for a Mars Airplane". In: *25th Joint Propulsion Conference* (1989). AIAA-89-2863.

[45] D. Todd. *SpaceX's Mars rocket to be methane-fuelled*. https://www.flightglobal.com/spacexs-mars-rocket-to-be-methane-fuelled/107953.article. (2012), accessed on 04/06/2024.

[46] Y. L. Yung and P. Chen. "Methane on Mars". In: *Journal of Astrobiology & Outreach* 3.1 (2015), p. 1000125.

[47] L. Han, S. Song, M. Liu, S. Yao, Z. Liang, H. Cheng, Z. Ren, W. Liu, R. Lin, G. Qi, X. Liu, Q. Wu, J. Luo, and H. L. Xin. "Stable and Efficient Single-Atom Zn Catalyst for CO_2 Reduction to CH_4". In: *Journal of the American Chemical Society* 142.29 (2020), pp. 12563–12567. DOI: 10.1021/jacs.9b12111.

[48] Y. L. Yung, P. Chen, K. Nealson, S. Atreya, P. Beckett, J. G. Blank, B. Ehlmann, J. Eiler, G. Etiope, J. G. Ferry, F. Forget, P. Gao, R. Hu, A. Kleinböhl, R. Klusman, F. Lefèvre, C. Miller, M. Mischna, M. Mumma, S. Newman, D. Oehler, M. Okumura, R. Oremland, V. Orphan, R. Popa, M. Russell, L. Shen, B. Sherwood Lollar, R. Staehle, V. Stamenković, D. Stolper, A. Templeton, A. C. Vandaele, S. Viscardy, C. R. Webster, P. O. Wennberg, M. L. Wong, and J. Worden. "Methane on Mars and Habitability: Challenges and Responses". In: *Astrobiology* 18.10 (2018), pp. 1221–1242. DOI: 10.1089/ast.2018.1917.

[49] B. Palaszewski. "Atmospheric Mining in the Outer Solar System: Resource Capturing, Exploration, and Exploitation". In: *49th AIAA/ASME/SAE/ASEE Joint Propulsion Conference, San Jose, CA* (2013). AIAA–2013–3765. DOI: 10.2514/6.2013-3765.

[50] B. Palaszewski and J. Zakany. "Metallized gelled propellants: Oxygen/RP-1/aluminum rocket combustion experiments". In: *Proceedings of the 31st Joint Propulsion Conference and Exhibit, San Diego, CA* (1995). NASA Technical Memorandum 107025. DOI: 10.2514/6.1995-2435.

[51] R. Ash, V. Cuda, M. Stancati, and J. Niehoff. "Outer planet satellite return missions using in situ propellant production". In: *Acta Astronautica* 8.5 (1981), pp. 511–526. DOI: https://doi.org/10.1016/0094-5765(81)90103-X.

[52] M. Tajmar, A. Genovese, and W. Steiger. "Indium Field Emission Electric Propulsion Microthruster Experimental Characterization". In: *Journal of Propulsion and Power* 20.2 (2004), pp. 211–218. DOI: 10.2514/1.9247.

[53] K. Katsonis. "Support of Solar system study by using ISRU based electric propulsion". In: *Aeron Aero Open Access Journal* 6 (2022), p. 97. DOI: 10.15406/aaoaj.2022.06.00146.

[54] NASA. *Apollo lunar module documentation*. https://www.hq.nasa.gov/alsj/alsj-LMdocs.html. (1969), accessed 04/06/2024.

[55] NASA. "Apollo lunar surface journal". https://www.hq.nasa.gov/alsj/a17/A17_LunarRover2.pdf. (1972), accessed 04/06/2024.

[56] NASA. *Surveyor 6 - spacecraft - the NSSDCA*. https://nssdc.gsfc.nasa.gov/nmc/spacecraft/display.action?id=1967-112A. (1967), accessed 04/06/2024.

[57] R. L. Degner, M. H. Kaplan, J. Manning, R. Meetin, S. Pasternack, S. Peterson, and H. Seifert. *The Lunar Hopping Transporter Final Report*. Tech. rep. Stanford University, 1971. URL: https://ntrs.nasa.gov/api/citations/19730007490/downloads/19730007490.pdf.

[58] J. Wickman and A. Oberth. "Lunar base spacecraft propulsion with lunar propellants". In: *Proc. of the 22nd Joint Propulsion Conference, Huntsville, AL* (1986). AIAA-1986-1763. DOI: 10.2514/6.1986-1763.

[59] R. Teeter, T. Crabb, and L. Johnson. *Lunar Surface Base Propulsion System Study*. Tech. rep. Astronautics Corporation of America, 1987. URL: https://ntrs.nasa.gov/api/citations/19890010900/downloads/19890010900.pdf.

[60] R. M. Zubrin. "Indigenous Martian propellant". In: *Aerospace America* 27 (1989), pp. 48–51.

[61] B. Cohanim, T. Mosher, M. Joyce, J. Hoffman, N. Harrison, J. Herron, K. Davis, P. Cunio, and J. Luis. "Small Lunar Exploration and Delivery System Concept". In: *Proc. of the AIAA SPACE 2009 Conference Exposition, Pasadena, CA* (2009). DOI: 10.2514/6.2009-6712.

[62] M. Phillip, A. Babuscia, Z. Bailey, H. Chaurasia, R. Goel, A. Golkar, D. Selva, E. Timmons, B. Cohanim, J. Hoffman, and D. Miller. "Initial Development of an Earth-Based Prototype for a Lunar Hopper Autonomous Exploration System". In: *Proc. of AIAA SPACE 2009 Conference Exposition, Pasadena, CA* (2009). AIAA-2009-6713. DOI: 10.2514/6.2009-6713.

[63] O. Jia-Richards, S. K. Hampl, and P. C. Lozano. "Electrostatic Levitation on Atmosphere-Less Planetary Bodies with Ionic-Liquid Ion Sources". In: *Journal of Spacecraft and Rockets* 58.6 (2021), pp. 1694–1703. DOI: 10.2514/1.A35001.

[64] S. Goroshin, I. Fomenko, and J. Lee. "Burning velocities in fuel-rich aluminum dust clouds". In: *Proc. of the International Symposium on Combustion* 26.2 (1996), pp. 1961–1967. DOI: https://doi.org/10.1016/S0082-0784(96)80019-1.

[65] M. Soo, S. Goroshin, N. Glumac, K. Kumashiro, J. Vickery, D. L. Frost, and J. M. Bergthorson. "Emission and laser absorption spectroscopy of flat flames in aluminum suspensions". In: *Combustion and Flame* 180 (2017), pp. 230–238. DOI: 10.1016/j.combustflame.2017.03.006.

[66] J. Bergthorson, S. Goroshin, M. Soo, P. Julien, J. Palecka, D. Frost, and D. Jarvis. "Direct combustion of recyclable metal fuels for zero-carbon heat and power". In: *Applied Energy* 160 (2015), pp. 368–382. ISSN: 0306-2619. DOI: 10.1016/j.apenergy.2015.09.037.

[67] E. Shafirovich, S. K. Teoh, and A. Varma. "Combustion of levitated titanium particles in air". In: *Combustion and Flame* 152.1 (2008), pp. 262–271. DOI: 10.1016/j.combustflame.2007.05.008.

[68] H. Cassel. *Some fundamental aspects of dust flames*. Tech. rep. U.S. Deptartment of the Interior, Bureau of Mines, 1964.

[69] S. Goroshin, J. Palecka, and J. M. Bergthorson. "Some fundamental aspects of laminar flames in nonvolatile solid fuel suspensions". In: *Progress in Energy and Combustion Science* 91 (July 2022), p. 100994. DOI: 10.1016/j.pecs.2022.100994.

[70] P. Julien, J. Vickery, S. Goroshin, D. Frost, and J. Bergthorson. "Freely-propagating flames in aluminum dust clouds". In: *Combustion and Flame* 16 (2015), pp. 1–13. DOI: 10.1016/j.combustflame.2015.07.046.

[71] A. Ghosh, N. M. Munoz-Munoz, K. P. Chatelain, and D. A. Lacoste. "Laminar burning velocity of hydrogen, methane, ethane, ethylene, and propane flames at near-cryogenic temperatures". In: *Applications in Energy and Combustion Science* 12 (2022), p. 100094. DOI: https://doi.org/10.1016/j.jaecs.2022.100094.

[72] S. Goroshin, M. Kolbe, and J. Lee. "Flame speed in a binary suspension of solid fuel particles". In: *Proceedings of the Combustion Institute* 28 (2000), pp. 2811–2817. DOI: 10.1016/S0082-0784(00)80703-1.

[73] I. Glassman, R. Yetter, and N. G. Glumac. *Combustion*. 5th ed. Waltham, MA: Elsevier, 2015. ISBN: 9780120885732.

[74] J. Vovchuk and N. Poletaev. "The temperature field of a laminar diffusion dust flame". In: *Combustion and Flame* 99.3 (1994). 25th Symposium (International) on Combustion Papers, pp. 706–712. ISSN: 0010-2180. DOI: 10.1016/0010-2180(94)90065-5.

[75] N. Poletaev and J. Vovchuk. "Particularities of the laminar diffusion dust flames". In: *International Conference on Combustion and Detonation, Moscow, Russia* (2004).

[76] N. Poletaev and M. Khlebnikova. "Combustion of Iron Particles Suspension in Laminar Premixed and Diffusion Flames". In: *Combustion Science and Technology* 194.7 (2022), pp. 1356–1377. DOI: 10.1080/00102202.2020.1812588.

[77] N. Ageev, Y. Vovchuk, S. Goroshin, A. N. Zolotko, and N. I. Poletaev. "Steady combustion of solid fuel gas-suspensions. Laminar diffusion two-phase flame." In: *Combustion, Explosion, and Shock Waves* 26 (1990), pp. 669–677. DOI: https://doi.org/10.1007/BF00786504.

[78] D. Stoeser, D. Rickman, and S. Wilson. "Design and Specifications for the Highland Regolith Prototype Simulants NU-LHT-1M and -2M". In: *NASA Technical Memorandum 2010–216438* (2010).

[79] D. S. McKay, G. Heiken, A. Basu, G. Blanford, S. Simon, R. Reedy, B. M. French, and J. Papike. "The lunar regolith". In: *Lunar Sourcebook*. Ed. by G. H. Heiken, D. T. Vaniman, and B. M. French. New York, NY: Cambridge University Press, 1991. Chap. 7, pp. 285–356. ISBN: 0521334446.

[80] M. L. Meyer. "Design Issues for Lunar In Situ Aluminum/Oxygen Propellant Rocket Engines". In: *Proc. of the 1992 Aerospace Design Conference, Irvine, CA* (1992). NASA Technical Memorandum 105433.

[81] U. Yelken, A. Yalcintas, O. Kara, M. Baysal, and M. A. Karabeyoglu. "Experimental study of lunar-based hybrid rocket engine". In: *Proc. of the AIAA Propulsion and Energy 2021 Forum* (2021). AIAA-2021-3507. DOI: 10.2514/6.2021-3507.

[82] C. Bale, E. Bélisle, P. Chartrand, S. Decterov, G. Eriksson, A. Gheribi, K. Hack, I.-H. Jung, Y.-B. Kang, J. Melançon, A. Pelton, S. Petersen, C. Robelin, J. Sangster, P. Spencer, and M.-A. Van Ende. "FactSage thermochemical software and databases, 2010–2016". In: *Calphad* 54 (2016), pp. 35–53. DOI: https://doi.org/10.1016/j.calphad.2016.05.002.

[83] S. Gordon and B. J. McBride. "Computer Program for Calculation of Complex Chemical Equilibrium Compositions and Applications". In: *NASA Reference Publication 1311* (1994).

[84] M. W. Chase Jr. "NIST-JANAF Thermochemical Tables, 4th Edition". In: *Journal of Physical and Chemical Reference Data, Monograph* 9 (1998), pp. 1–1951.

[85] A. A. Shiryaev. "Thermodynamics of SHS Processes: Advanced Approach". In: *International Journal of Self-Propagating High-Temperature Synthesis* 4.4 (1995), pp. 351–362.

[86] L. Gurvich, I. Veyts, and C. Alcock. *Thermodynamic Properties of Individual Substances*. 4th ed. Only Vols. 1 and 2 were published in English, Vols. 3 and 4 are only available in the Russian original. New York: Hemisphere, 1989.

[87] L. V. Gurvich. "Reference Books and Data Banks on the Thermodynamic Properties of Inorganic Substances". In: *Materials Chemistry at High Temperatures: Characterization*. Ed. by J. W. Hastie. Totowa, NJ: Humana Press, 1990, pp. 197–206. ISBN: 978-1-4612-0481-7.

[88] *FSstel - FactSage Steel Alloy Database*. fromhttps://www.crct.polymtl.ca/fact/documentation/menu.php?FSstel=1. accessed 03/20/2024.

[89] M. Notin, J. Gachon, and J. Hertz. "Enthalpy of Formation of Al_4Ca and Al_2Ca and of the liquid alloys (aluminum + calcium)". In: *Journal of Chemical Thermodynamics* 14 (1982), pp. 425–434.

[90] J. Acker, K. Bohmhammel, G. van den Berg, J. van Miltenburg, and C. Kloc. "Thermodynamic properties of iron silicides FeSi and α-$FeSi_2$". In: *The Journal of Chemical Thermodynamics* 31.12 (1999), pp. 1523–1536. DOI: https://doi.org/10.1006/jcht.1999.0550.

[91] D. Allen, H. Krier, and N. Glumac. "Heat transfer effects in nano-aluminum combustion at high temperatures". In: *Combustion and Flame* 161.1 (2014), pp. 295–302. DOI: https://doi.org/10.1016/j.combustflame.2013.07.010.

[92] D. Ning, Y. Shoshin, J. van Oijen, G. Finotello, and L. de Goey. "Burn time and combustion regime of laser-ignited single iron particle". In: *Combustion and Flame* 230 (2021), p. 111424. DOI: https://doi.org/10.1016/j.combustflame.2021.111424.

[93] Y. Zhou, J. Liu, D. Liang, W. Shi, W. Yang, and J. Zhou. "Effect of particle size and oxygen content on ignition and combustion of aluminum particles". In: *Chinese Journal of Aeronautics* 30.6 (2017), pp. 1835–1843. DOI: https://doi.org/10.1016/j.cja.2017.09.006.

[94] A. Fujinawa, L. C. Thijs, J. Jean-Philyppe, A. Panahi, D. Chang, M. Schiemann, Y. A. Levendis, J. M. Bergthorson, and X. Mi. "Combustion behavior of single iron particles, Part II: A theoretical analysis based on a zero-dimensional model". In: *Applications in Energy and Combustion Science* 14 (2023), p. 100145. ISSN: 2666-352X. DOI: https://doi.org/10.1016/j.jaecs.2023.100145.

[95] D. Chang, L. C. Thijs, A. Panahi, X. Mi, J. M. Bergthorson, and Y. A. Levendis. "Effects of oxygen concentration on nanoparticle formation during combustion of iron powders". Unpublished manuscript.

[96] M. Beckstead. "Correlating Aluminum Burning Times". In: *Combustion, Explosion, and Shock Waves* 41.5 (2005), pp. 533–546. DOI: 10.1007/s10573-005-0067-2.

[97] E. K. Gibson Jr. and G. W. Moore. "Sulfur abundances and distributions in the valley of Taurus-Littrow". In: *Lunar Science Conference, 5th, Houston, Texas* (1974).

[98] J. Gillis-Davis. *Chandrayaan-3's measurements of sulfur open the doors for lunar science and exploration*. fromhttps://www.space.com/chandrayaan-3-sulfur-measurements-lunar-science-expert-voices. (2023), accessed 03/20/2024.

[99] E. K. Gibson Jr. "Thermal analysis-mass spectrometer computer system and its application to the evolved gas analysis of Green River shale and lunar soil samples". In: *Thermochimical Acta* 5.3 (1973), pp. 243–255.

[100] D. S. Bruce. "Explosive property of aluminum powder liquid oxygen mixture". Master's Thesis. Stockton, CA: University of the Pacific, 1936.

[101] C. M. Austin, C. S. Rohrer, and R. L. Seifert. "Explosive hazard of aluminum-liquid oxygen mixtures". In: *Journal of Chemical Education* 36.2 (1959), p. 54. DOI: 10.1021/ed036p54.

[102] W. Wong, J. Starkovich, S. Adams, B. Palaszewski, W. Davison, W. Burt, H. Thridandam, H. Hu-Peng, and M. Santy. "Cryogenic gellant and fuel formulation for metallized gelled propellants: Hydrocarbons and hydrogen with aluminum". In: *Proc. of the 30th Joint Propulsion Conference and Exhibit, Indianapolis, IN* (1994). NASA Technical Memorandum 106698.

[103] J. Hodge and L. Rauen. "Space nuclear tug mission applications". In: *AIP Conference Proceedings* 361.1 (1996), pp. 1065–1070.

[104] J. Brewer, R. Chaves, R. Tomiozzo, and M. Okutsu. "Model Rocket Projects for Aerospace Engineering Course: Propellant Analyses". In: *Proc. of the 54th AIAA Aerospace Sciences Meeting, San Diego, CA* (2016). AIAA-2016-1578. DOI: 10.2514/6.2016-1578.

[105] S. Goroshin, J. Lee, and D. Frost. "Combustion synthesis of ZnS in microgravity". In: *Symposium (International) on Combustion* 25.1 (1994), pp. 1651–1657. DOI: https://doi.org/10.1016/S0082-0784(06)80812-X.

[106] S. Goroshin, A. Miera, D. Frost, and J. Lee. "Metal-sulfur combustion". In: *Symposium (International) on Combustion* 26.2 (1996), pp. 1883–1889.

[107] S. Goroshin, L. Camargo, and J. Lee. "Liquid flame: combustion of metal suspensions in liquid sulfur". In: *Proceedings of the Combustion Institute* 30.2 (2005), pp. 2561–2568.

[108] A. Nabavi, S. Goroshin, D. Frost, and F. Barthelat. "Mechanical properties of chromium–chromium sulfide cermets fabricated by self-propagating high-temperature synthesis". In: *Journal of Materials Science* 50 (Feb. 2015). DOI: 10.1007/s10853-015-8902-7.

[109] C. Glaser, J. Hijlkema, and J. Anthoine. "Bridging the Technology Gap: Strategies for Hybrid Rocket Engines". In: *Aerospace* 10.10 (2023). DOI: 10.3390/aerospace10100901.

[110] T. Miller and J. Herr. "Green Rocket Propulsion by Reaction of Al and Mg Powders and Water". In: *Proc. of the 40th AIAA/ASME/SAE/ASEE Joint Propulsion Conference and Exhibit, Fort Lauderdale, FL* (2004). AIAA-2004-4037. DOI: 10.2514/6.2004-4037.

[111] J. Foote and R. Litchford. "Powdered Magnesium: Carbon Dioxide Combustion for Mars Propulsion". In: *Proc. of the 41st AIAA/ASME/SAE/ASEE Joint Propulsion Conference and Exhibit, Tuscon, AZ* (2005). AIAA-2005-4469. DOI: 10.2514/6.2005-4469.

[112] Y. Li, C. Hu, X. Zhu, J. Hu, X. Hu, C. Li, and Y. Cai. "Experimental study on combustion characteristics of powder magnesium and carbon dioxide in rocket engine". In: *Acta Astronautica* 155 (Feb. 2019), pp. 334–349. DOI: https://doi.org/10.1016/j.actaastro.2018.11.006.

[113] J. Hu, C. Hu, Y. Che, X. Zhu, J. Yang, M. Li, and C. Li. "Experimental study on the working performance of powdered magnesium and liquid carbon dioxide bipropellant rocket engine for Mars missions". In: *Acta Astronautica* 184 (2021), pp. 274–285. DOI: https://doi.org/10.1016/j.actaastro.2021.04.025.

[114] C. Li, C. Hu, X. Xin, Y. Li, and H. Sun. "Experimental study on the operation characteristics of aluminum powder fueled ramjet". In: *Acta Astronautica* 129 (Dec. 2016), pp. 74–81. DOI: https://doi.org/10.1016/j.actaastro.2016.08.032.

[115] S. Luo, Y. Feng, J. Song, D. Xu, and K. Xia. "Progress and challenges in exploration of powder fueled ramjets". In: *Applied Thermal Engineering* 213 (2022), p. 118776. DOI: 10.1016/j.applthermaleng.2022.118776.

[116] S. Goroshin, A. Higgins, and M. Kamel. "Powdered metals as fuel for hypersonic ramjets". In: *Proc. of the 37th Joint Propulsion Conference and Exhibit, Salt Lake City, UT* (2001). AIAA-2001-3919. DOI: 10.2514/6.2001-3919.

[117] H.-D. Kwak, S. Kwon, and C.-H. Choi. "Performance assessment of electrically driven pump-fed LOX/kerosene cycle rocket engine: Comparison with gas generator cycle". In: *Aerospace Science and Technology* 77 (2018), pp. 67–82. DOI: 10.1016/j.ast.2018.02.033.

[118] G. Sutton and O. Biblarz. *Rocket Propulsion Elements*. 5th ed. Hoboken, NJ: Wiley, 2010. ISBN: 9780470080245.

[119] E. Armstrong. "Liquid oxygen cooling of hydrocarbon fueled rocket thrust chambers". In: *Proc. of the 25th Joint Propulsion Conference, Monterey, CA* (1986). NASA Technical Memorandum 102113. DOI: 10.2514/6.1989-2739.

[120] R. Katkov, I. Lozino-Lozinskaya, S. Mosolov, V. Skoromnov, A. Smolentsev, B. Sokolov, P. Strizhenko, and N. Tupitsyn. "Experimental Development of a Multifunctional Liquid Rocket Engine with Oxygen-Cooled Combustion Chamber: Results of 2009–2014". In: *Space Engineering and Technology* 4.11 (2015), pp. 12–24.

[121] P. Hanaphy, K. Sertoglu, A. Shaikhnag, H. Everett, M. Petch, and B. Jackson. *Launcher succesfully test-fires EOS 3D printed copper rocket engine*. https://3dprintingindustry.

com/news/launcher-succesfully-test-fires-eos-3d-printed-copper-rocket-engine-140809/. (2018), accessed 04/01/2023.

[122] E. S. Armstrong and J. A. Schlumberger. "Cooling of Rocket Thrust Chambers With Liquid Oxygen". In: *Proc. of the 26th Joint Propulsion Conference, Orlando, FL* (1990). NASA Technical Memorandum 103146.

[123] M. De Morton. "Erosion in rocket motor nozzles". In: *Wear* 41.2 (1977), pp. 223–231. DOI: 10.1016/0043-1648(77)90003-5.

[124] R. F. Hoglund. "Recent Advances in Gas-Particle Nozzle Flows". In: *ARS Journal* 32.5 (1962), pp. 662–671. DOI: 10.2514/8.6121.

[125] P. Hill and C. Peterson. *Mechanics and Thermodynamics of Propulsion*. New York, NY: Addison-Wesley, 1992. ISBN: 9780201146592.

[126] J. Linnell and T. Miller. "A Preliminary Design of a Magnesium Fueled Martian Ramjet Engine". In: *Proc. of the 38th AIAA/ASME/SAE/ASEE Joint Propulsion Conference, Inidianapolis, IN* (2012). AIAA-2002-3788. DOI: 10.2514/6.2002-3788.

[127] V. Weiser, M. Juez-Lorenzo, S. Kelzenberg, S. Knapp, A. Koleczko, V. Kuchenreuther-Hummel, E. Roth, and T. Schäfer. "Pressurized Silicon combustion for pyrotechnic and energetic use". In: *51st International Annual Conference of the Fraunhofer ICT, Karlsruhe* (2022), pp. 56–62. DOI: https://doi.org/10.24406/publica-149.

[128] M. W. Beckstead. "A Summary of Aluminum Combustion". In: *Proc. of the Internal Aerodynamics in Solid Rocket Propulsion Conference, Rhode-Saint-Genèse, Belgium* (2004). NATO report RTO-EN-023.

[129] N. G. Vaz, I. Shancita, and M. L. Pantoya. "Thermal oxidation analysis of aerosol synthesized fuel particles composed of Al versus Al-Si". In: *Powder Technology* 382 (2021), pp. 532–540. DOI: https://doi.org/10.1016/j.powtec.2021.01.018.

[130] K. Estala-Rodriguez, S. Cordova, and E. Shafirovich. "Oxidation and combustion of stabilized lithium metal powder (SLMP)". In: *Proceedings of the Combustion Institute* (2022). DOI: https://doi.org/10.1016/j.proci.2022.07.051.

[131] S. Cordova, K. Estala-Rodriguez, and E. Shafirovich. "Infiltration-controlled combustion of magnesium for power generation in space". In: *Combustion and Flame* 238 (2022), p. 111950. DOI: https://doi.org/10.1016/j.combustflame.2021.111950.

[132] A. L. Corcoran, V. K. Hoffmann, and E. L. Dreizin. "Aluminum particle combustion in turbulent flames". In: *Combustion and Flame* 160.3 (2013), pp. 718–724. DOI: https://doi.org/10.1016/j.combustflame.2012.11.008.

[133] P. Julien, S. Whiteley, M. Soo, S. Goroshin, D. Frost, and J. Bergthorson. "Flame speed measurements in aluminum suspensions using a counterflow burner". In: *Proceedings of the Combustion Institute* 36 (2016). DOI: 10.1016/j.proci.2016.06.150.